OPTIMIZATION, APPLICATION, AND CROSS-CORRELATION OF DCE-MRI IN SMALL ANIMAL MODELS OF CANCER

By

Mary Elizabeth Loveless

Dissertation

Submitted to the Faculty of the

Graduate School of Vanderbilt University

in partial fulfillment of the requirements

for the degree of

DOCTOR OF PHILOSOPHY

in

Biomedical Engineering

December, 2010

Nashville, Tennessee

Approved:

Professor Thomas E. Yankeelov

Professor John C. Gore

Professor Mark D. Does

Professor Christopher C. Quarles

Professor J. Oliver McIntyre

DEDICATION

I would like to dedicate this dissertation to all the members of my family that have been affected by cancer. Over the past five years, I have worked to contribute a small piece of the puzzle in cancer research in honor and in loving memory of my grandmother (breast cancer) and grandfather (pancreatic cancer). And to my aunt and aunt-in-law who are breast cancer survivors, know that you inspire and encourage me to continue fighting the good fight! I dedicate my work to you.

I would also like to dedicate the work presented here to a wonderful mentor, colleague, and friend, Jane Halliday. Without your valuable input, insight, and cheerful personality, this work would be incomplete. I thank you for all your contributions, especially when you made us laugh; you will be missed.

ACKNOWLEDGMENT

Words really fall short of how much I appreciate all the people who have helped with this work and who have supported me along the way. First, I would like to thank my WONDERFUL husband Daniel who has been my rock throughout my entire graduate school career. Throughout the creation of this dissertation, there have been some very extraordinary "ups" and "downs," moments of desperation, moments of sheer exhaustion, and moments of panic; but Daniel has taken it all in stride and talked me through it – and when that didn't work, he bought me ice cream. This work would not have been possible without all his encouragement and understanding. And to my family, Mom, Dad and Katie, I thank you all for your patience and understanding. Your unconditional love provides the cornerstone for my success. Thanks to all of you; I would not be where I am today without you.

I would also like to express my gratitude to my advisor Tom. Tom has been an amazing advisor - exuding patience, insight, and a cheerful disposition that makes any problem seem doable, even capturing unicorns. I feel I have learned so much from him, and I truly thank him for sharing his knowledge and expertise with me. And a special shout out to Margie - my occasional (and sometimes frequent), "life advisor." I thank her for her words of support, helpful ideas and suggestions, and the cookies that kept me awake during my all-nighters.

And to my committee, Dr. Gore, Dr. Does, Dr. Quarles, and Dr. McIntyre: I thank them for their insight and commitment to make this dissertation the best it can be. I

also thank them for their flexibility and cooperation during the many meetings scheduled throughout this process!

This work would not be complete without the help of my colleagues both at VUIIS and AstraZeneca. To the many of you who have had detailed discussions about this work specifically those in the Cancer Imaging Group (lots of folks!), Tom's Group of Awesomeness (Jennifer, Lori, Lisa, Nikki, Richard, Dave, and Stephanie), and the office of MCN AA1101 (Richard, Adrienne, Adam, Allen, Subechya, Lindsay, and Mariam), I thank you for your contributions and/or letting me vent. To my friends at the MMP Core (Carlo and Tasneem), thank you so much for your flexibility and willingness to help out in a pinch!

I would also like to thank all the valuable insights from my colleagues at AstraZeneca: to John Waterton, Jane Halliday, and Carsten Leiss at the Alderly Park facility, I thank you for your contributions both imaging and animal design protocols and for your help during ISMRM 2010; to Dennis Huszar, Corinne Reimer, Maria Pinzon-Ortiz, Deborah Lawson, Mike Collins, Prasad Nadella at the Waltham, MA facility, I thank you for your insight into the molecular/biological mechanisms of AZD 1480 as well as your assistance with the immunohistochemistry.

I would like to thank Dr. Gore, Nancy Hagan, Tracy Porchak, Jarrod True, Daniel Colvin, Ken Wilkens, Zou Yue, Bruce Martin, and all those who keep such a wonderful place like the VUIIS going. It has been an honor to work at such a great facility with such wonderful people.

And finally, I would like to thank my funding sources for their support during the investigation of this work. The AstraZeneca predoctoral training grant, National

Cancer Institute - NCI U24 CA126588 (Small Animal Imaging Resource Program) and NCI P30 CA068485 (Cancer Center Support Grant), - and the National Institute of Biomedical Imaging and Bioengineering (NIBIB 1K25 EB005936) generously provided the funding for materials and time to produce the work presented in this dissertation.

LIST OF FIGURES

LIST OF TABLES

TABLE OF CONTENTS

Page

CHAPTER I

INTRODUCTION

With cancer encompassing a range of disease states and phenotypes, identifying effective or non-effective treatments early, accurately, and non-invasively is essential such that the course of treatment can be modified if needed. Thus, using various imaging techniques such as X-ray mammography, positron emission tomography (PET), and magnetic resonance imaging (MRI) has become a popular option for the ability to non-invasively monitor changes during treatment. This work will discuss two types of cancer imaging techniques, and the importance they have to several classes of drug treatment regimens. Additionally, this work will further optimize and identify errors in current protocols used in preclinical studies of drug efficacy. These optimized protocols will then be used to assess the efficacy of a novel anti-cancer treatment early in the course of therapy; and finally, the relationship of two imaging biomarkers frequently used in monitoring cancer therapy will be assessed and compared to histology.

The goal of Aim 1 is to assess the error in parameters extracted from dynamic contrast-enhanced magnetic resonance imaging (DCE-MRI) modeling when using a vascular input function (VIF) derived from a population average versus those extracted with an individually measured VIF in mice. The measurement of a VIF needed to drive pharmacokinetic models requires high temporal resolution and the presence of a major vessel within the field of view. In order to achieve these requirements, signal is sacrificed, and coverage and location of the region of interest is

limited. VIF measurements were obtained in a cohort of mice using two different contrast agents of varying molecular weight in order to assess the error in the kinetic parameters within the tumor associated with using a population VIF or individual VIF.

The goal of Aim 2 is examine a novel Jak2 inhibitor with both DCE-MRI and diffusion-weighted MRI (DW-MRI) to determine if these imaging techniques can be used to assess preclinical efficacy. Both DCE-MRI and DW-MRI have been shown to be informative when monitoring treatment and determining drug efficacy. Using a novel drug that functions as a Jak2 inhibitor, animals were imaged using DCE-MRI and DW-MRI at multiple time points to assess the effectiveness of using DCE-MRI and DW-MRI as early response metrics

The goal of Aim 3 is to compare the parameters found using DCE-MRI with similar measures determined from DW-MRI both before and during the course of therapy. Apparent diffusion coefficient (*ADC*) maps obtained from DW-MRI have been shown to be a metric of cellularity in tumors. Since one of the parameters obtained from DCE-MRI studies is the fraction of extravascular-extracellular space (v_e), maps of *ADC* and v_e should be directly proportional to each other in that they both change positively in response to reduced cell density. However, previous literature suggests that the relationship between these parameters may be more complex in response to treatment. The relationship between these two parameters has been assessed on a spatial and histological scale using two treatment regimens.

CHAPTER II

MAGNETIC RESONANCE IMAGING

Fundamentals of Magnetization and Relaxation

In the following work, magnetic resonance imaging (MRI) is the primary tool used to probe various aspects of cancer and to monitor cancer treatment. An abbreviated description of nuclear magnetic resonance (NMR) and MRI is provided for clarity, but more details can be found in reference (1).

The signal from MRI is derived from nuclear magnetic properties of particular nuclei such as ^{1}H, ^{13}C, and ^{19}F, for example. This work exclusively describes proton or ^{1}H MRI but non-proton MRI is discussed in references (2,3). These nuclei possess property magnetic moment that has both magnitude and direction, illustrated in Fig. II-1 (a).

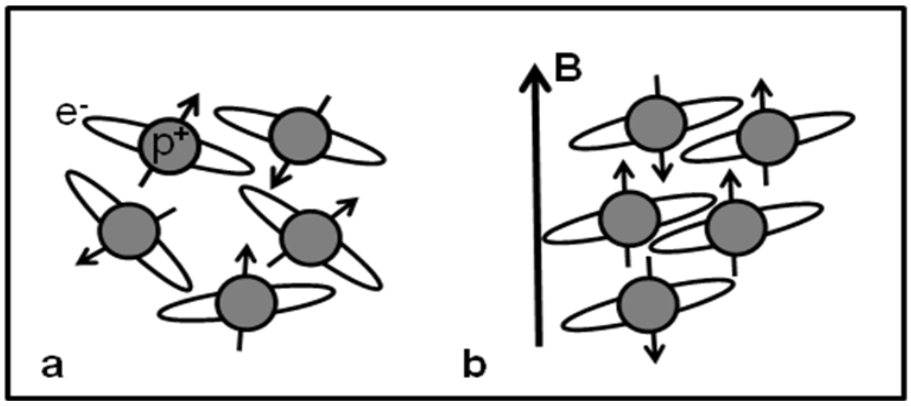

Fig. II-1. Spin Alignment in a Magnetic Field. Panel **a** illustrates nuclei as magnetic dipoles, or "spins," in random alignment while panel **b** shows that the nuclei align parallel or anti-parallel when an external magnetic field ***B*** is introduced.

When no magnetic field is present, these magnetic dipoles, or "spins," have random alignment; however, when an external magnetic field is present, these spins will align either parallel or anti-parallel to the field, shown in Fig. II-1 (b). These protons not only

align with the external magnetic field ***B***, but they also precess about the axis ***B*** is applied. The frequency at which they precess is known as the Larmor frequency (ω_o). The Larmor frequency is directly proportional to the gyromagnetic ratio, γ (approximately 42.6 MHz/T for ^{1}H), and the strength of the external magnetic field (***B***) and can be described as

$$\omega_0 = -\gamma \cdot B. \quad \text{(II-1)}$$

On a more macroscopic level, the individual nuclei or spins can be summed to produce a net magnetization vector (***M***) that can describe the system as in Fig. II-2 (a). At equilibrium, the magnetization vector lies parallel to the main magnetic field, ***B***. The bulk magnetization align with and precess about the external magnetic field ***B***.

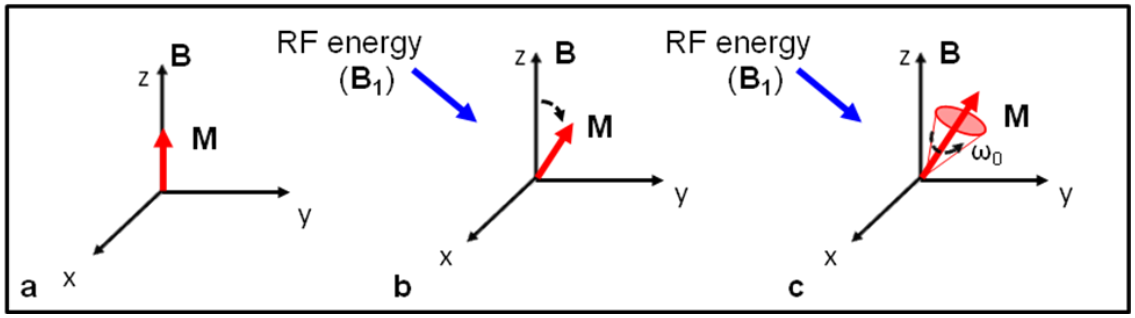

Fig. II-2. The "spins" are summed to form a net magnetization vector (***M***) that, at equilibrium, aligns with the magnetic field, ***B***, as shown in panel (a). As RF energy (***B₁***) is introduced at the Larmor frequency, ***M*** will tip away from equilibrium as shown in panel (b) while panel (c) shows that the vector ***M*** also precesses at the Larmor frequency forming a cone of precession.

By introducing radiofrequency (RF) energy at the Larmor frequency in a form such as a pulsed ***B₁*** field along the *x*-axis, the vector is nutated away from a direction parallel to the external magnetic field as shown in Fig. II-2 (b). If the applied ***B₁*** pulse stops, the net magnetization (***M***) will slowly "relax" back to equilibrium. The process of ***M*** returning back to alignment with the external magnetic field ***B*** is known as longitudinal relaxation and is characterized by a time constant known as $T_1 (\equiv 1/R_1)$. This longitudinal relaxation

is not the only type of relaxation occurring with this system. As the net magnetization ***M*** is tipped away from the direction parallel to the main magnetic field, the spins are aligned or "in phase." Instead of the net magnetization "relaxing" along the direction of the magnetic field, ***M*** will precess around the field direction, similar to a spinning gyroscope. Thus, the spins exhibit more of a characteristic cone of precession around the magnetization vector ***M*** as represented in Fig. II-2 (c).

At equilibrium, these spins precess at a frequency affected by the local and global environmental magnetic fields. To clarify, Fig. II-3 shows the magnetization vector ***M*** in a plane perpendicular to the main magnetic field, also known as the transverse plane. The spins precess at different frequencies until the $\boldsymbol{B_1}$ pulse is introduced which aligns the spins as shown in Fig. II-3 (a).

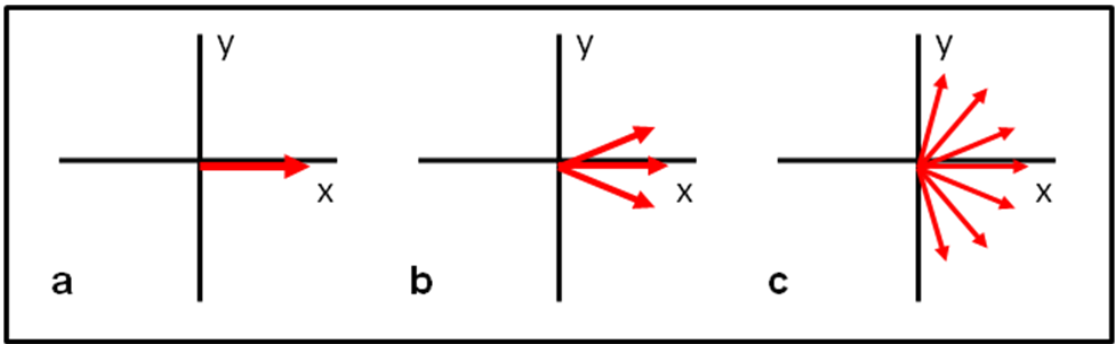

Fig. II-3. In the transverse plane (perpendicular to the magnetic field ***B***), spins will be in phase as they precess at the Larmor frequency as shown in panel (a). Once the $\boldsymbol{B_1}$ pulse is removed, the spins begin to dephase according to local magnetic field variations at a rate of T_2 shown in panel (b) and (c).

With no RF energy input, the spins will dephased based on their independent precession frequency as shown in Fig. II-3 (b) and (c); consequently, the spins dephase at a rate known as T_2. The effects of these relaxation properties can be described in a series of equations known as the Bloch equations (4). The change in the net magnetization ***M*** as

it experiences a torque associated with the pulsed magnetic field $\boldsymbol{B_1}$ and the effects of T_1 and T_2 relaxation (noted as $\boldsymbol{R}$ for relaxation) can be described by

$$\frac{d\boldsymbol{M}}{dt} = \gamma \boldsymbol{M} \times \boldsymbol{B_1} - \boldsymbol{R}(\boldsymbol{M}(t) - M_0). \qquad \text{(II-2)}$$

Since T_1 and T_2 effect the magnetization vector in different directions, R must be broken down along the three orthogonal axes to reflect the transverse relaxation occurring the x-y plane and longitudinal relaxation occurring along the z-direction:

$$\frac{d\boldsymbol{M_x}}{dt} = \gamma(\boldsymbol{M_y} \cdot \boldsymbol{B_z} - \boldsymbol{M_z} \cdot \boldsymbol{B_y} - \frac{\boldsymbol{M_x}}{T_2}), \qquad \text{(II-3)}$$

$$\frac{d\boldsymbol{M_y}}{dt} = \gamma(\boldsymbol{M_x} \cdot \boldsymbol{B_z} - \boldsymbol{M_z} \cdot \boldsymbol{B_x} - \frac{\boldsymbol{M_y}}{T_2}), \text{ and} \qquad \text{(II-4)}$$

$$\frac{d\boldsymbol{M_z}}{dt} = \gamma(\boldsymbol{M_x} \cdot \boldsymbol{B_y} - \boldsymbol{M_y} \cdot \boldsymbol{B_x} - \frac{\boldsymbol{M_z} - M_0}{T_1}). \qquad \text{(II-5)}$$

These equations can be integrated and solved by the Laplace transform, for example, to obtain:

$$\boldsymbol{M_{xy}}(t) = \cdot \boldsymbol{M_{xy}}(0) \cdot e^{-t/T_2} \qquad \text{and} \qquad \boldsymbol{M_z}(t) = \cdot \boldsymbol{M_z}(0) \cdot (1 - e^{-t/T_1}). \qquad \text{(II-6/II-7)}$$

By manipulating the timing and $\boldsymbol{B_1}$ pulses, sequences can be developed to better exploit these relaxation properties to differentiate between tissue types and diseased states. The two most common MR experiments are the spin echo or gradient echo acquisitions. A simple spin-echo sequence is described as a pulse that reflects a 90° tip away from the z axis and then a 180° refocusing pulse to "reverse" the dephasing spins shown in Fig. II-3 (c) so that they will partially rephrase, causing a signal echo at a time TE, or echo time. The change in signal (S), which is proportional to the net magnetization described above, can be characterized by the following equation:

$$S = S_0 \cdot [1 - 2e^{-(TR - TE/2)/T_1)} + e^{-TR/T_1}] \cdot e^{-TE/T_2}, \qquad \text{(II-8)}$$

where S_0 is the initial signal related to the net magnetization and TR is the repetition time between 90° pulses.

The second common NMR experiment is based on administering a pulse at an arbitrary flip angle, α, and using magnetic gradients to rephase the signal. The gradient echo equation describes the change in signal by

$$S = S_0 \cdot \frac{(1 - e^{-TR/T_1}) \cdot sin(\alpha) \cdot e^{-TE/T_2^*}}{(1 - cos(\alpha) \cdot e^{-TR/T_1})}, \qquad \text{(II-9)}$$

where T_2^* represents the combination of T_2 and T_2', a quantity that represents sample and field homogeneity. For the purpose of the work presented in this dissertation, it is assumed that there is a relatively homogeneous external field such that $T_2^* \approx T_2$. The parameters of TR, TE, and α can be manipulated to weight the image contrast based on either T_1 or T_2 relaxation. For example, the acquisition can be weighted for T_1 relaxation by making the TR short relative to T_1 and TE very short (much shorter than the T_2 of the tissue of interest); thus, the T_2 relaxation component will become negligible. The work presented here focuses primarily on T_1 relaxation so for the sake of brevity, T_2 relaxation measurements will be omitted but further discussion can be found in reference (1).

Image Reconstruction

Determining the origin, in three dimensional space, of the signals discussed in the previous section is required in order to form an image; spatial encoding is the process by which these signals are mapped into coordinates in space. First, a "slice select" magnetic gradient is used to change the precession frequency of the spins along the slice selection axis (*e.g.*, the *z*-axis). By having these precession frequencies vary in a known spatial

coordinate system, the excitation pulse can then be "tuned" to perturb spins at a particular location along the *z*-axis; thus, the selected slice will be uniquely identified. Additional gradients can be used to identify the origin of a signal within the selected slice/plane. A phase encode gradient is applied, essentially assigning "columns" of spins with phases varying across a field of view. And finally, a frequency-encoding gradient is applied. This gradient divides the image space into "rows" with varied precession frequencies. Now, the signal extracted from an MRI experiment can be decomposed using a 2D Fourier transform analysis, allowing the frequency and phase contributions assigned by the spatially varied gradients to be separated and form an image.

Measuring T_1

As discussed above, once magnetization has been tipped into the transverse plane, it will regrow along the *z*-axis back to equilibrium at a rate of R_1 ($\equiv 1/T_1$). There are several methods for determining the T_1 of tissue (5). For example, by collecting data at multiple *TR* or flip angle (α) values *via* either a spin echo or gradient echo experiment, Eqn. (II-8) or Eqn. (11-9) can be fit to the data to estimate T_1 for a particular sample. One technique for a robust estimation of T_1 is an inversion recovery sequence in which the net magnetization is flipped 180° and is sampled along the regrowth at different times, called inversion times, *TI*. After the inversion pulse the signal (*S*) can be described as

$$S = S_0 \cdot \left| (1 - 2 \cdot e^{-TI/T_1} + e^{-TR/T_1}) \right|, \qquad \text{(II-10)}$$

where S_0 and S are the signal intensities at baseline and at the inversion time, respectively. The resulting absolute value of the signal at each inversion time is graphically shown in Fig. II-4. After acquisition, the data is fit to Eqn. (11-10),

represented by the solid line in the figure. This fit produces an estimation of T_1 for each voxel to yield a T_1 map of the tissue of interest.

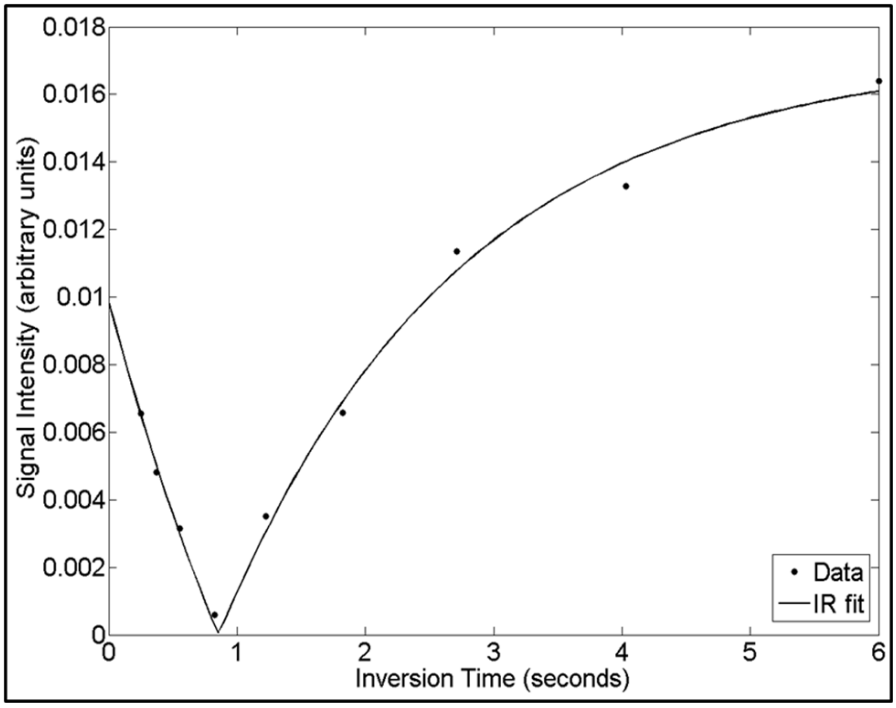

Fig. II-4. The signal can be sampled at multiple inversion times (•) and fit to Eq. II-10 (solid line) to obtain T_1 measurements.

Contrast Agents

Unlike X-ray or CT contrast agents (CAs) that provide a direct effect on the image signal, MRI contrast agents indirectly alter the signal *via* influencing the relaxation of the hydrogen nuclei. Simply put, MRI contrast agents work by shortening the native relaxation times of the tissue(s) they penetrate, thereby changing the R_1 of that tissue. In order to accomplish this task, MRI CAs must be designed to strongly interact with the spin, in this case, the hydrogen nuclei. One characteristic of an ideal MRI contrast agent is a high number of unpaired electrons. Unpaired electrons have a much stronger magnetic moment than that of the nuclei; thus, MRI CAs are typically developed by using elements with many unpaired electrons to dominate the magnetic moment produced

by the nuclei. The two CAs discussed in this Dissertation use chelated gadolinium (Gd), which has seven unpaired electrons (6).

In addition to unpaired electrons, another desirable characteristic of an MRI contrast agent is an appropriate correlation time. Molecules in a liquid are free to rotate, and the inverse of the frequency at which they rotate is known at as the correlation time. Molecules that have an optimum rotation can interact with surrounding molecules more frequently causing the relaxation times to change. For T_1 relaxation, molecules rotating at the Larmor frequency have the maximum opportunity to interact with neighboring molecules. Since the rotation frequency in a liquid is typically faster than the Larmor frequency, the size of the contrast agent increases the correlation time for a more efficient interaction. The two contrast agents used in this work have different molecular sizes, directly responsible for the difference in relaxivities (7,8). The relaxivity of a contrast agent describes how the R_1 relaxation changes with respect to concentration, and this is dependent on the type of agent used as well as field strength at relatively low concentrations (like that in tissue). By using the baseline relaxation measurement, R_{10}, and the known relaxivity of the agent (r), the concentration of contrast agent can be determined by (9)

$$R_1 = r \cdot [CA] + R_{10}. \qquad \text{(II-11)}$$

The relaxivity of an agent describes the efficacy of an agent to induce a change in relaxation; therefore, the higher the relaxivity, the better contrast between the surrounding tissue and tissue affected by the agent.

Gadolinium diethylenetriaminepentaacetic acid (Gd-DTPA) is a small (~0.6 kDa) hydrophilic, barrier-limited molecule that has strong paramagnetic properties allowing it

to successfully change the relaxation rates of surround tissue. Gd-DTPA has high *in vivo* stability, rapid clearance, and minimal toxicity; these characteristics have allowed Gd-DTPA to be a frequently used CA in the clinic (10). A contrast agent called P846 (Guerbet, Aulnay-sous-Bois, France) has a molecular weight of approximately 3.54 kD and consists of a single Gd ion in a macro-cyclic 3-armed chelate. This larger contrast agent has a higher correlation time, yielding a higher relaxivity relative to Gd-DTPA. Additionally, the size of this CA gives rise to different pharmacokinetic properties; as shown in Chapter VI, this property gives rise to an elongated contrast enhancement period as it is less permeable than the smaller agent (11).

The subsequent studies in Chapters V through VIII will utilize these properties of MRI, relaxation, and MRI contrast agents to examine properties that distinguished diseased tissue from normal tissue. While MRI is applicable to a wide range of disease states, this work will focus specifically on the vascular and cellular aspects of cancer.

References

1. Haacke M, Brown R, Thompson M, Venkatesan R, Haacke M, Brown R, Thompson M, Venkatesan R. Magnetic Resonance Imaging: Physical Principles and Sequence Design: Wiley-Liss; 1999.
2. de Graaf RA. Basic Principles: John Wiley & Sons, Ltd; 2007. 1 p.
3. de Graaf RA. Magnetic Resonance Imaging: John Wiley & Sons, Ltd; 2007. 191 p.
4. Bloch F. Nuclear Induction. Physical Review 1946;70(7-8):460.
5. Kingsley P. Methods of measuring spin-lattice (T-1) relaxation times: An annotated bibliography. CONCEPT MAGNETIC RES 1999;11(4):243-276.
6. Hendrick RE, Haacke EM. Basic physics of MR contrast agents and maximization of image contrast. J Magn Reson Imaging 1993;3(1):137-148.
7. Toth E, Helm L, Merbach A. Relaxivity of MRI contrast agents. TOP CURR CHEM 2002;221:61-101.
8. Borel A, Bean J, Clarkson R, Helm L, Moriggi L, Sherry A, Woods M. Towards the rational design of MRI contrast agents: Electron spin relaxation is largely unaffected by the coordination geometry of Gadolinium(III)-DOTA-Type complexes. CHEM-EUR J 2008;14(9):2658-2667.
9. Landis CS, Li X, Telang FW, Molina PE, Palyka I, Vetek G, Springer CS, Jr. Equilibrium transcytolemmal water-exchange kinetics in skeletal muscle in vivo. Magn Reson Med 1999;42(3):467-478.
10. Weinmann HJ, Brasch RC, Press WR, Wesbey GE. Characteristics of gadolinium-DTPA complex: a potential NMR contrast agent. AJR Am J Roentgenol 1984;142(3):619-624.
11. Peldschus K, Hamdorf M, Robert P, Port M, Graessner J, Adam G, Herborn CU. Contrast-enhanced magnetic resonance angiography: evaluation of the high relaxivity low diffusible gadolinium-based contrast agent P846 in comparison with gadoterate meglumine in rabbits at 1.5 Tesla and 3.0 Tesla. Invest Radiol 2008;43(12):837-842.

CHAPTER III

BIOLOGICAL BACKGROUND OF CANCER

Introduction

While cancer is a very complex disease state, there are several "hallmarks" that can be generalized across cancer type or tumor model. These attributes are discussed in greater detail in references (1,2) but, this work will focus on two specific traits: cellularity and angiogenesis.

Cellularity

One fundamental characteristic of cancer cells is the ability to proliferate unregulated, typically resulting in a very dense tumor mass that can spread depending on the aggressive nature of the cancer. There are several aspects that contribute to the unregulated proliferation as documentd in established cancer cell lines. First, cancer cells adapt to produce and sustain growth signals despite environmental factors. It has been shown that cancer cells can generate or mimic growth signals independently. An example of this is the ability of glioblastomas and sarcomas to produce platelet-derived growth factor (PDGF) and tumor growth factor α (TGFα), both of which blood vessel formation and cell growth regulation (1). Surface receptors for growth factors have also been shown to be upregulated in cancer. This upregulation in receptors tends to make tumor cells hypersensitive to potentially low to normal amounts of circulating growth factors; overexpression of the *HER2/neu* receptors, which activate proliferative molecular pathways, have been noted in some stomach and mammary cancer cell lines (3). With

these and other mechanisms, cancer cells can sustain activation of proliferative pathways without input from the surrounding environment.

To complement the independent generation of pro-growth factors, tumor cells have developed mechanisms to becoming insensitive to anti-growth factors (4) and avoid terminal differentiation (5). Anti-growth factors drive cells out of an active proliferative cycle into a state of quiescence. For example. retinoblastoma protein (pRb) is strongly linked to anti-proliferative signal pathways; when pRb is in a hypophosphorylated state, it blocks proliferation by sequestering E2F transcription factor, which is responsible for gene expression associated with transitioning from G1 into S phase of the cell cycle (4). It has been shown that if the pRb pathway is perturbed, E2F is released, allowing the cells to proliferate, insensitive to anti-growth feedback. TGFβ, for example, is a small signaling molecule that has been shown to prevent phosphorylation of pRb that would render it inactive, thereby reinforcing proliferative effects (6).

Additionally, cancer cells develop the ability to evade programmed cell death, or apoptosis. Briefly, most apoptotic signaling funnels through the mitochondria, where a potent catalyst of apotosis, cytochrome C, is released (7). Once cytrochrome C is released, it can stimulate intracellular proteases known as caspases (8). These caspases are responsible for executing a sequence that leads to cell death. Mutations in the apoptotic signaling pathways which activate cytochrome C can lead to anti-apoptotic affects. For example, bcl-2, an anti-apoptotic protein, is upregulated in follicular lymphoma, leading to the improved survival of lymphocytes. (9,10).

Increased proliferation and survival are not the only mechanisms by which cancer cells flourish; the ability to continuously proliferate is not governed by growth factors alone. Normal cells typically have a terminal number of replications within a lifespan before entering a state of senescence. A phenotype of cancer cells that differentiates them from normal cells is the ability to bypass the state of senescence and become essentially "immortalized," proliferating limitlessly (11). With cancer cells developing such phenotypes, monitoring the cellularity of a tumor cite has become an important biomarker for aggressive tumors. Additionally, this attribute has become a target for therapy as well as a useful biomarker for imaging, discussed in subsequent chapters.

Angiogenesis

Another fundamental "hallmark" of cancer is the ability to recruit and sustain a vascular network to allow for a continuous supply of nutrients. In order for a tumor to grow beyond approximately 1-2 mm^3, a tumor must recruit and form new vasculature as it can no longer rely on the passive diffusion of nutrients (12). During the process known as angiogenesis, several growth factors, including vascular endothelial growth factor (VEGF) are secreted to promote the migration of endothelial cells to the site. In particular, VEGF has been shown to be a rate-limiting step in angiogenesis, making it a target for various therapies as well. VEGF binds to two primary endothelial receptors known as Flt-1 (VEGFR-1) and KDR (VEGF-R2). *Via* these receptors, various pathways are stimulated that promote neovascularization in tumors including endothelial cell migration and proliferation (13), endothelial cell precursor recruitment (14), formation of capillary tubes (15) and permeability enhancement (16). However, the vessels produced

from pathological angiogenesis differ from that of normal vasculature. Normal vasculature is arranged as a progression from large arteries feeding into smaller arteries/arterioles which terminate at the capillary bed. From the capillary bed, venules carry the deoxygenated blood to small veins which empty into larger primary veins. During tumor angiogenesis, the imbalance between anti-angiogenic and angiogenic factors can lead to abnormal vasculature formation. Tumor vasculature has been reported to be leaky and poorly constructed with tortuous topology containing incomplete vessels (12,17,18).

The importance of tumor angiogenesis has led to a number of drugs developed to inhibit the growth of cancer *via* disruption of angiogenesis. The goal of these so-called anti-angiogenic drugs is to essentially cut off the development of an adequate blood supply, stunting tumor growth.

Treatment

As mentioned, numerous anti-cancer treatments and therapies have been developed that target the various cancer-specific (and even many nonspecific) characteristics. Below are discussed three categories of treatment: cytotoxic drugs, vasculature-targeted drugs, and a novel class of Jak2 inhibitors.

Cytotoxic Drugs

Cytotoxic treatments have been available in the clinic for several decades. This classification of drug typically attacks or disrupts mitotic function of neoplastic cells, thereby inducing apoptosis. Cytotoxic therapies interfere with cell proliferation by 1)

damaging DNA within the cell, causing cytotoxicity, 2) interfering with basic cellular metabolites such as enzymes used in the formation of nucleotides, or 3) inhibiting spindle formation during cell division. Doxorubicin is an example of a cytotoxic chemotherapy drug that acts by intercalating DNA and by inhibiting macromolecular biosynthesis. This process inhibits DNA unwinding and thereby hinder transcription (19,20). Methotrexate acts as a folate antagonist that inhibits enzymes involved in the formation of nucleotides (21). Another clinically-used cytotoxic therapy, paclitaxel, targets microtubule formation without which the cell cannot divide (22,23). While these therapies are commonly used in the clinic, they are not necessarily targeted to only tumor cells, and the side effects involve toxicity to other organs or systems that have high cell turnover such as hair follicles and intestinal lumen. Thus, targeting therapies to tumor-specific phenotypes has become an important area of research over the past several decades (24).

Vasculature-Targeted Drugs

Within the realm of "targeted" therapies, there are two classes that target the vasculature of the tumor system: anti-vascular and anti-angiogenic drugs. Anti-vascular drugs target the vascular endothelium; the vascular endothelium is highly proliferative and a class of tubulin-binding microtubule-depolymerizing agents has been developed to cause the collapse of mature tumor vessels. For example, combretastatins, a subclass of tubulin-binding agents, have been used widely in the clinic (25,26) Anti-angiogenic drugs specifically target angiogenic pathways, ultimately inhibiting tumor neovascularization. Frequently, receptors and receptor tyrosine kinases such as vascular endothelial growth factor (VEGF) receptor, FLT1, PI3 kinase, and HIF are targeted by

these drugs because they are included in pathways that contribute to angiogenesis. Bevacizumab, ZD6474, SU11248, vatalanib, and AGM-1470 are several agents that serve as anti-angiogenic therapies (27). Recentin is a well-characterized anti-angiogenic drug that has been shown to reduce vascular density and stunt tumor growth reliably on the Calu-6 tumor lines. Otherwise known as AZD 2171 (4-[(4-Fluoro-2-methyl-1H-indol-5-yl)oxy]-6-methoxy-7-[3-(pyrrolidin-1-yl)propoxy]quinazoline), Recentin has a molecular weight of 450.51 D. This drug acts as a potent inhibitor of KDR tyrosine kinase thereby inhibiting VEGF induced signaling pathways in endothelial cells. In a comprehensive investigation into the efficacy of AZD 2171, Wedge, et al, compared AZD 2171 activity with other well known angiogenesis inhibitors both *in vitro* and *in vivo* (28). Not only was AZD 2171 found to be a potent inhibitor of KDR, it was shown to inhibit endothelial cell and tumor cell proliferation in a broad spectrum of human tumor models. Specifically, 6.4 ± 0.6 μmol/L of AZD 2171 were required to halt proliferation of the Calu-6 lung tumor cell line.

Jak2 Inhibitor Drugs

Other signal transduction pathways have also become a target for cancer therapies. Some of these pathways include downstream effects that offer a combination of anti-anagiogenic, pro-apoptotic, and/or anti-proliferative consequences (24). An example of this type of targeted therapy is a novel class known as Jak2 inhibitors. The Janus family kinases (Jak) are fundamental to mediating activation of signal transducers and activator of transcription (Stat) proteins. Stat proteins are responsible for mediating cytokine and growth factor responses. Over the past two decades, it has been shown that persistent

activation of Stat3 is found in a wide variety of human cancer cell lines (29), and that aberrant Stat3 activation is necessary for some cancer cell lines to survive (30,31). Stat3 activation has been implicated in numerous survival and proliferative pathways, and blocking Stat3 has shown increased apoptosis induction (32) and decreased proliferation (30,33). In addition to implications in the upregulation of survival and proliferative pathways, it has been reported that persistent activation of Stat3 directly targets VEGF (32), one of the most potent angiogenesis-inducing signaling factors. Stat3 acts to direct transcriptional activation of VEGF, as well as having downstream effects that, when inhibited, may slow HIF1 activation, which is another upregulator of VEGF (34).

A selective Jak2 small-molecule inhibitor, AZD 1480, has been shown to actively suppress the role of Stat3 in tumorgenesis. Tumor growth in multiple cell lines has been stunted at various doses. Additionally, Stat3 expression was reduced significantly in tumor tissues treated with the AZD 1480 (35). In unpublished data, mean vessel density was also significantly reduced in murine xenografts relative to vehicle controls.

Conclusion

Thus, as more and more progress is made in understanding molecular and physiological "hallmarks" of cancer, specificity and efficacy of treatments will continue to improve. To complement these targeted drugs, it is important to have specific metrics for monitoring the efficacy of new treatments that may similarly affect these aspects of cancer. Imaging has become a standard of care for non-invasively monitoring the efficacy of such drugs. For example, an imaging technique sensitive to cellular changes would be useful in monitoring cytotoxic or Jak2-inhibiting treatments while an imaging method

that quantified vascular properties would be valuable in assessing vascular- or Jak2-targeted therapies. In the following chapter, two specific imaging techniques are discussed.

References

1. Hanahan D, Weinberg RA. The hallmarks of cancer. Cell 2000;100(1):57-70.
2. Pietras K, Ostman A. Hallmarks of cancer: interactions with the tumor stroma. Exp Cell Res;316(8):1324-1331.
3. Slamon DJ, Clark GM, Wong SG, Levin WJ, Ullrich A, McGuire WL. Human breast cancer: correlation of relapse and survival with amplification of the HER-2/neu oncogene. Science 1987;235(4785):177-182.
4. Weinberg RA. The retinoblastoma protein and cell cycle control. Cell 1995;81(3):323-330.
5. Foley KP, Eisenman RN. Two MAD tails: what the recent knockouts of Mad1 and Mxi1 tell us about the MYC/MAX/MAD network. Biochim Biophys Acta 1999;1423(3):M37-47.
6. Moses HL, Yang EY, Pietenpol JA. TGF-beta stimulation and inhibition of cell proliferation: new mechanistic insights. Cell 1990;63(2):245-247.
7. Green DR, Reed JC. Mitochondria and apoptosis. Science 1998;281(5381):1309-1312.
8. Thornberry NA, Lazebnik Y. Caspases: enemies within. Science 1998;281(5381):1312-1316.
9. Korsmeyer SJ. Bcl-2: an antidote to programmed cell death. Cancer Surv 1992;15:105-118.
10. Strasser A, Harris AW, Bath ML, Cory S. Novel primitive lymphoid tumours induced in transgenic mice by cooperation between myc and bcl-2. Nature 1990;348(6299):331-333.
11. Hayflick L. Mortality and immortality at the cellular level. A review. Biochemistry (Mosc) 1997;62(11):1180-1190.
12. Folkman J. Tumor angiogenesis: therapeutic implications. N Engl J Med 1971;285(21):1182-1186.
13. Rousseau S, Houle F, Huot J. Integrating the VEGF signals leading to actin-based motility in vascular endothelial cells. Trends Cardiovasc Med 2000;10(8):321-327.
14. Asahara T, Takahashi T, Masuda H, Kalka C, Chen D, Iwaguro H, Inai Y, Silver M, Isner JM. VEGF contributes to postnatal neovascularization by mobilizing bone marrow-derived endothelial progenitor cells. Embo J 1999;18(14):3964-3972.
15. Koolwijk P, Peters E, van der Vecht B, Hornig C, Weich HA, Alitalo K, Hicklin DJ, Wu Y, Witte L, van Hinsbergh VW. Involvement of VEGFR-2 (kdr/flk-1) but not VEGFR-1 (flt-1) in VEGF-A and VEGF-C-induced tube formation by human microvascular endothelial cells in fibrin matrices in vitro. Angiogenesis 2001;4(1):53-60.
16. Bates DO, Heald RI, Curry FE, Williams B. Vascular endothelial growth factor increases Rana vascular permeability and compliance by different signalling pathways. J Physiol 2001;533(Pt 1):263-272.
17. Jain RK. Determinants of tumor blood flow: a review. Cancer Res 1988;48(10):2641-2658.

18. Ribatti D, Vacca A, Presta M. The discovery of angiogenic factors: a historical review. Gen Pharmacol 2000;35(5):227-231.
19. Fornari FA, Randolph JK, Yalowich JC, Ritke MK, Gewirtz DA. Interference by doxorubicin with DNA unwinding in MCF-7 breast tumor cells. Mol Pharmacol 1994;45(4):649-656.
20. Momparler RL, Karon M, Siegel SE, Avila F. Effect of adriamycin on DNA, RNA, and protein synthesis in cell-free systems and intact cells. Cancer Res 1976;36(8):2891-2895.
21. Farber S, Diamond LK. Temporary remissions in acute leukemia in children produced by folic acid antagonist, 4-aminopteroyl-glutamic acid. N Engl J Med 1948;238(23):787-793.
22. McGuire WP, Rowinsky EK, Rosenshein NB, Grumbine FC, Ettinger DS, Armstrong DK, Donehower RC. Taxol: a unique antineoplastic agent with significant activity in advanced ovarian epithelial neoplasms. Ann Intern Med 1989;111(4):273-279.
23. Chabner BA, Roberts TG, Jr. Timeline: Chemotherapy and the war on cancer. Nat Rev Cancer 2005;5(1):65-72.
24. Dy GK, Adjei AA. Systemic cancer therapy: evolution over the last 60 years. Cancer 2008;113(7 Suppl):1857-1887.
25. Chaplin DJ, Pettit GR, Parkins CS, Hill SA. Antivascular approaches to solid tumour therapy: evaluation of tubulin binding agents. Br J Cancer Suppl 1996;27:S86-88.
26. Tozer GM, Kanthou C, Lewis G, Prise VE, Vojnovic B, Hill SA. Tumour vascular disrupting agents: combating treatment resistance. Br J Radiol 2008;81 Spec No 1:S12-20.
27. Leach MO, Brindle KM, Evelhoch JL, Griffiths JR, Horsman MR, Jackson A, Jayson GC, Judson IR, Knopp MV, Maxwell RJ, McIntyre D, Padhani AR, Price P, Rathbone R, Rustin GJ, Tofts PS, Tozer GM, Vennart W, Waterton JC, Williams SR, Workman P. The assessment of antiangiogenic and antivascular therapies in early-stage clinical trials using magnetic resonance imaging: issues and recommendations. Br J Cancer 2005;92(9):1599-1610.
28. Wedge SR, Kendrew J, Hennequin LF, Valentine PJ, Barry ST, Brave SR, Smith NR, James NH, Dukes M, Curwen JO, Chester R, Jackson JA, Boffey SJ, Kilburn LL, Barnett S, Richmond GH, Wadsworth PF, Walker M, Bigley AL, Taylor ST, Cooper L, Beck S, Jurgensmeier JM, Ogilvie DJ. AZD2171: a highly potent, orally bioavailable, vascular endothelial growth factor receptor-2 tyrosine kinase inhibitor for the treatment of cancer. Cancer Res 2005;65(10):4389-4400.
29. Yu H, Jove R. The STATs of cancer--new molecular targets come of age. Nat Rev Cancer 2004;4(2):97-105.
30. Bowman T, Broome MA, Sinibaldi D, Wharton W, Pledger WJ, Sedivy JM, Irby R, Yeatman T, Courtneidge SA, Jove R. Stat3-mediated Myc expression is required for Src transformation and PDGF-induced mitogenesis. Proc Natl Acad Sci U S A 2001;98(13):7319-7324.
31. Bowman T, Garcia R, Turkson J, Jove R. STATs in oncogenesis. Oncogene 2000;19(21):2474-2488.

32. Niu G, Bowman T, Huang M, Shivers S, Reintgen D, Daud A, Chang A, Kraker A, Jove R, Yu H. Roles of activated Src and Stat3 signaling in melanoma tumor cell growth. Oncogene 2002;21(46):7001-7010.
33. Dang CV. c-Myc target genes involved in cell growth, apoptosis, and metabolism. Mol Cell Biol 1999;19(1):1-11.
34. Semenza GL. Targeting HIF-1 for cancer therapy. Nat Rev Cancer 2003;3(10):721-732.
35. Hedvat M, Huszar D, Herrmann A, Gozgit JM, Schroeder A, Sheehy A, Buettner R, Proia D, Kowolik CM, Xin H, Armstrong B, Bebernitz G, Weng S, Wang L, Ye M, McEachern K, Chen H, Morosini D, Bell K, Alimzhanov M, Ioannidis S, McCoon P, Cao ZA, Yu H, Jove R, Zinda M. The JAK2 inhibitor AZD1480 potently blocks Stat3 signaling and oncogenesis in solid tumors. Cancer Cell 2009;16(6):487-497.

CHAPTER IV

CANCER IMAGING

Overview

As with the treatments described previously in Chapter III, there are imaging techniques that are designed to be sensitive to particular aspects of a disease state such as cancer. Imaging has an important role in cancer therapy in that it offers a relatively non-invasive method for tracking the response to certain therapies. In this work, two MRI based methods, dynamic contrast enhanced-MRI (DCE-MRI) and diffusion weighted-MRI (DW-MRI), are used to look specifically at the cellular and vascular aspects of cancer.

DCE-MRI

One technique that has been shown to be sensitive to changes in physiological characteristics of tumor vasculature including perfusion, blood vessel permeability, blood volume, and the extravascular extracellular volume fraction, is DCE-MRI (1,2). This technique characterizes the pharmacokinetics of an injected contrast agent as it enters and exits a region or tissue of interest (ROI/TOI). Typical, MRI contrast agents are based on gadolinium (Gd) chelates, as discussed previously in Chapter II. Recall that as the CA interacts with the surrounding tissue, the longitudinal relaxation time will shorten, leading to a signal intensity increase on a T_1-weighted image. By acquiring T_1-weighted images of the MRI signal over time, the kinetics of the CA can be modeled, and

biologically relevant parameters can be extracted that represent changes in, for example, blood flow, permeability, and tissue volume fractions. For this type of quantification, three main components, which will be discussed in further detail below, are required: 1) a T_1 map prior to the injection of the CA (discussed in Chapter II), 2) serial T_1-weighted images acquired during the injection, and 3) the vascular or arterial input function (VIF/AIF).

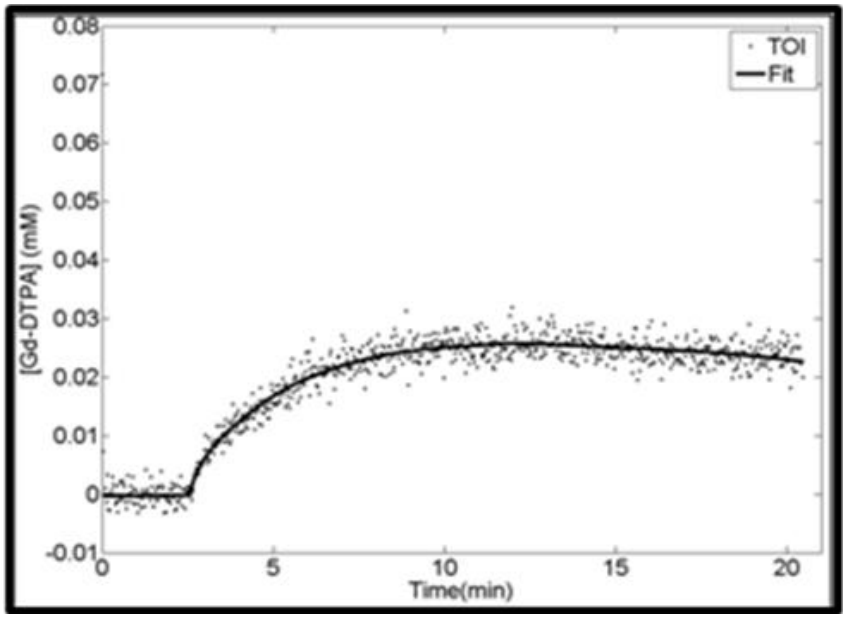

Fig. IV-1. An example of the change in concentration within the tissue of interest over time. The (.) represent actual data while the solid line represents the model fit to this data.

Each image acquisition represents one time point, and the resulting TIC from each voxel can be analyzed with a mathematical model. Fig. IV-1 demonstrates an example time intensity curve (TIC) selected from a voxel within the tumor. Since the kinetics of the CA depend on the physiological characteristics of the tissue, pathological conditions such as cancer show distinct differences from that of normal tissue. This observation can be exploited in order to diagnose cancer and monitor treatment.

Dynamic Acquisition

In order to observe the T_1 changes induced by the injected CA, T_1-weighted images must be acquired before, during, and after the injection. As with any MR imaging protocol, trade-offs exist between temporal resolution, spatial resolution, and signal to noise. In oncology applications, it is important to cover as much of the lesion volume as possible; in addition, the acquisition must be rapid enough to characterize the CA kinetics in a heterogeneous tumor region. Typical temporal resolutions can range from 1-30 seconds, depending on the application. If modeling tumor CA kinetics on a voxel-by-voxel basis to map tumor heterogeneity is required, then spatial resolution must be high enough to probe the details of the lesion. However, increasing the spatial resolution necessarily limits the temporal resolution and signal-to-noise of the acquired data. Thus, the relative importance of temporal resolution, spatial resolution, and signal-to-noise (SNR) is dependent on the goals of the study; considerations for these trade-offs will be discussed in the following section.

Vascular/Arterial Input Function

In order to perform a quantitative analysis of DCE-MRI data, knowledge of the kinetics of the CA in the plasma blood (vascular/arterial input function or VIF/AIF[1]) is required. While this is not a unique problem to DCE-MRI, technical demands make accurate quantification of the VIF/AIF difficult. Typical characteristics of the VIF/AIF from a bolus injection include a rapid wash-in of high CA concentration (*A*), followed by

[1] In this work VIF and AIF are used interchangeably; however the two do have a subtle difference. The VIF describes the time course of concentration of CA in the vasculature, whereas the AIF refers only to the arterial concentration. At early time points, the arterial and venous concentrations differ, but later the concentration equilibrates; hence, the changes in the blood pool examined in this work focus mainly on arterial concentrations but can be generalized in terms of a vascular input function.

a short-lived peak concentration value (*B*), and an exponentially decaying wash-out period (*C*) as shown in the VIF/AIF in Fig. VI-2.

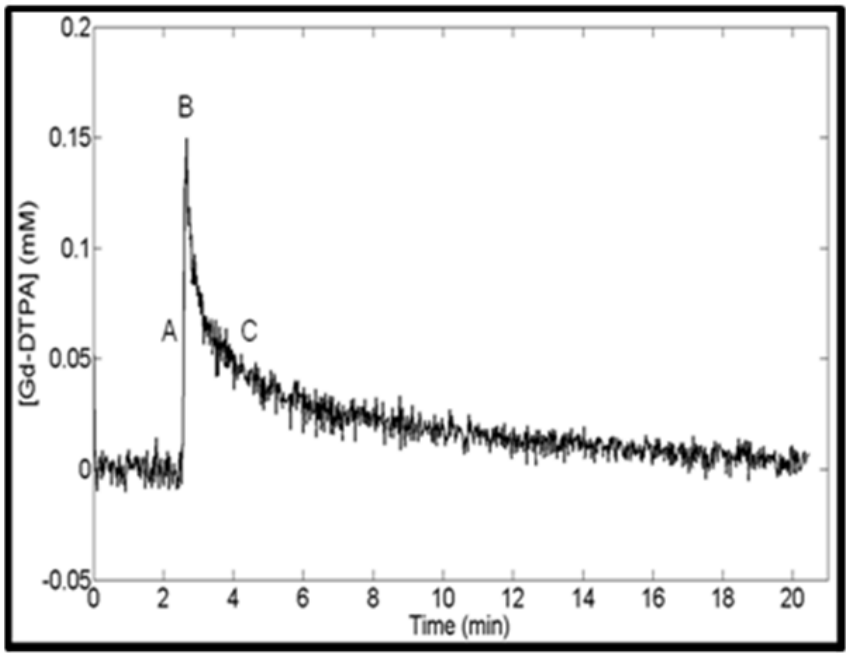

Fig. IV-2. An example of a typical vascular input function obtained from the left ventricle of the mouse. (A) illustrates the rapid rise during a bolus injection of contrast agent while (B) depicts the peak amplitude of measured contrast agent concentration and (C) shows the wash-out of the CA as it diffuses to the tissue.

Capturing the peak is one of the most critical and most difficult tasks due to the need for rapid sampling (1-2 seconds) and high SNR. Several techniques for obtaining the VIF/AIF are discussed. The current "gold standard" for measuring the VIF/AIF is taking arterial blood samples during the imaging acquisition (3,4). Very accurate VIF/AIFs can be obtained with this method in that CA concentration can be determined directly from these samples. However, the invasive nature of this method is a substantial drawback. To characterize the rapid rise and wash-out of the CA in the blood, obtaining blood samples at a high enough temporal resolution is also very difficult. For preclinical studies with mice, the typical blood volume of a mouse is ~ 2 mL; thus, the number of blood samples that can be obtained is quite limited.

Another method for estimating the VIF/AIF is derived from the image data itself. By strategically positioning the field of view to include a large vessel or left ventricle of the heart, the signal from the blood can be converted to describe the changing concentration of the CA during the injection. While this technique is certainly less invasive than blood sampling, it requires the presence of a blood pool in the field of view, which is not always conveniently located near the lesion of interest. Additionally, care must be taken to avoid partial volume or flow effects when measuring the VIF/AIF in this manner. As mentioned above, rapid scanning is required to capture the VIF/AIF peak (seen in Fig. IV-2) and this results in lower spatial resolution and/or lower SNR. Also, in high concentrations, such as that seen during the first pass of the CA bolus, T_2^* effects can diminish the measured MR signal in the image, providing an inaccurate estimation of the peak CA concentration in the blood. T_2* decay occurs due to field inhomogeneities and by introducing a large bolus of CA, such inhomogeneities can dampen the signal from T_1 dramatically (5). Dosage and imaging parameters (*TE*, gradient spoiler amplitude, etc.) should be optimized to eliminate T_2^* effects. An example of this effect is shown in Fig. IV-3.

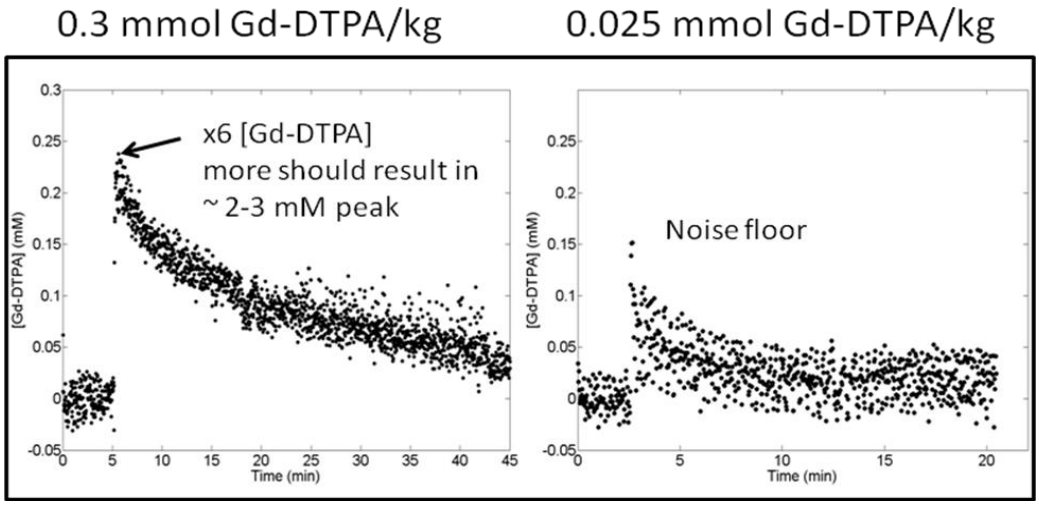

Fig. IV-3. Example time courses using two different doses, 0.3 mmol Gd-DTPA/kg (**a**) and 0.025 mmol Gd-DTPA/kg (**b**). At high doses, T_2* effects can diminish the apparent peak concentration while doses that are too low cannot be distinguished from the noise floor.

If arterial input functions are measured from the left ventricle of a heart (in this case, from a mouse), dose optimization is critical. If the concentration is too high, as seen with a 0.3 mmol/kg injection of Gd-DTPA, the signal will be severely diminished but if the dose is too low, the signal-to-noise will not be enough to differentiate the signal from background noise. Some sequences have been designed to measure both T_1 and T_2^* relaxation during a dynamic scan such that the effect of T_2^* can be quantified and corrected at the expense of temporal resolution (6).

Alternatively, "reference region" (RR) approaches have been applied to DCE-MRI techniques if a large vessel or blood pool is not present in the field of view (7-9). Specifically, if a sample of tissue is well-characterized (i.e., muscle), the time course from that tissue can be used to calibrate the signal from the region of interest and the need for estimating the VIF/AIF is eliminated with this technique. The high temporal resolution required to accurately capture the VIF/AIF can now be used to increase spatial

resolution, which improves the ability to probe tumor heterogeneity. Studies with a RR model have reported both good correlation with blood sampling analysis (10) as well as reasonable repeatability (11) and reproducibility (12). However, if the reference region shows much variability, or is poorly characterized, the accuracy of the approach suffers.

Because of the difficulty associated with measuring the VIF/AIF, many studies have used a cohort of similar subjects to obtain a population average VIF/AIF (13,14). The population average VIF/AIF is then applied to other similar subjects in additional studies. An example of this approach is shown in Fig. IV-4, where five mice were imaged on separate days. The group averaged, or population, VIF/AIF is displayed in black.

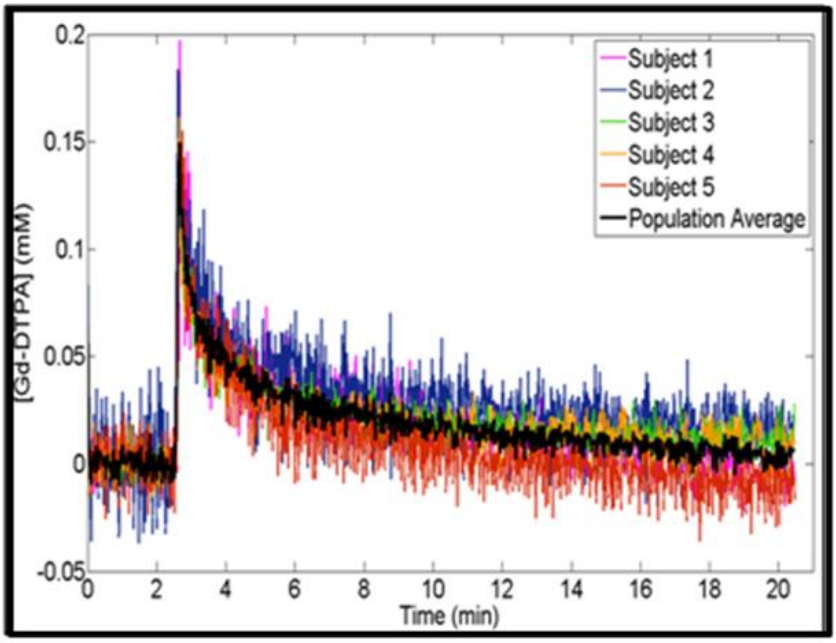

Fig. IV-4. Multiple arterial input functions measured from the left ventricle of five mice. The black line depicts the population average of this cohort of mice.

If a population VIF/AIF is used, the temporal resolution required to capture the kinetics of the individual VIF/AIF can now be "traded" for addition spatial resolution and/or signal-to-noise for the region of interest since changes in tissue are much slower than changes in the blood. Thus, during subsequent studies, spatial resolution can be

increased, and the population VIF/AIF can be used to drive the kinetic modeling. However, the obvious drawback to this technique is the inter- and intra-subject variability that may induce systematic errors in the pharmacokinetic parameters extracted from the models. When pursuing this technique, physical variation between subjects must be minimal, and DCE-MRI protocol set-ups must be identical to that used in obtaining the population-derived VIF/AIF; this method will be discussed in detail in subsequent chapters.

Modeling

Mathematical models are frequently employed to understand and quantify underlying physiology. Models for contrast agents have been developed that describe the introduction, distribution, and clearance of the agent within the body; specifically for DCE-MRI, extravasation of the CA in tissue can indicate physiologic parameters such as blood flow, vessel wall permeability, and tissue volume fractions of the tissue (1). The most commonly used model, developed by Kety in 1951, divides the body into two compartments: the blood/plasma space (denoted by C_p) and the tissue space (denoted by C_t) as shown in Fig. IV-5 (15).

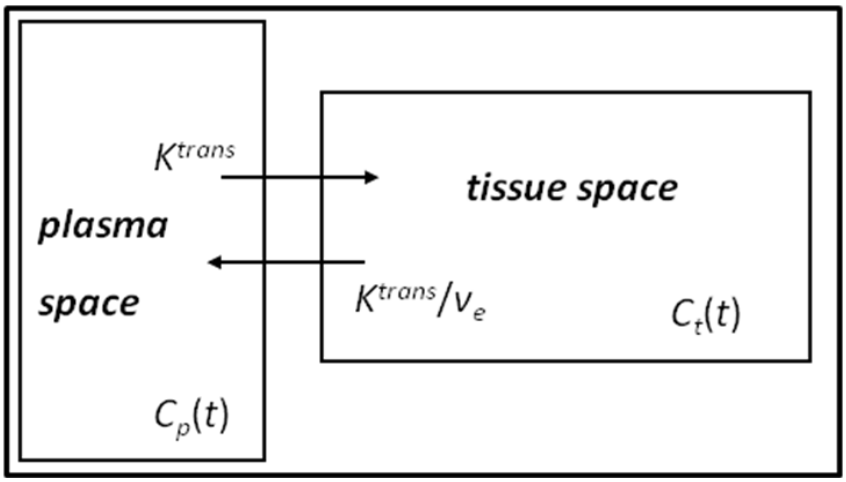

Fig. IV-5. Two compartment model showing one compartment representing the plasma space while the other compartment is the tissue space. The contrast agent leaves the plasma space at a rate represented by K^{trans} and returns by K^{trans}/v_e.

Using the notation standardized for DCE-MRI by Tofts *et al*, in 1999, K^{trans} represents the transfer constant from the plasma space to the tissue space (5). This transfer constant has different physiologic interpretations depending on factors such as permeability and blood flow for the tissue of interest. This process can be described in four ways: 1) flow limited (areas with high permeability); 2) permeability-vessel surface area (*PS*) limited (areas with low permeability); 3) mixed flow and *PS*; and 4) clearance. Under each of these conditions, the definition of the transfer constant K^{trans} changes. For example, in highly permeable areas, K^{trans} is governed by the flow (*F*) of the CA in the plasma fraction of the blood (1-hematocrit) and can be defined as $K^{trans} = F \cdot \rho \cdot (1\text{-}Hct)$, where ρ is tissue density, and *Hct* is the hematocrit. Similarly, if permeability limits extravasation, K^{trans} is then defined as the product of vessel permeability and surface area for the given tissue ($PS \cdot \rho$). In the mixed case, K^{trans} is defined as the extraction fraction, *E* ($= 1\text{-}e^{(-PS/F(1-Hct))}$) times $F \cdot \rho \cdot (1\text{-}Hct)$. For tumors, *PS* limited or mixed models most likely best describe CA extravasation from the characteristic leaky vasculature (1). Contrast agents of different molecular size can also force specific weighting on K^{trans}. Smaller

agents are more permeable so the predominant component affecting K^{trans} is flow while larger agents are slower to extravasate, allowing K^{trans} to reflect vessel permeability. An example of the use of a larger agent is presented below.

If we assume that a homogeneous distribution of CA exists in both compartments and there exists no back flux to either compartment, then any of the above cases can be generalized into a linear, first order ordinary differential equation describing CA kinetics into the tissue

$$\frac{d}{dt}C_t(t) = K^{trans} \cdot C_p(t) - (K^{trans}/v_e) \cdot C_t(t). \qquad \text{(IV-1)}$$

This equation can then be solved using (for example) the Laplace Transform, resulting in

$$C_t(t) = K^{trans} \cdot \int_0^t C_p(u) \cdot e^{-(K^{trans}/v_e)(t-u)} du. \qquad \text{(IV-2)}$$

It is important to note that the term (*1-Hct*) has been applied to the blood pool to indicate the portion of the blood, $C_b(t)$, that is well-mixed with the CA; $C_p(t)$ represents the [CA] in the plasma space $(1\text{-}Hct)\cdot C_b(t)$; thereby, the K^{trans} interpretations above have been simplified.

The aforementioned mathematical model neglects the fraction of tissue that may contain vascular space. Investigators have shown that in some tissues such as muscle, the fraction of vascular space (v_p) is so small (~0.02) that it can be considered negligible (16-18). However, some investigators argue that tumor tissue may contain a non-trivial fraction of vascular space due to angiogenesis. If v_p is ignored for a tissue that contains significant vascular space, the pharmacokinetic modeling will overestimate K^{trans}, leading to erroneous results. An illustration of this extension has been adapted by Daldrup *et al*,

shown in Fig. IV-6, and has been used by other investigators (19,20).

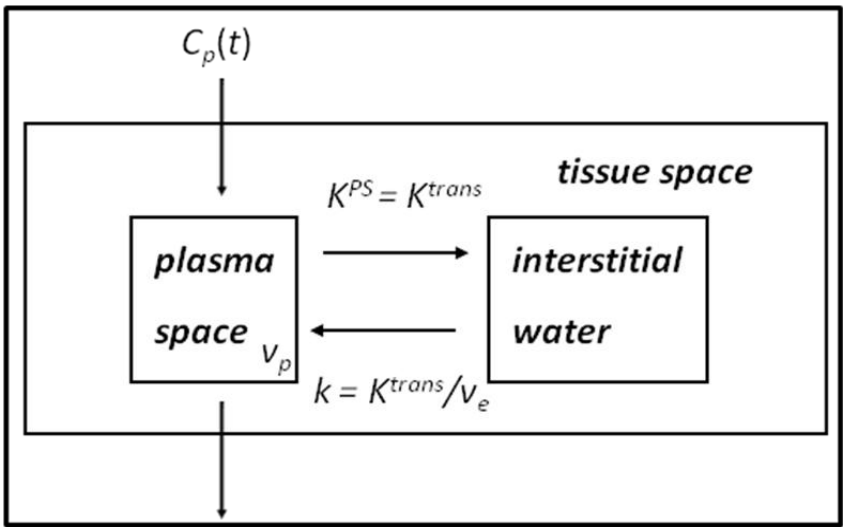

Fig. IV-6. Two compartment model showing one compartment representing the plasma space while the other compartment is the tissue space. Now, however, the tissue space is comprised of both plasma and interstitial components.

An extension of the two-compartmental model has been formalized to improve accuracy in highly vascularized tissues such that the tissue space is composed of not only extravascular extracellular space but also a plasma space, described by:

$$C_t(t) = K^{trans} \cdot \int_0^t C_p(u) \cdot e^{-(K^{trans}/v_e)(t-u)} du + v_p \cdot C_p(t) . \qquad \text{(IV-3)}$$

Now, C_t is not only composed of the concentration of CA in the extravascular extracellular space (C_e) x v_e, but also an additional plasma component within the tissue (C_p x v_p); i.e., $C_t = v_e \cdot C_e + v_p \cdot C_p$. (We note that the contrast agents used in this study are strictly extracellular, so there that the concentration in the intracellular space, v_i, is zero.) In these forms, if $C_p(t)$ is measured, K^{trans}, v_e, (and v_p) can be determined using a nonlinear least squares fit to the collected data, $C_t(t)$. This analysis can be done on a voxel-by-voxel basis in order to produce parametric maps.

Applications

By employing both the standard and extended two compartmental model described above, quantitative measures of K^{trans} and v_e can provide valuable information regarding the efficacy of anti-cancer drugs. For example, Checkley, *et al* examined both drug efficacy and dose-dependent response using DCE-MRI parameters as primary metrics (21). ZD6474 is a VEGF receptor 2 (KDR) tyrosine kinase inhibitor that prevents endothelial migration and proliferation (22,23). In this study, athymic mice were inoculated with PC-3 human prostate adenocarcinoma xenografts on the hind limb. After reaching approximately 1.0 cm^3, the mice were divided into controls that received a vehicle treatment and mice that received a dose of ZD6474; this study was repeated for doses ranging from 12.5, 25, 50, and 100 mg/kg, administered in two doses at time 0 hr and 22 hours. DCE-MRI data was collected pre-treatment and 24 hours post-treatment. Data were acquired at 4.7T; a saturation recovery experiment with *TR* values ranging from 120, 500, 2000, and 10000 ms (*TE* = 16 ms) was used to calibrate signal to pre-contrast T_1. The dynamic acquisition employed a spin echo sequence with a *TR/TE* = 120/10 ms, an acquisition matrix of 512 × 256 × 4 slices, resulting in a spatial resolution of 0.625 × 0.312 × 2 mm. At a temporal resolution of approximately 16 s, 5 baseline images were acquired, followed by a 0.01 mL/g dose of Gd-DTPA over a 3 s injection. Imaging continued for 11 more minutes for a total of 40 image sets. Relaxivity for Gd-DTPA was measured using mouse blood samples dosed with known concentrations of Gd-DTPA and the VIF/AIF was obtained from another set of mice (physiologically identical) and fit to a bi-exponential decay. A reproducibility study was also done using

11 vehicle controls. It was found that there was no significant difference between K^{trans} (P = 0.4) and v_e (P = 0.1) as measured on the same animal during two different imaging sessions. No change in growth was reported during the 24 hours treatment study; however, a significant reduction in K^{trans} for doses $\geq$ 25 mg/kg and in v_e for doses > 50 mg/kg were identified. Chronic dose yielded significant volumetric difference at day 11. Since K^{trans} was not significantly different at 12.5 mg/kg and significant changes in K^{trans} between doses were demonstrated, the authors suggest that K^{trans} is dose-dependent. This study illustrates the utility of DCE-MRI in anti-angiogenic treatment studies at early response time.

As explained in the previous section, depending on the vascular environment, modeling can be flow-limited, permeability-limited, or mixed. The use of macromolecular rapid clearance blood flow agent that is larger and therefore crosses the endothelium more slowly can be used to control the weighting of flow and permeability on K^{trans}. In Bradley *et al* (24), gadomelitol with a molecular weight of 6.47 kDa (as opposed to the frequently used Gd-DTPA, with a molecular weight of 0.5 kDa), was used to model components of the tissue curve that represented flow and permeability in order to explore the effects of two anti-angiogenic drugs, AZD 2171 and vandetanib. AZD 2171 and vandetanib both inhibit VEGF receptor type 2 tyrosine kinases and have previously shown a drastic reduction in tumor blood flow and permeability (23,25). Nineteen male athymic AP rats were inoculated with SW620 colorectal adenocarcinoma tumor cells on the forelimb flank (dorsal to the heart). After 10 days, 8 rats were treated with AZD 2171 (3 mg/kg), 8 rats were treated with vandetinib (50 mg/kg), 3 were treated with vehicle controls. All rats were treated again after 22 hours and were imaged pre- and

23 hr post-treatment. One of the emphasized points of this study was the meticulous imaging protocol. Tumors were placed just above the heart in order to capture both the region of interest as well as the left ventricle of the heart to capture the VIF/AIF. Imaging was performed at 4.7T and a semi-keyhole technique (sampling only a portion of *k*-space) was incorporated to improve temporal resolution (26). Gadomelitol gel phantoms of various concentrations were also included in the field of view to calibrate signal intensity to agent concentration. The dynamic acquisition was done with a SPGR sequence with *TR/TE* = 13/9/2.3 s, $\alpha = 15^0$, FOV = 60^2, and the acquisition matrix = 128 × 96. With these parameters, a temporal resolution of 0.5 s/image was obtained; with this fine of a resolution, the rapid enhancing VIF/AIF in the left ventricle was adequately sampled for each subject. Baseline images were taken for 15 s, followed by a bolus injection of 0.045 mmol/kg of CA over 2-3 s with 5 minutes of additional imaging. The VIF/AIF peaked at approximately 1.15 mM of CA for all animals. The extended two compartmental model (with v_p term) was used, and the tissue curves were analyzed such that F/v_T, v_p, and $PS{\cdot}\rho$ where F, v_p, P,S, and ρ have been defined in the previous section and v_t is the total volume of the image voxel. Animals that were treated with the angiogenic drug show significant changes in vascular related parameters, $PS{\cdot}\rho$ (19.7 ± 9.5% and 28.9 ± 14.1%) and v_p (31.2 ± 19.1% and 54.8 ± 21%) while no effect was seen in F/v_T. This study explored the use of a larger molecular weight contrast agent to discern effects on permeability and blood flow on anti-angiogenic drugs. Furthermore, an imaging protocol was designed, optimized and strictly adhered to in order to help minimize parametric variability.

DW-MRI

Introduction

As mentioned previously, the majority of MRI applications use magnetic fields and radiofrequency energy to acquire signals from the hydrogen nuclei contained in tissue water. While the contrast in MRI is typically due to variations in the nuclei density and relaxation, the mobility or diffusion, of this water can also be probed to extract information about cellularity.

Physical Basis

Self-diffusion or Brownian motion is due to the microscopic random walk of water molecules (27). In a system that is defined by small compartments, such as cells, that are separated by semipermeable barriers, such as cell membranes, the rate of this self diffusion, which is also described as the apparent diffusion coefficient (*ADC*), depends on the spatial relationship between these barriers (28-30). Hence, the cell membranes act to restrict the diffusion of water molecules.

Techniques such as a pulsed-gradient spin-echo (PGSE) sequence have been designed to be sensitive to this diffusion and the effects of restrictions on water movements at spatial scales up to the order of several microns; this spatial scale is on the order of the diameter of a cell and therefore can be used as an estimate of cellularity.

Consider a spin at a particular position x with gyromagnetic ratio γ, precessing in the transverse plane about magnetic field $\boldsymbol{B}$ in the z-direction ($\boldsymbol{B}_z$). At its current position, the

spin is labeled by magnetic field gradient, ***G***, applied in the *x*-direction, and accumulating phase, ϕ, over time, δ, described by

$$\varphi_1 = \gamma \int_0^{\delta} G_x x_1 dt = \gamma G_x x_1 \delta . \qquad \text{(IV-4)}$$

If a magnetic field gradient, equal in magnitude to the first, is applied in the opposite direction some time later, Δ, the spin will experience a different phase accumulation described by

$$\varphi_2 = \gamma \int_{\Delta}^{\Delta+\delta} G_x x_2 dt = \gamma G_x x_2 \delta . \qquad \text{(IV-5)}$$

If the spin undergoing these two pulses remains stationary (i.e., $x_1=x_2$), then there will be no net phase ($\varphi_2 - \varphi_1 = 0$); however, if the spin moves ($x_1 \neq x_2$), then there is a net phase displacement. This phenomena is demonstrated in Fig. IV-7.

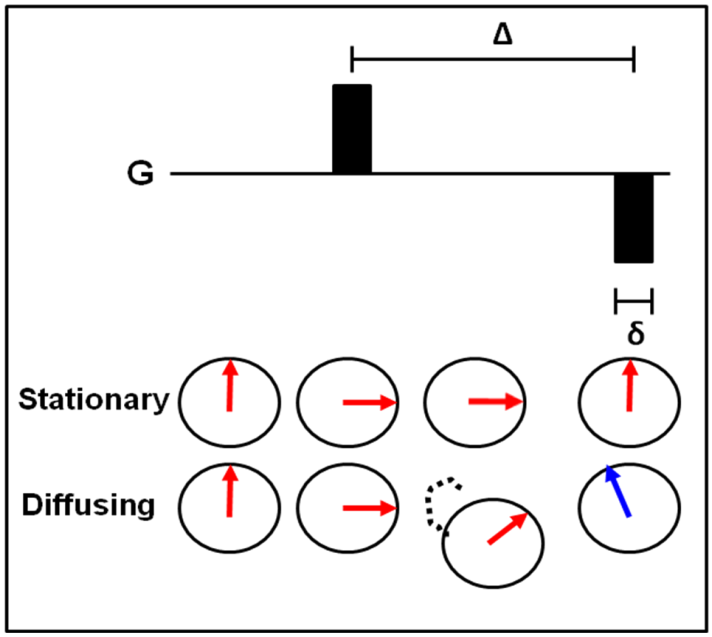

Fig. IV-7. As the spins are labeled by the first magnetic field gradient, a spin may diffuse, accumulating some phase. As the second magnetic field gradient (equal in magnitude but opposite in direction), is applied, spins that have not moved will acquire no net phase displacement while spins that have diffused will not acquire a net phase displacement.

If we extend this model to a large number of spins which is assumed to have a Gaussian distribution of phase displacement, the total diffusion weighting imparted on the spins by both the imaging- and diffusion-sensitizing gradients, denoted as *b-value* or *b*, can be described (details provided elsewhere (5)) as

$$b_{ij} = \gamma^2 \delta^2 G_i G_j ADC\left(\Delta - \frac{\delta}{3}\right), \qquad \text{(IV-6)}$$

where *ADC* is the apparent diffusion coefficient of the molecule in question. Based on Einstein's equation,

$$\left\langle r^2 \right\rangle = 2Dt, \qquad \text{(IV-7)}$$

if the diffusivity (*D*) of free water at body temperature is ~ 2.5 $\mu m^2/ms$, within an interval of approximately 35 ms (*t*), water will move ~ 13 μm ($<r^2>$), which is approximately the size of a cell. Thus, by adjusting the timing of a DW-MRI sequence, an estimation of cellularity can be determined based on the presence of cellular membranes.

Modeling

By recalling the spin echo equation from a previous chapter, the signal depends on proton density, T_1, and T_2 relaxation. During a diffusion experiment, the signal will change due to diffusion as well and now the signal can be described as

$$S = S_0 \cdot (1 - e^{-TR/T_1}) \cdot e^{-TE/T_2} \cdot e^{-ADC \cdot b}, \qquad \text{(IV-8)}$$

where *b* is given by (IV-6). If *TR* is set to a value greater than that of the T_1 of the tissue of interest and *TE* is minimized to shorter than the T_2 of the tissue of interest, then the signal will be dependent on diffusion

$$S = S_0 \cdot e^{-ADC \cdot b}. \qquad \text{(IV-9)}$$

By changing the magnitude or duration of the diffusion gradients, thus changing the *b*-values, and acquiring multiple image sets, the data can be exponentially fit to acquire *ADC* values on a voxel by voxel basis, as shown in Fig. IV-8.

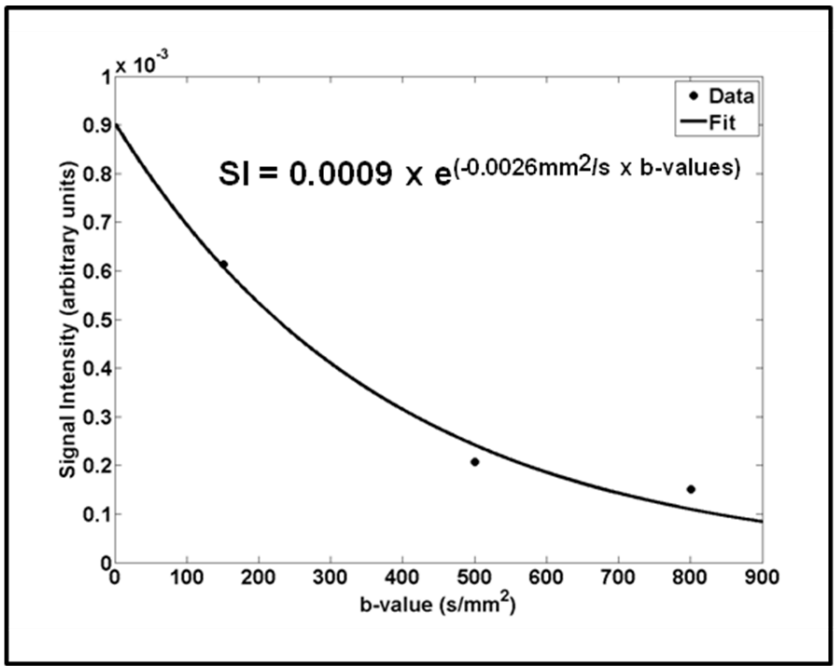

Fig. IV-8. A mono-exponential fit to diffusion data acquired at three different *b*-values. This fit returned a value of 0.0026 mm^2/s as the ADC value of the sample.

Applications

Because of its high sensitivity, DW-MRI has also been used to monitor treatment response in a variety of anti-cancer therapies, including both cytotoxic and anti-vascular/anti-angiogenic drugs (31-33). However, the specific changes in tissue that lead to these changes in *ADC* are not fully understood, and other processes can lead to increases or decreases in *ADC*. Changes in active transport, blood flow or perfusion and bulk motion can potentially confound *ADC* measures as a surrogate for cell density (34). Additionally, tissue organization also contributes to the water movement. For example, an area that is densely packed with tumor cells will have a reduced *ADC* value due to the increase in cell membranes present, but if the an area with sparse tumor cells has

increased extracellular matrix (ECM), ECM components, or macrophage activity lending to an increase in extracellular space tortuosity, a reduced *ADC* value may also be reported (34). As the cellular and extracellular environments change during the course of treatment, *ADC* has been used extensively to report areas of increasing necrosis and even malignancy grade (31,35).

Correlations with *ADC* maps and tumor cellularity have been demonstrated (36-41). Subsequently, maps of *ADC* have also been used to examine treatment response in a variety of types of tumors, in both preclinical and clinical settings. In one study, DW-MRI was used to predict treatment outcome for a high grade brain tumor model. After 10-12 days after tumor inoculation, rats were imaged using a diffusion-weighted sequence to obtain an *ADC* map of multiple slices of the tumor. After several baseline scans were acquired, 13 animals were treated while 20 animals were not; all animals were imaged every two days following baseline scans for approximately 20 days. The results of this study found that diffusion measurements were significantly sensitive to therapy-induced changes (42).

In another study, DW-MRI was used to assess treatment efficacy of a vascular disrupting treatment regime. Seventeen male adult rats were implanted with two rhabdomyosarcoma tumor fragments on each flank. After the tumors reached approximately 2 cm^3, 14 rats were placed a group receiving an intraperitoneal dose of 25 mg/kg of combretastatin A4 phosphate (Oxigene, Watertown, MA), which is a vascular disrupting agent similar to those treatments described in Chapter III, while three rats were used as controls receiving saline injections. Rats were imaged 1 hour, 6 hours, and 2 days after treatment (or saline) administration, sacrificing three rats at each time point.

Anatomical and contrast enhanced images were acquired at 1.5T in addition to the DW-MRI protocol. The DW-MRI protocol included an echo planar imaging scheme with the following parameters: TR/TE/NEX: 3300 ms/124 ms/4, acquisition matrix = 96 × 192 for a FOV = 81.3 mm × 130 mm (with 20 sections at a thickness = 0.2 mm with 0.2 mm gap), and b-values = 0, 50, 100, 150, 200, 250, 300, 500, 750, and 1000 s/mm^2. *ADC* maps were created using all b-values in addition to separate *ADC* maps to differentiate perfusion and diffusion effects; low b-values were used to create *ADC* maps that reflected perfusion while the high b-values created *ADC* maps that reflected water movement from diffusion. The results of this study demonstrate the transient change in *ADC* in response to treatment. Average *ADC* for the entire tumor showed an initial decrease immediately (1hr and 6hrs) post-treatment while at day 2, *ADC* increased significantly. Histology showed that this was due to the collapse of vasculature and subsequent crowding of endothelial cells into the extracellular space; at day 2, the high *ADC* reflects areas of developed necroses (43).

References

1. Tofts PS, Brix G, Buckley DL, Evelhoch JL, Henderson E, Knopp MV, Larsson HB, Lee TY, Mayr NA, Parker GJ, Port RE, Taylor J, Weisskoff RM. Estimating kinetic parameters from dynamic contrast-enhanced T(1)-weighted MRI of a diffusable tracer: standardized quantities and symbols. J Magn Reson Imaging 1999;10(3):223-232.
2. Yankeelov TE, Gore JC. Contrast enhanced magnetic resonance imaging in oncology: data acquisition, analysis, and examples. Current Medical Imaging Reviews 2007;3:91-107.
3. Fritz-Hansen T, Rostrup E, Larsson HB, Sondergaard L, Ring P, Henriksen O. Measurement of the arterial concentration of Gd-DTPA using MRI: a step toward quantitative perfusion imaging. Magn Reson Med 1996;36(2):225-231.
4. Larsson HB, Stubgaard M, Frederiksen JL, Jensen M, Henriksen O, Paulson OB. Quantitation of blood-brain barrier defect by magnetic resonance imaging and gadolinium-DTPA in patients with multiple sclerosis and brain tumors. Magn Reson Med 1990;16(1):117-131.
5. Haacke M, Brown R, Thompson M, Venkatesan R, Haacke M, Brown R, Thompson M, Venkatesan R. Magnetic Resonance Imaging: Physical Principles and Sequence Design: Wiley-Liss; 1999.
6. Heilmann M, Walczak C, Vautier J, Dimicoli JL, Thomas CD, Lupu M, Mispelter J, Volk A. Simultaneous dynamic T1 and T2* measurement for AIF assessment combined with DCE MRI in a mouse tumor model. Magma 2007;20(4):193-203.
7. Kovar DA, Lewis M, Karczmar GS. A new method for imaging perfusion and contrast extraction fraction: input functions derived from reference tissues. J Magn Reson Imaging 1998;8(5):1126-1134.
8. Yankeelov TE, Luci JJ, Lepage M, Li R, Debusk L, Lin PC, Price RR, Gore JC. Quantitative pharmacokinetic analysis of DCE-MRI data without an arterial input function: a reference region model. Magn Reson Imaging 2005;23(4):519-529.
9. Yang C, Karczmar GS, Medved M, Stadler WM. Estimating the arterial input function using two reference tissues in dynamic contrast-enhanced MRI studies: fundamental concepts and simulations. Magn Reson Med 2004;52(5):1110-1117.
10. Yankeelov TE, Cron GO, Addison CL, Wallace JC, Wilkins RC, Pappas BA, Santyr GE, Gore JC. Comparison of a reference region model with direct measurement of an AIF in the analysis of DCE-MRI data. Magn Reson Med 2007;57(2):353-361.
11. Yankeelov TE, DeBusk LM, Billheimer DD, Luci JJ, Lin PC, Price RR, Gore JC. Repeatability of a reference region model for analysis of murine DCE-MRI data at 7T. J Magn Reson Imaging 2006;24(5):1140-1147.
12. Walker-Samuel S, Parker CC, Leach MO, Collins DJ. Reproducibility of reference tissue quantification of dynamic contrast-enhanced data: comparison with a fixed vascular input function. Phys Med Biol 2007;52(1):75-89.
13. Port RE, Knopp MV, Brix G. Dynamic contrast-enhanced MRI using Gd-DTPA: interindividual variability of the arterial input function and consequences for the assessment of kinetics in tumors. Magn Reson Med 2001;45(6):1030-1038.

14. Parker GJ, Barker GJ, Tofts PS. Accurate multislice gradient echo T(1) measurement in the presence of non-ideal RF pulse shape and RF field nonuniformity. Magn Reson Med 2001;45(5):838-845.
15. Kety SS. Peripheral blood flow measurements. Pharmacol Rev 1951;3:1-41.
16. Faranesh AZ, Kraitchman DL, McVeigh ER. Measurement of kinetic parameters in skeletal muscle by magnetic resonance imaging with an intravascular agent. Magn Reson Med 2006;55(5):1114-1123.
17. Shames DM, Kuwatsuru R, Vexler V, Muhler A, Brasch RC. Measurement of capillary permeability to macromolecules by dynamic magnetic resonance imaging: a quantitative noninvasive technique. Magn Reson Med 1993;29(5):616-622.
18. Kuwatsuru R, Shames DM, Muhler A, Mintorovitch J, Vexler V, Mann JS, Cohn F, Price D, Huberty J, Brasch RC. Quantification of tissue plasma volume in the rat by contrast-enhanced magnetic resonance imaging. Magn Reson Med 1993;30(1):76-81.
19. Daldrup H, Shames DM, Wendland M, Okuhata Y, Link TM, Rosenau W, Lu Y, Brasch RC. Correlation of dynamic contrast-enhanced MR imaging with histologic tumor grade: comparison of macromolecular and small-molecular contrast media. AJR Am J Roentgenol 1998;171(4):941-949.
20. de Lussanet QG, Beets-Tan RG, Backes WH, van der Schaft DW, van Engelshoven JM, Mayo KH, Griffioen AW. Dynamic contrast-enhanced magnetic resonance imaging at 1.5 Tesla with gadopentetate dimeglumine to assess the angiostatic effects of anginex in mice. Eur J Cancer 2004;40(8):1262-1268.
21. Checkley D, Tessier JJ, Kendrew J, Waterton JC, Wedge SR. Use of dynamic contrast-enhanced MRI to evaluate acute treatment with ZD6474, a VEGF signalling inhibitor, in PC-3 prostate tumours. Br J Cancer 2003;89(10):1889-1895.
22. Hennequin LF, Stokes ES, Thomas AP, Johnstone C, Ple PA, Ogilvie DJ, Dukes M, Wedge SR, Kendrew J, Curwen JO. Novel 4-anilinoquinazolines with C-7 basic side chains: design and structure activity relationship of a series of potent, orally active, VEGF receptor tyrosine kinase inhibitors. J Med Chem 2002;45(6):1300-1312.
23. Wedge SR, Ogilvie DJ, Dukes M, Kendrew J, Chester R, Jackson JA, Boffey SJ, Valentine PJ, Curwen JO, Musgrove HL, Graham GA, Hughes GD, Thomas AP, Stokes ES, Curry B, Richmond GH, Wadsworth PF, Bigley AL, Hennequin LF. ZD6474 inhibits vascular endothelial growth factor signaling, angiogenesis, and tumor growth following oral administration. Cancer Res 2002;62(16):4645-4655.
24. Bradley DP, Tessier JL, Checkley D, Kuribayashi H, Waterton JC, Kendrew J, Wedge SR. Effects of AZD2171 and vandetanib (ZD6474, Zactima) on haemodynamic variables in an SW620 human colon tumour model: an investigation using dynamic contrast-enhanced MRI and the rapid clearance blood pool contrast agent, P792 (gadomelitol). NMR Biomed 2008;21(1):42-52.
25. Wedge SR, Kendrew J, Hennequin LF, Valentine PJ, Barry ST, Brave SR, Smith NR, James NH, Dukes M, Curwen JO, Chester R, Jackson JA, Boffey SJ, Kilburn LL, Barnett S, Richmond GH, Wadsworth PF, Walker M, Bigley AL, Taylor ST, Cooper L, Beck S, Jurgensmeier JM, Ogilvie DJ. AZD2171: a highly potent,

orally bioavailable, vascular endothelial growth factor receptor-2 tyrosine kinase inhibitor for the treatment of cancer. Cancer Res 2005;65(10):4389-4400.
26. Kuribayashi H, Bradley DP, Checkley DR, Worthington PL, Tessier JJ. Averaging keyhole pulse sequence with presaturation pulses and EXORCYCLE phase cycling for dynamic contrast-enhanced MRI. Magn Reson Med Sci 2004;3(4):207-210.
27. Einstein A. Über die von der molekularkinetischen Theorie der Wärme geforderte Bewegung von in ruhenden Flüssigkeiten suspendierten Teilchen. 1905;322(8):549.
28. Stejskal EO, Tanner JE. Spin diffusion measurements: spin echoes in the presence of a time dependent field gradient. J Chem Phys 1965;42:288-292.
29. Le Bihan D, Breton E, Lallemand D, Aubin ML, Vignaud J, Laval-Jeantet M. Separation of diffusion and perfusion in intravoxel incoherent motion MR imaging. Radiology 1988;168(2):497-505.
30. Chenevert TL, Brunberg JA, Pipe JG. Anisotropic diffusion in human white matter: demonstration with MR techniques in vivo. Radiology 1990;177(2):401-405.
31. Patterson DM, Padhani AR, Collins DJ. Technology insight: water diffusion MRI--a potential new biomarker of response to cancer therapy. Nat Clin Pract Oncol 2008;5(4):220-233.
32. Thoeny HC, De Keyzer F. Extracranial applications of diffusion-weighted magnetic resonance imaging. Eur Radiol 2007;17(6):1385-1393.
33. Yankeelov TE, Lepage M, Chakravarthy A, Broome EE, Niermann KJ, Kelley MC, Meszoely I, Mayer IA, Herman CR, McManus K, Price RR, Gore JC. Integration of quantitative DCE-MRI and ADC mapping to monitor treatment response in human breast cancer: initial results. Magn Reson Imaging 2007;25(1):1-13.
34. Padhani AR, Liu G, Koh DM, Chenevert TL, Thoeny HC, Takahara T, Dzik-Jurasz A, Ross BD, Van Cauteren M, Collins D, Hammoud DA, Rustin GJ, Taouli B, Choyke PL. Diffusion-weighted magnetic resonance imaging as a cancer biomarker: consensus and recommendations. Neoplasia 2009;11(2):102-125.
35. Moffat BA, Hall DE, Stojanovska J, McConville PJ, Moody JB, Chenevert TL, Rehemtulla A, Ross BD. Diffusion imaging for evaluation of tumor therapies in preclinical animal models. Magma 2004;17(3-6):249-259.
36. Sugahara T, Korogi Y, Kochi M, Ikushima I, Shigematu Y, Hirai T, Okuda T, Liang L, Ge Y, Komohara Y, Ushio Y, Takahashi M. Usefulness of diffusion-weighted MRI with echo-planar technique in the evaluation of cellularity in gliomas. J Magn Reson Imaging 1999;9(1):53-60.
37. Hayashida Y, Yakushiji T, Awai K, Katahira K, Nakayama Y, Shimomura O, Kitajima M, Hirai T, Yamashita Y, Mizuta H. Monitoring therapeutic responses of primary bone tumors by diffusion-weighted image: Initial results. Eur Radiol 2006;16(12):2637-2643.
38. Guo Y, Cai YQ, Cai ZL, Gao YG, An NY, Ma L, Mahankali S, Gao JH. Differentiation of clinically benign and malignant breast lesions using diffusion-weighted imaging. J Magn Reson Imaging 2002;16(2):172-178.

39. Humphries PD, Sebire NJ, Siegel MJ, Olsen OE. Tumors in pediatric patients at diffusion-weighted MR imaging: apparent diffusion coefficient and tumor cellularity. Radiology 2007;245(3):848-854.
40. Squillaci E, Manenti G, Cova M, Di Roma M, Miano R, Palmieri G, Simonetti G. Correlation of diffusion-weighted MR imaging with cellularity of renal tumours. Anticancer Res 2004;24(6):4175-4179.
41. Manenti G, Di Roma M, Mancino S, Bartolucci DA, Palmieri G, Mastrangeli R, Miano R, Squillaci E, Simonetti G. Malignant renal neoplasms: correlation between ADC values and cellularity in diffusion weighted magnetic resonance imaging at 3 T. Radiol Med 2008;113(2):199-213.
42. Chenevert TL, McKeever PE, Ross BD. Monitoring early response of experimental brain tumors to therapy using diffusion magnetic resonance imaging. Clin Cancer Res 1997;3(9):1457-1466.
43. Thoeny HC, De Keyzer F, Chen F, Vandecaveye V, Verbeken EK, Ahmed B, Sun X, Ni Y, Bosmans H, Hermans R, van Oosterom A, Marchal G, Landuyt W. Diffusion-weighted magnetic resonance imaging allows noninvasive in vivo monitoring of the effects of combretastatin a-4 phosphate after repeated administration. Neoplasia 2005;7(8):779-787.

CHAPTER V

OPTIMIZATION OF A MURINE VASCULAR INPUT FUNCTION MRI ACQUISITION PROTOCOL

As discussed in chapter IV, the typical characteristics of the VIF from a bolus injection include a rapid wash-in of high CA concentration up to a sharp peak concentration and a bi-exponentially decaying wash-out period (see Figure IV-2). Capturing the first pass of the bolus is critical; previous literature suggests that if there is a 10% error in peak estimation, it will contribute to a 5-7% error in DCE-MRI parameters (1). However, it is extraordinarily difficult in small animals due to the need for high temporal as well as adequate spatial resolution.

To circumvent issues associated with other VIF acquisition protocols, some investigators measure the VIF using the imaging data itself. While this method is noninvasive, strategically including a blood pool in the field of view (FOV) can limit the location of the region of interest (ROI). Additionally, the spatial resolution must be high enough to minimize partial volume or flow effects, while the temporal resolution must be high enough to capture the peak of the VIF. Because of these requirements, SNR, the number of slices, and spatial resolution over the tumor are typically compromised. Because of the difficulties in obtaining a high-quality VIF from every subject at every time point, some investigators have used a population-averaged VIF for data analysis.

Typically, a cohort of patients or animals is used to obtain multiple individual VIFs, which are then averaged together to form a high-SNR population VIF (2-4). Then, the DCE-MRI treatment study is performed using a separate cohort, and the population

derived VIF is used for all subjects. Thus, the temporal resolution can be "traded" for higher spatial resolution and/or increased SNR, and the location of the imaging ROI becomes less important since a major vessel is not required in the FOV. This higher spatial resolution is particularly important when characterizing the heterogeneity of the tumor on a voxel by voxel basis.

In order to arrive at an accurate, population-derived VIF, a cohort of mice must be used to obtain a number of individually measured VIFs. The following work describes optimizations to an MRI protocol in order to accurately obtain multiple individual VIF data from the left ventricle in a cohort of mice.

Relaxivity

First, the relaxivities of the contrast agents used in subsequent experiments were determined. Phantoms for Gd-DTPA and P846 were constructed using five tubes of saline containing concentrations of 0, 0.25, 0.75, 1.5, and 4.5 mM (2.3 mM for P846). The inversion recovery snapshot FLASH (Fast Low Angle SHot) gradient echo sequence (described in greater detail below) was used with the following parameters: TR/TE = 12 s/2.12 ms, $\alpha = 15°$, NEX = 2, acquisition matrix = 64^2, and FOV = $(35\ mm)^2$ with a slice thickness of 2 mm. Twenty-two images at linearly spaced inversion times ranging from 10 ms to 10 s were collected. ROIs within each tube were fit to an inversion recovery equation in order to determine the R_1 of each concentration.

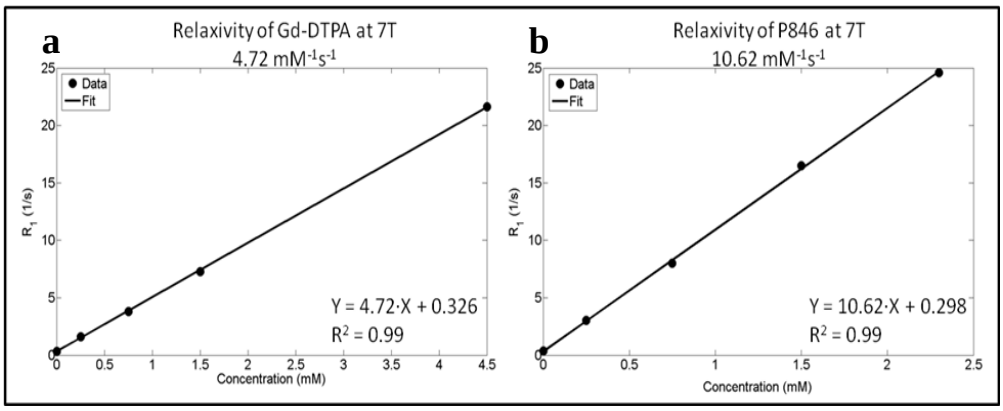

Fig. V-1. Relaxivity fits for Gd-DTPA (**a**) and P846 (**b**). Each point represents the measured R1 value for one of the five vials containing various concentrations of contrast agent. The solid line illustrates the linear fit to the data to extract the relaxivity (slope).

Fig. VI-1 shows the plot of the respective R_1 values for each vial concentration for each agent. Linear regression was performed on the data producing a slope that reflected the relaxivity for each agent at 7T of 4.72 $mM^{-1}s^{-1}$ for Gd-DTPA and 10.62 $mM^{-1}s^{-1}$ for P846. This experiment was also performed at 9.4T producing a relaxivity of 4.8 $mM^{-1}s^{-1}$ for Gd-DTPA.

Parametric Optimization

Once the relaxivity was determined, a spoiled gradient echo sequence was optimized to maximize the SNR, temporal and spatial resolution at 7T. First, the flip angle was determined to maximize the difference between signal from the tumor ($T_1 \approx 2.5$ s) and signal from blood containing contrast agent ($T_1 \approx 1.3$ s) to provide the highest contrast between these tissues of interest in this study. The signal for each of these two regions is plot over a range of flip angles in Fig. V-2.

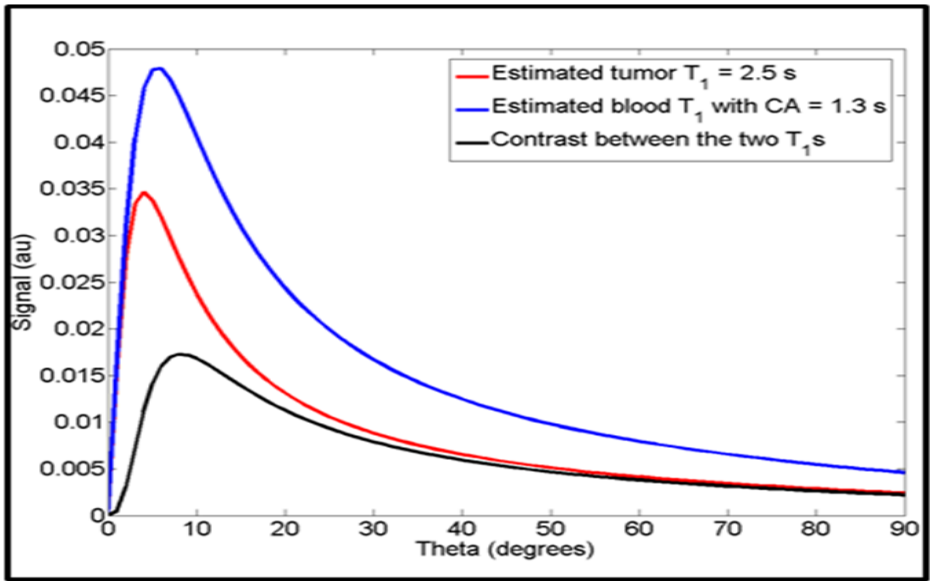

Fig. V-2. Simulation illustrating the change in signal intensity over flip angle for two tissues with different T_1 values. The blue line represents signal from blood containing CA while the red line represents signal from the tumor tissue. The black line is the difference between the two which is maximized at a flip angle = 10°.

With the flip angle optimized at 10°, the following parameters were used to image one slice containing the left ventricle and tumor tissue: TR/TE = 6/2.31 ms, NEX = 4, acquisition matrix = 64^2, and FOV = $(25\ \text{mm})^2$ with a slice thickness of 2 mm. The temporal resolution was approximately 1.5 s/image while the spatial resolution was 0.39 × 0.39 × 2 mm^3. Seventeen dummy scans were incorporated in order to ensure steady state was reached prior to the acquisition of relevant data, and spoilers were increased to 3 G/cm to ensure no transverse magnetization remained.

Localization Optimization

In order to obtain the desired slice, positioning within the animal also had to be optimized. Since the left ventricle of the heart is relatively small (approximately the size of a pencil eraser), the slice had to reflect the maximum area of the left ventricle such that minimal respiratory and cardiac motion would be reflected in the VIF measurement.

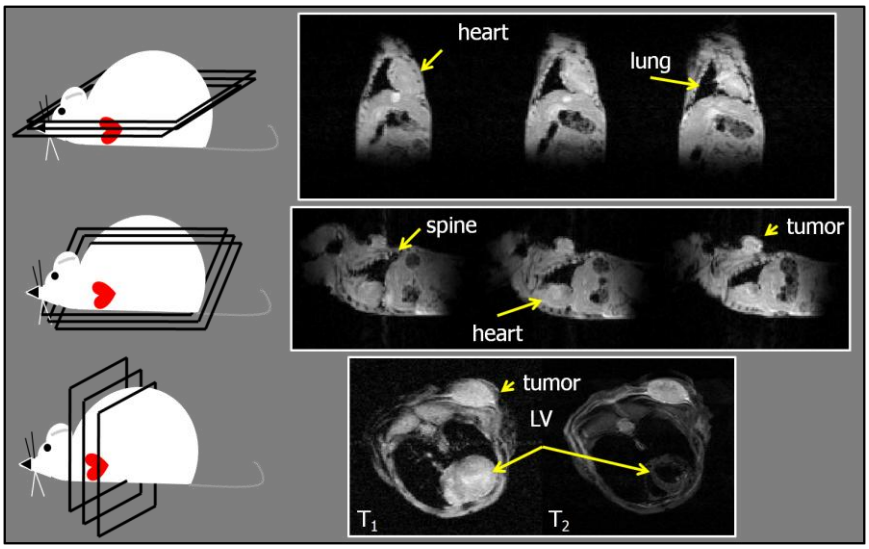

Fig. V-3. Illustration of scout images required to localize an oblique slice of the left ventricle of a mouse heart. The top row demonstrates gated coronal slices while the middle row shows gated sagittal slices. By planning from these two data sets, axial-oblique slices of the left ventricle can be obtained.

Fig. V-3 shows a series of scouts that were used to determine the ideal slice. Gated coronal and sagittal slices were gathered to plan the appropriate axial-oblique slice. If the slice is too close to the mitral valve, there is an increased likelihood of flow effects; however, if the slice is too close to the apex, myocardial wall contamination could skew the VIF measurement.

Dose Optimization

As mentioned earlier, in high concentrations, such as during the first pass of the contrast agent bolus, T_2^* effects can significantly diminish the measured MR signal, providing an inaccurate estimation of the CA concentration in the blood. Dosage was also optimized to mitigate these T_2^* effects. An example of this effect is shown in a previous Fig. IV-3. If the concentration is too high, as seen with 0.3 mmol/kg Gd-DTPA, SNR will be severely diminished but if the dose is too low, contrast to noise will not be enough to

differentiate the signal from background noise. Optimum dose for each agent was found empirically to be 0.05 mmol/kg.

T_1 Mapping Optimization

There are several techniques for obtaining T_1 information, as discussed in Chapter II (5,6). As T_1 of tissue is on the order of several seconds, measuring T_1 can become a time consuming process, particularly when multiple slices of data are acquired. In order to optimize T_1 mapping for the subsequent studies, several T_1 methods were tested using Gd-DTPA doped vials of water that have T_1 values that mimic a range a relevant biological tissue T_1, as shown in Fig V-4.

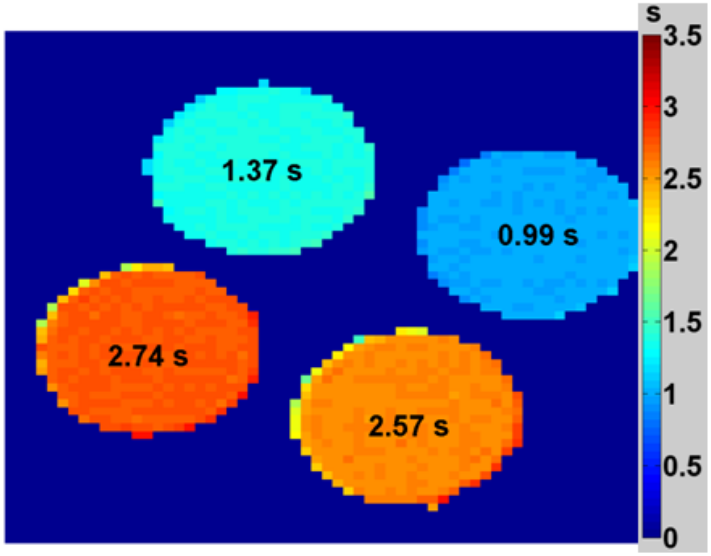

Fig. V-4. Phantom vials used for T_1 optimization;T_1 values are denoted by the text within each vial.

The methods which had the best estimation of these T_1 were experimentally examined in *vivo*. Four T_1 mapping techniques, shown in Table V-1, were compared to a single slice

(ss) inversion recovery snapshot FLASH (Fast Low Angle SHot) gradient echo sequence (for brevity, this technique will be referred to as 'snapshot') as a gold standard.

TABLE V-1
PERCENT ERROR OF COMPARED T_1 METHODS.

Method	**Scan Length (min)**	**Percent Error**			
		Vial 1 T_1 **= 0.99 min**	**Vial 2** T_1 **= 1.37 min**	**Vial 3** T_1 **= 2.57 min**	**Vial 4** T_1 **= 2.74 min**
snapshot (ss) 17 TIs	**68**	0	0	0	0
variable FA (ms) 5 α with no $\mathbf{B_1}$	**4.5**	31.45	43.527	35.167	37.851
variable FA (ms) 5 α with $\mathbf{B_1}$	**40.7**	61.496	59.6	>50	>50
FSEMS -IR (ms) 18 TIs	**144**	2.948	3.177	4.241	5.394
FSEMS -IR (ms) 7 TIs	**56**	0.456	0.168	0.008	1.525
SEMS -SR (ms) 7 TRs	**42**	25.774	34.361	20.981	36.607
FSEMS -SR (ms) 7 TRs	**12**	9.583	20.295	9.242	8.933

The snapshot sequence is a T_1 mapping method that uses a non-selective adiabatic pulse which allows it to be more robust to $\boldsymbol{B}_1$ and $\boldsymbol{B}_0$ inhomogeneities that may skew T_1 measurements. For each inversion pulse, eight lines of *k*-space were acquired, making it faster than a typical inversion recovery experiment. During the data fit, S_0 was also a free parameter in order to account for incomplete longitudinal inversions. All compared

techniques were acquired at multiple slices as future studies would require this covering the entire tumor volume.

The variable FA (flip angle) technique varies the flip angle, α, as shown in the gradient echo equation (Eqn. (II-9)), over a range from 10°-50° with a fixed *TR* and *TE*; the signal at five angles (10°, 20°, 30°, 40° , and 50°) were measured and the data was then fit to Eqn. (II-9) to obtain T_1. Since this technique relies heavily on the homogeneity of $\boldsymbol{B}_1$, $\boldsymbol{B}_1$ maps were collected to correct for heterogeneities as well (7). Data from a spin echo sequence (SEMS-SR) with seven *TR*s (200, 500, 800, 1000, 1300, 2000, and 4000 ms) were also acquired and fit to Eqn. (II-8). In order to achieve the lowest scan time possible, fast spin echo inversion recovery (FSEMS-IR) and fast spin echo saturation recovery (FSEMS-SR) were incorporated into the comparison. Similar to snapshot, FSEMS experiments acquired multiple lines of *k*-space at a time in order to reduce acquisition time. FSEMS-IR administers a full inversion pulse and the signal was sampled at multiple inversion times (*TI*), as described in a previous chapter. FSEMS-SR varied the *TR* with a fixed *TE* and was fit to Eqn. (II-8) to obtain T_1 estimations.

The method, total imaging time, and percent error for each vial tested are recorded in Table V-1. For the subsequent studies, a T_1 mapping technique that took less than 60 minutes was desired to minimize total *in vivo* imaging time. While variable FA methods are relatively fast, they can be very inaccurate at high field strengths due to inhomogeneities in the applied $\boldsymbol{B}_1$ field. FSEMS-IR seems to very accurate with an error (when compared to snapshot) less than 2%, but it takes 56 minutes to obtain this data. FSEMS-SR, at a 12 minute total imaging time was selected for a subsequent *in vitro* study; the results of this study are shown in Table V-2.

TABLE V-2
FURTHER *IN VITRO* EXPERIMENTS WITH POTENTIAL T_1 ESTIMATION METHODS.

Method	Scan Length (min)	Percent Error			
		Vial 1 T_1 = 0.99 min	Vial 2 T_1 = 1.37 min	Vial 3 T_1 = 2.57 min	Vial 4 T_1 = 2.74 min
FSEMS -SR (ms) 9 TRs (NEX = 8)	24.53	2.596	1.7	0.112	1.044
FSEMS -SR (ms) 9 TRs (NEX = 6)	16.35	2.524	0.942	0.064	0.86
FSEMS -SR (ms) 9 TRs (NEX = 4)	12.27	1.95	1.905	0.288	0.575
FSEMS -SR (ms) 7 TRs (NEX = 8)	22.19	2.692	1.604	0.078	1.132
FSEMS -SR (ms) 6 TRs (NEX = 8)	20.48	2.678	1.629	0.016	0.887
FSEMS -SR (ms) 7 TRs (NEX = 6)	16.64	2.557	0.998	0.056	0.896
FSEMS -SR (ms) 7 TRs (NEX = 4)	11.09	2.034	1.883	0.266	0.696
FSEMS -SR (ms) 6 TRs (NEX = 4)	10.24	1.986	1.843	0.399	0.467

Several FSEMS-SR protocols were tested and compared to the same phantom vials, using single slice (SS) snapshot as a gold standard. The number of TRs and NEXs were varied to obtain an accurate and fast T_1 estimation. From this experiment, the highlighted protocols had less than a 2% error in multi-slice data and were tested in *vivo*. However, upon testing FSEMS-SR protocols *in vivo*, a gross overestimation of T_1 values were found in both phantom and mouse muscle tissue, as shown in Fig. V-3. Water phantom T_1

values exceeded five seconds when spectroscopic results of water at 9.4T range from 3.4 to 3.6 seconds, as similarly indicated by the snapshot data. This dramatic differences could be due to known magnetic transfer (MT) effects from off-resonance saturation seen in FSEMS protocols (8).

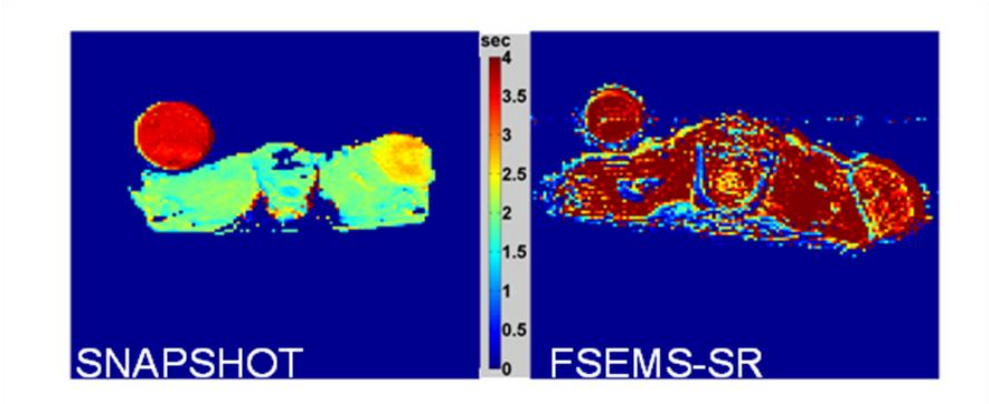

Fig. V-5. *In vivo* experiment between snapshot and FSEMS-SR reflecting a large overestimation in T_1 measurements with FSEMS-SR.

To circumvent these issues, single slice snapshot was adapted to a multi-slice snapshot sequence, and testing showed less than a 5% difference in T_1 from the single slice snapshot protocol. For multi-slice snapshot, eight inversion times and a NEX = 4 can estimate T_1 values accurately with a total imaging time of 52 minutes. Once all of these optimizations were completed, individual VIFs were acquired and compared to a population-derived VIF described in the following chapter.

References

1. Tofts PS, Berkowitz B, Schnall MD. Quantitative analysis of dynamic Gd-DTPA enhancement in breast tumors using a permeability model. Magn Reson Med 1995;33(4):564-568.
2. Pickup S, Zhou R, Glickson J. MRI estimation of the arterial input function in mice. Acad Radiol 2003;10(9):963-968.
3. Port RE, Knopp MV, Brix G. Dynamic contrast-enhanced MRI using Gd-DTPA: interindividual variability of the arterial input function and consequences for the assessment of kinetics in tumors. Magn Reson Med 2001;45(6):1030-1038.
4. Parker GJ, Roberts C, Macdonald A, Buonaccorsi GA, Cheung S, Buckley DL, Jackson A, Watson Y, Davies K, Jayson GC. Experimentally-derived functional form for a population-averaged high-temporal-resolution arterial input function for dynamic contrast-enhanced MRI. Magn Reson Med 2006;56(5):993-1000.
5. Kingsley P. Methods of measuring spin-lattice (T-1) relaxation times: An annotated bibliography. CONCEPT MAGNETIC RES 1999;11(4):243-276.
6. Haacke M, Brown R, Thompson M, Venkatesan R, Haacke M, Brown R, Thompson M, Venkatesan R. Magnetic Resonance Imaging: Physical Principles and Sequence Design: Wiley-Liss; 1999.
7. Yarnykh VL. Actual flip-angle imaging in the pulsed steady state: a method for rapid three-dimensional mapping of the transmitted radiofrequency field. Magn Reson Med 2007;57(1):192-200.
8. Constable RT, Anderson AW, Zhong J, Gore JC. Factors influencing contrast in fast spin-echo MR imaging. Magn Reson Imaging 1992;10(4):497-511.

CHAPTER VI

A QUANTITATIVE COMPARISON OF THE INFLUENCE OF INDIVIDUAL- VERSUS POPULATION-DERIVED VASCULAR INPUT FUNCTIONS ON DCE-MRI IN SMALL ANIMALS

Introduction

Currently, there are few studies that discuss the relative merits and accuracy of using the population VIF versus an individual VIF in small animals (1,2). Pickup, *et al.*, obtained the VIF from the left ventricle of the imaging data in four mice. Temporal resolution for this study was approximately one image/s, but spatial resolution was severely restricted using only 16 phase-encode lines over a 2.5 cm field of view. Additionally, the injection was manually performed (1). More recently, another study by McGrath *et al*., compared the VIF in rats (using a manual injection) with frequently used VIF models and the population averaged VIF and reported the downstream effects on pharmacokinetic modeling parameters (2).

The goal of this study is to assess the error in parameters extracted from DCE-MRI modeling of tumor tissue when using a VIF derived from a population average versus those extracted with an individually measured VIF in mice. These VIF measurements were obtained in a cohort of mice using two different contrast agents of varying molecular weight. The comparisons between pharmacokinetic parameters were performed on both an ROI and voxel-based analyses. Voxel analysis allows characterization of tumor heterogeneity while the ROI-analysis may be more typically used in a treatment response study. Additionally, performing voxel analysis allows for

performing intra-animal comparisons that are not possible when just an ROI value is computed. Error and agreement between these methods are reported, and the subsequent power analysis and consequences for using either individual or population VIF in DCE-MRI is discussed.

Methods

Tumor Model

Murine 4T1 breast cancer cells were cultured in Dulbecco's modified Eagle's medium supplemented with 10% fetal bovine serum and 0.2% Gentamicin. Cells were incubated at 37^{o} C in a mixture of 5%/95% CO_2/air. Cells growing at 80% confluence were harvested, and a single cell suspension containing 5×10^6 cells suspended in 100 μL of medium was injected subcutaneously near the shoulder. Tumors were allowed to grow for six to nine days before imaging; tumor size ranged from 100 mm^3 to 400 mm^3 thereby producing a range of kinetic parameters.

Animal Model

Eleven female Balb/c mice (approximately 20 g, 8-10 weeks of age) were purchased from Charles River Laboratories (Wilmington, MA), housed in pathogen-free facilities and provided with rodent chow and tap water *ad libitum*. A 26-gauge jugular catheter was surgically implanted to allow for delivery of the contrast agent. All animals were imaged twice: once using an injection of 120 μL of 0.05 mmol/kg gadopentetate dimeglumine, Gd-DTPA, (Magnevist, Wayne, NJ) (3) and once using an injection of 120 μL of 0.05 mmol/kg P846 (Guerbet Research, Aulnay-sous-Bois, France) on a later day (4). During

all imaging procedures, the mice were anesthetized using a 2%/98% isoflurane/oxygen mixture. Temperature, respiratory rate, and electrocardiogram (ECG) signal were monitored throughout the entire experiment. All procedures in the experiment were reviewed and approved by our Institutional Animal Care and Use Committee.

MRI Contrast Agents

The two contrast agents used here were described in greater detail in Chapter II. Briefly, Gd-DTPA (3) and P846 (4-6) were used in this experiment. Relaxivities for Gd-DTPA and P846 at 7T were found using the technique described in chapter V; the measured values of 4.71 $s^{-1}mM^{-1}$ and 10.62 $s^{-1}mM^{-1}$, respectively were used in subsequent data analyses.

Data Acquisition

MR imaging was performed using a Varian 7.0T Inova scanner equipped with a 25 mm quadrature volume coil (both Varian, Inc. Palo Alto, CA). A respiratory- and ECG-gated gradient echo sequence was used to locate a 2 mm slice that both contained the tumor and cut across the short-axis of the left ventricle (LV) of the heart. Data for constructing a pre-contrast T_1 map were obtained by an inversion recovery snapshot FLASH (Fast Low Angle SHot) gradient echo sequence with an adiabatic inversion pulse over nine inversion times (TI) ranging logarithmically from 200 – 6000 ms with *TR**TE* \α= 10000 ms\ 3.44 ms\15° and NEX = 4, FOV = 25 mm^2, and matrix = 64^2 (7-9). The data were then fit to Eqn. (II-10).

The DCE-MRI protocol employed a T_1-weighted, spoiled gradient echo sequence to obtain serial images at a temporal resolution of 1.536 seconds for 20 minutes with $TR\backslash TE\backslash\alpha$ = 6 ms\2.41 ms\10^o, NEX = 4, and the same acquisition matrix and FOV as for the T_1 map. A 120 µL bolus of 0.05 mmol/kg Gd-DTPA or P846 was delivered *via* a jugular catheter using an automated syringe pump (Harvard Apparatus, Holliston, MA, USA) at a rate of 2.4 mL/min after 100 baseline images were acquired.

Data Analysis

Data collected for the T_1 map were fit using a nonlinear least squares method in Matlab 2008a (The Mathworks, Natick, MA, USA) to Eqn. (II-10). Once pre-contrast T_1 maps were calculated for the interrogated slice, regions of interest were drawn to include the entire left ventricle of the mouse. Each voxel was then converted to an R_1 (= $1/T_1$) time course by the method of Landis, *et al.* (10)

$$R_1(t) = -\frac{1}{TR}\cdot ln\left[\frac{(S_0\cdot sin\alpha\cdot e^{-TE/T_2^*}) - S(t)\cdot cos\alpha}{S_0\cdot sin\alpha\cdot e^{-TE/T_2^*} - S(t)}\right], \qquad \text{(VI-1)}$$

where R_1, TR, TE, T_2^* and α are described previously, $S(t)$ is the signal intensity time course, and

$$S_0 = S_{ss}\cdot\frac{(1-e^{-TR/T_1}\cdot cos\,\alpha)}{(1-e^{-TR/T_1})\cdot sin\alpha\cdot e^{-TE/T_2^*}}, \qquad \text{(IV-2)}$$

where S_{ss} is the steady state averaged signal intensity before contrast agent administration (pre-CA). At a short TE, T_2^* contribution to the signal was assumed to be neglible. Using the R_1 time course for the LV, the concentration of contrast agent in the plasma, C_p, was then determined using the fast exchange limit (FXL) assumption

$$R_1 = r_1 \cdot (1 - hct) \cdot C_p + R_{10}\,, \qquad \text{(IV-3)}$$

where r_1 is the relaxivity for Gd-DTPA and P846, (values reported in Chapter V), *hct* is the hematocrit of a mouse (h = 0.45 was used in this study based on literature values (11)) and R_{10} is the pre-contrast R_1 value.

Due to potential flow and motion artifacts, a simple filter was employed to examine every voxel within the LV blood pool for specific characteristics; in particular, voxels were included in the VIF calculation if the SNR ≥ 30 at all time points and if the peak concentration was ≥ 0.15 mM, based on literature values (1). Each voxel returned was also visually inspected for appropriate wash-out activity to prevent potential myocardial wall contamination. An ROI in the left ventricle was drawn and all voxel time courses were graphically displayed. If the time course had an elongated wash-out indicative of slower clearance (characteristic of tissue curves), it was excluded from analysis (typically only 2-3 voxels per animal). These appropriate voxels were then averaged together to represent the individual VIF for that animal. Once the individual VIFs were collected (N = 11 for Gd-DTPA and N = 9 for P846), they were aligned to the same initial uptake time. Briefly, the peaks (maximum value) of the individual VIFs were used to align the data to form the population VIF. Alignment typically varied 1-3 time points and interpolation (if needed) was either added to the baseline acquisition or at the tail end of the wash-out period. For each animal, an individual VIF (VIF_{ind}) and a population VIF (VIF_{pop}), which was determined by taking the mean of the individual VIFs (excluding its own individual VIF), were used to fit that animal's ROI signal curves to both the standard and extended model represented in Eqs. Eqn. (IV-2) and Eqn. (IV-3) to extract K^{trans}, v_e, and v_p.

Statistical Analysis

By fitting the tissue signals to the standard (*ST*) and extended (*EX*) models with both VIF_{ind} and VIF_{pop}, two sets of five parameters were produced: 1) using VIF_{ind} to obtain $K^{trans,ind}$ (*ST*), $v_{e,ind}$ (*ST*), $K^{trans,ind}$ (*EX*), $v_{e,ind}$ (*EX*), *and* $v_{p,ind}$ (*EX*); and 2) using VIF_{pop}:to obtain $K^{trans,pop}$ (*ST*), $v_{e,pop}$ (*ST*), $K^{trans,pop}$ (*EX*), $v_{e,pop}$ (*EX*), *and* $v_{p,pop}$ (*EX*). Each parameter was paired for comparison (e.g., $K^{trans,ind}$ (*ST*) and $K^{trans,pop}$ (*ST*)); these "parametric pairs" were compared on two levels.

First, an ROI was drawn around the tumor for each animal. The signal from the ROI was averaged to produce one R_1 time course, which was then analyzed by both the standard and extended models. The absolute agreements between the resulting parametric pairs were then assessed using the concordance correlation coefficient (CCC) (12). Specifically, the CCC evaluates the degree to which these pairs fall on the line of unity when they are plotted against each other. Like the more common Pearson correlation coefficient, a perfect correlation of the pairs produce a CCC value of 1, while completely independent pairs produce a CCC equal to 0. The Pearson correlation coefficient, was also calculated. In addition to the correlation indices, each parametric pair was analyzed using linear regression. We also performed a power analysis on each set of parameters to determine how many more samples are likely needed to detect 50% increase/decrease in the means with 80% power if the population VIF was used. This calculation is based on a two sample t-test. To account for the variability of the estimated standard deviation, we used a bootstrap sampling technique and reported the median sample sizes.

The second level of comparison was based on individual voxel data for each animal. Voxels within the whole tumor ROIs were fit individually to produce two sets of five parametric maps for all animals (as described above). To ensure that only properly fit data continued on for further comparison, voxel fits were filtered using a simple r^2 filter ($r^2 > 0.6$) for the VIF_{ind} data; additionally voxel data were filtered to ensure the resulting parameters fell within a physiologically relevant parametric range ($0 < K^{trans} < 1$ min^{-1}, $0 < v_e < 1$, and $0 < v_p < 1$). Voxels that could be fit using the VIF_{ind} but not the VIF_{pop} were tabulated and reported in Table VI-7. For each animal, the CCC and Pearson correlation coefficient were determined on a voxel by voxel basis between the parametric pairs described previously; additionally these paired data were compared using linear regression.

Modeling and Temporal Resolution Analysis

Both raw VIF_{ind} and VIF_{pop} data were fit to a bi-exponential decay model (13). Kinetic parameters produced using the fitted VIF_{ind} and fitted VIF_{pop} data were compared using statistics similar to those described above in order to assess the accuracy of using a fitted VIF_{pop} versus using a fitted VIF_{ind}. Additionally, ROI signal data were downsampled by selecting every 20th point (simulating a temporal resolution of approximately 30 seconds) in order to simulate a realistic clinical acquisition with a reduced temporal resolution. Data were then interpolated using a linear interpolation scheme in Matlab (the 'interp1' function) and fit to extract kinetic parameters using the VIF_{ind} and VIF_{pop} as an input to the model. Kinetic parameters were compared with similar statistics as described above.

Results

Using a standard injection protocol, the resulting population averaged VIF for both Gd-DTPA (n=11) and P846 (n=9) are presented in Fig. VI-1 (a) and (b) (black line); the grey lines represent one standard deviation from each population VIF. Fig. VI-1 (c) illustrates two VIF_{ind} from two separate mice using Gd-DTPA (blue dashed and red lines) compared to the VIF_{pop} (black solid line).

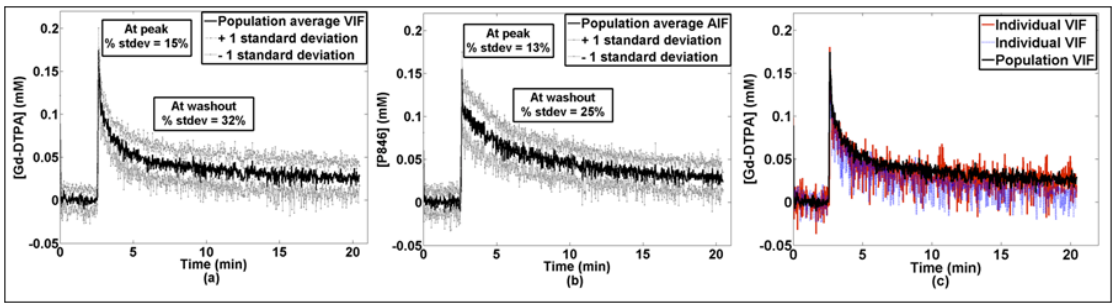

Fig.VI-1. Population derived VIFs using Gd-DTPA (N = 11) (a) and P846 (N = 9) (b). P846 had a longer wash-out period than Gd-DTPA due to its larger size. Both Gd-DTPA and P846 have a relatively small standard deviation at the peak (13% and 15%, respectively). However, both have a larger standard deviation at ~5-10 minutes during wash-out equal to 32% and 25%, respectively. Panel **(c)** illustrates two example VIF_{ind} (blue dashed and red solid lines) compared to the VIF_{pop} (solid black line).

Note that while the red VIF_{ind} seems to fall along the VIF_{pop}, the VIF_{ind} indicated by the blue dashed line has a slightly different wash-out period. Since P846 is a larger contrast agent, the P846 VIF has a longer wash-out period than those obtained using Gd-DTPA. The peak values for both agents were very similar across all subjects, yielding a standard deviation of approximately 15% while the wash-out was different for both Gd-DTPA and P846 with a standard deviation of 32% and 25%, respectively.

ROI Analysis

The first set of analyses examined the ROI averaged signal time course from the tumor of each mouse. Each averaged time course was then fit to Eqn. (IV-2) and Eqn. (IV-3) to extract the pharmacokinetic parameters. By modeling each time-intensity course using both the VIF_{ind} and VIF_{pop}, two sets of five parameters ($K^{trans}(ST)$, $v_e(ST)$, $K^{trans}(EX)$, $v_e(EX)$, *and* $v_p(EX)$) were produced and the subsequent parametric pairs (i.e., $K^{trans,ind}(ST)$ and $K^{trans,pop}(ST)$) were compared. Fig. VI-2 shows the results of this study for Gd-DTPA (a) and P846 (b).

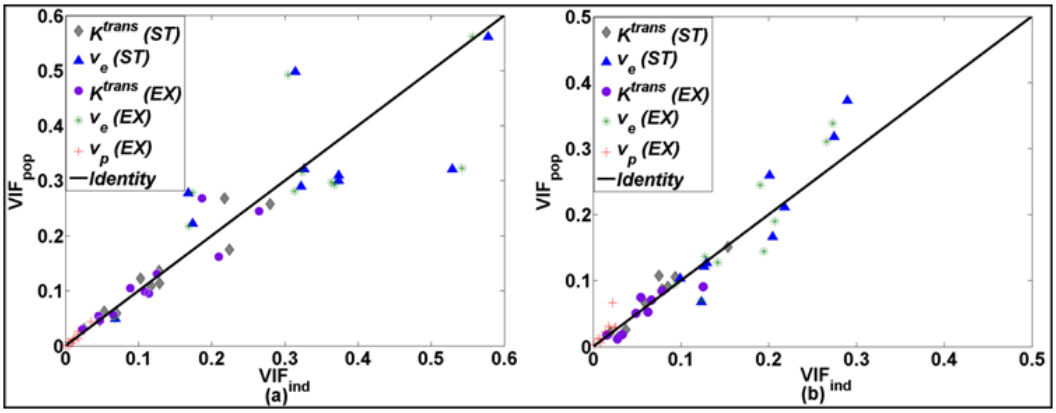

Fig.VI-2 Parametric plots for both Gd-DTPA (a) and P846 (b) resulting from the ROI analysis. Each parameter is designated by the colored marker (for each animal) while the solid black line indicates the line of identity.

Upon visual inspection, these parameters appear to fall close to the line of identity for both agents; also in both agents, the parametric pairs for $v_e(ST)$ and $v_e(EX)$ tend to deviate from unity more than $K^{trans}(ST)$, $K^{trans}(EX)$, and $v_p(EX)$. The CCC, reported in Table VI-1, represents a quantitative measure of parameter proximity to the line of unity.

TABLE VI-1
RESULTS FROM THE ROI-BASED COMPARISON.

	CCC (95% CI)		Pearson		Intercept		Slope	
	Gd-DTPA	**P846**	**Gd-DTPA**	**P846**	**Gd-DTPA**	**P846**	**Gd-DTPA**	**P846**
K^{trans} (ST)	**0.93** (0.81,0.98)	**0.93** (0.73,0.98)	0.95	0.95	-0.02	0.00	1.20	1.10
v_e (ST)	**0.82** (0.48,0.95)	**0.84** (0.62,0.94)	0.83	0.94	0.08	-0.08	0.74	1.48
K^{trans} (EX)	**0.96** (0.85,0.99)	**0.85** (0.47,0.96)	0.96	0.85	-0.01	0.01	1.06	0.82
v_e (EX)	**0.80** (0.42,0.94)	**0.82** (0.58,0.93)	0.81	0.92	0.09	-0.07	0.69	1.45
v_p (EX)	**0.88** (0.76,0.97)	**0.45** (0.02,0.74)	0.98	0.73	0.00	0.00	1.54	1.61

TABLE VI-2
POPULATION CHANGES RESULTING FROM THE ROI-BASED COMPARISON.

	Δ% in Population Size	
	Gd-DTPA	**P846**
K^{trans} (ST)	**35**	**19**
v_e (ST)	**-14**	**100**
K^{trans} (EX)	**16**	**11**
v_e (EX)	**-16**	**100**
v_p (EX)	**58**	**57**

The CCC values for K^{trans} (both *ST* and *EX*) are > 0.90 for Gd-DTPA and > 0.85 for P846 indicating a strong correlation between the pairs. However, the CCC values for v_e (both *ST* and *EX*) are lower for both contrast agents (0.79 to 0.83 for Gd-DTPA and P846, respectively). Interestingly, while both the CCC for K^{trans} and v_e were similar between the contrast agents, v_p (*EX*) was very different. The v_p (*EX*) values estimated using Gd-DTPA had a stronger correlation than the P846 data. In addition to the CCC, the Pearson correlation coefficients show a strong significant linear relationship between each paired

set of parameters (ranging from 0.80 to 0.97). The results of the linear regression analysis agrees with the interpretation of the CCC in that K^{trans} (both *ST* and *EX*) have slopes close to 1.0 while v_e and v_p deviate from 1.0 by 30-40%.

Table VI-2 conveys the change in the number of animals required to achieve the same power when using the VIF_{pop} versus the VIF_{ind}. Relatively small increases in the number of animals are required for K^{trans} (*ST*) and K^{trans} (*EX*) using Gd-DTPA (35% and 19%, respectively), K^{trans} (*ST*) and K^{trans} (*EX*) using P846 (11% and 16%, respectively). A smaller number of animals is required for v_e measurements using Gd-DTPA (-14% for v_e (*ST*) and -16% for v_e (*EX*)) but require double the sample size using P846 (100% for both v_e (*ST*) and v_e (*EX*)). To achieve the same power for v_p measurements, the sample size must be increased by half the number of initial subjects (58% and 57% for Gd-DTPA and P846, respectively).

Voxel Analysis

As described above, voxels for each animal were fit to Eqn. (IV-2) and Eqn. (IV-3) to yield paired parametric maps using both the VIF_{ind} and VIF_{pop}. An example mouse is shown in Fig. VI-3.

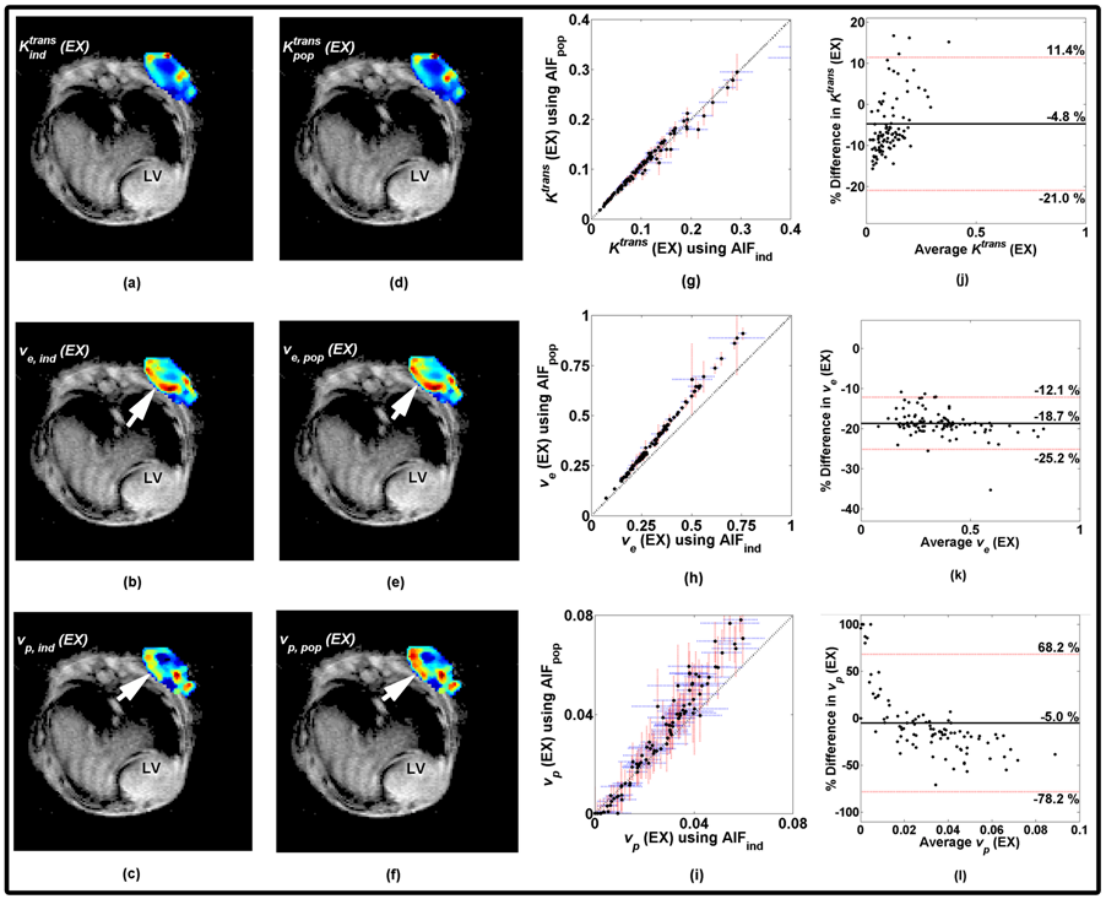

Fig.VI-3. Parametric maps determined using Eqn. (IV-3) overlaid on a (gated) T_1-weighted anatomical image for one mouse. Panels a-c depict the parametric maps using the VIF_{ind} while d-f show the maps resulting from using the VIF_{pop}. Each parameter for each voxel is plotted with respect to its pair in g-i where the solid black line indicates the line of unity. Each data point has a set of dotted vertical red and horizontal blue lines that represent the 95% CI for the respective axes. A Bland-Altman plot is presented in j-l for each parameter. The *x*-axis represents the average parametric value between those obtained using the VIF_{ind} and VIF_{pop} while the y-axis is the percent difference between VIF_{ind} and VIF_{pop} parametric estimations with respect to the VIF_{ind} parameter. The solid black line is the mean difference while the dotted red lines represent ± 2*standard deviation. The maps are very similar, particularly for K^{trans}. However, overestimations in v_e and v_p are evident using the VIF_{pop} versus the VIF_{ind}. The arrows in panels b and e emphasize the areas within the maps where v_e found using VIF_{pop} is overestimated relative to v_e found using VIF_{ind}. In panels c and f, the overestimations are also noted for the v_p parameter as well.

Panels (a) - (c) demonstrate the parametric maps from the extended model overlaid on a (gated) T_1-weighted anatomical image obtained using the VIF_{ind} during modeling, while panels (d) - (f) depict parametric maps obtained using the VIF_{pop}. When

plotted against each other, as in panels (g) – (i) the voxel level data are linearly related (black line represents unity). Panels (j) – (l) illustrate Bland-Altman plots for each kinetic parameter with the x-axis representing the average parametric value between those obtained using the VIF_{ind} and VIF_{pop} while the y-axis is the percent difference between VIF_{ind} and VIF_{pop} parametric estimations with respect to the VIF_{ind} parameter. The solid black line is the mean difference while the dotted red lines represent ± 2×standard deviation. The slopes of the fit lines for K^{trans} pairs for the subject shown in Fig. VI-3 differ from unity by 5-7% while the slopes of the fit lines for v_e and v_p deviate from the identity line by as much as 24-31%. Upon closer inspection of the maps of this particular mouse, the overestimation of v_e and v_p by the VIF_{pop} (panels (e) and (f)) compared to their respective pairs (b and c) are shown by the arrows in panels (b), (c), (e), and (f). The differences between these estimations are quantified in panels (j) – (l). For this animal, confidence intervals (CI), shown as the vertical red and horizontal blue dotted lines for K^{trans} are very tight (g) while CI boundaries for v_e tend to be tighter for lower values and increase as the value of v_e increases (h). CI values for v_p are quite large but are similar for both the VIF_{ind} and VIF_{pop} (i).

The CCC was computed for each animal for each parameter and results are presented in Fig. VI-4. Panels (a) **–** (e) in Fig. VI-4 display the plots of the CCC (*x* axis) for each animal (*y* axis) with the solid lines showing the 95% CI boundaries for each value while the number on the far right is the nominal CCC.

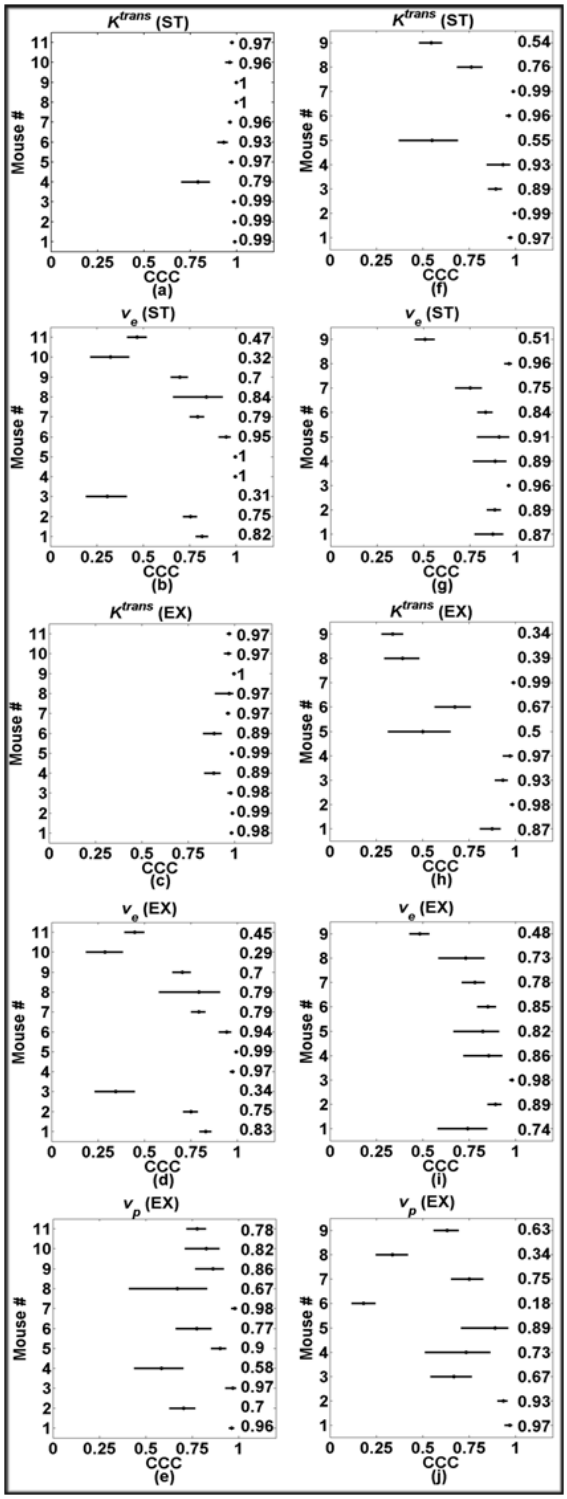

Fig.VI-4. Panels a-e show the CCC plots for the respective kinetic parameter in the voxel based analysis found using Gd-DTPA; the P846 data is shown in panels f-j. Each plot displays the CCC values (*y*-axis) and 95% CI for voxels obtained from each animal (*x*-axis). The CCC values are listed in the column on the right side of the plot.

While the voxel-based analysis echoes the results of the ROI-based analysis, the difference between the parameter pairs is magnified for some animals. K^{trans} (both *ST* and *EX*) still reflects very high correlation with unity (panels (a) and (c)) with the exception of one mouse in the *ST* analysis and two mice in the *EX* analysis that used Gd-DTPA, that yielded a CCC > 0.90. For P846, seven mice had CCC > 0.75 for K^{trans} (*ST*) (panel (f)). K^{trans} correlation for P846 is reduced in the extended model, yielding only five mice with CCC > 0.85. Three mice using Gd-DTPA had CCC < 0.70 for v_e (both *ST* and *EX*), (panels (b) and (d)). For mice that were imaged using P846, eight had CCC > 0.70 for v_e (panels (g) and (i)); again, modeling with the standard model provided higher correlations than the extended model for P846 data. Additionally, v_p had nine mice with CCCs higher than 0.75 for Gd-DTPA data while only four had CCC > 0.75 using P846. Additional quantitative results from the voxel-by-voxel study are shown in Tables VI 3-6.

TABLE VI-3
VOXEL-BASED RESULTS FOR GD-DTPA DATA USING *ST* MODEL.

Mouse	Pearson Corr. Coefficient		Slope		Intercept	
	K^{trans} (ST)	v_e (ST)	K^{trans} (ST)	v_e (ST)	K^{trans} (ST)	v_e (ST)
1	1.000	0.992	0.927	0.796	-0.006	0.005
2	0.999	0.996	1.090	1.340	0.010	0.005
3	0.998	0.882	0.983	0.457	-0.011	0.084
4	0.998	0.998	1.441	1.011	-0.031	0.017
5	0.999	1.000	1.144	0.957	-0.008	0.008
6	0.999	0.981	0.826	0.975	-0.011	0.023
7	1.000	1.000	0.921	0.836	-0.002	0.008
8	0.999	1.000	1.011	0.695	-0.004	0.001
9	0.999	0.989	0.998	0.829	-0.011	0.033
10	0.998	0.888	1.146	1.631	0.007	0.081
11	0.993	0.975	1.047	1.565	0.011	0.037

Tables VI-3 and VI-4 show the Pearson correlation coefficient and linear regression results for Gd-DTPA for the standard and extended models, respectively. Tables VI-5 and VI-6 present results for P846 using the standard and extended models, respectively.

TABLE VI-4
VOXEL-BASED RESULTS FOR GD-DTPA DATA USING *EX* MODEL.

Mouse	Pearson Corr. Coefficient			Slope			Intercept		
	K^{trans} (EX)	v_e (EX)	v_p (EX)	K^{trans} (EX)	v_e (EX)	v_p (EX)	K^{trans} (EX)	v_e (EX)	v_p (EX)
1	0.998	0.993	0.978	0.922	0.793	1.129	-0.010	0.004	0.001
2	0.991	0.992	0.888	0.968	1.319	1.638	0.021	0.001	0.001
3	0.997	0.924	0.976	0.909	0.488	0.957	-0.003	0.065	0.002
4	0.998	0.998	0.949	1.248	0.939	1.725	-0.001	0.004	0.008
5	0.997	1.000	0.991	1.072	0.956	1.371	-0.003	0.005	0.001
6	0.986	0.980	0.868	0.784	0.958	1.401	-0.006	0.018	0.003
7	1.000	0.999	0.990	0.921	0.833	0.979	-0.002	0.009	0.002
8	0.987	0.999	0.999	0.890	0.647	2.186	-0.001	0.006	0.000
9	0.998	0.987	0.881	1.027	0.826	0.953	-0.015	0.029	0.003
10	0.995	0.863	0.957	1.096	1.609	1.454	0.009	0.106	0.002
11	0.989	0.973	0.965	1.005	1.613	1.725	0.014	0.027	0.003

The Pearson correlation coefficients reflect a high degree of linearity between parameter pairs in both Gd-DTPA and P846 data.

TABLE VI-5
VOXEL-BASED RESULTS FOR P846 DATA USING *ST* MODEL.

Mouse	Pearson Corr. Coefficient		Slope		Intercept	
	K^{trans} (ST)	v_e (ST)	K^{trans} (ST)	v_e (ST)	K^{trans} (ST)	v_e (ST)
1	1.000	0.922	1.211	0.745	-0.002	1.211
2	0.997	0.996	0.951	1.244	0.009	0.951
3	0.999	1.000	1.232	1.038	-0.005	1.232
4	0.998	0.999	1.327	0.750	-0.018	1.327
5	0.998	0.972	1.865	0.770	-0.024	1.865
6	0.990	0.999	0.811	1.309	0.025	0.811
7	1.000	0.987	1.091	1.356	0.006	1.091
8	0.997	0.964	0.597	0.903	0.005	0.597
9	1.000	0.996	0.451	0.528	0.001	0.451

For Gd-DTPA data, the slopes for K^{trans} are close to 1.0 while v_e and v_p tend to deviate, thus indicating a lower correlation with unity.

TABLE VI-6
VOXEL-BASED RESULTS FOR P846 DATA USING *EX* MODEL.

Mouse	Pearson Corr. Coefficient			Slope			Intercept		
	K^{trans} (EX)	v_e (EX)	v_p (EX)	K^{trans} (EX)	v_e (EX)	v_p (EX)	K^{trans} (EX)	v_e (EX)	v_p (EX)
1	0.982	0.846	0.987	1.469	0.597	0.869	-0.005	0.058	0.001
2	0.989	0.997	0.983	0.925	1.251	1.313	0.010	0.013	0.004
3	0.995	0.994	0.983	1.301	1.010	1.735	-0.011	0.002	0.002
4	0.993	0.998	0.989	1.217	0.734	1.612	-0.023	0.004	0.003
5	0.993	0.976	0.921	2.056	0.695	0.918	-0.029	0.047	0.004
6	0.904	0.975	0.789	0.484	1.214	3.318	0.037	0.032	0.008
7	0.993	0.993	0.990	1.028	1.328	1.784	0.007	0.006	0.002
8	0.935	0.739	0.940	0.343	0.828	2.824	0.013	0.069	0.005
9	0.960	0.986	0.935	0.301	0.517	1.824	0.007	0.002	0.002

Comparing the two contrast agents, it appears that while both show high degrees of linearity, the average difference between the slopes of the fit line for K^{trans} data and the line of unity is greater for P846 relative to Gd-DTPA. Both Gd-DTPA and P846 data yield similar differences for v_e, while v_p has a much higher average difference between fit

and unity lines. For both agents, the slope/intercept data reiterate the CCC findings seen in Fig. VI-4.

Modeling and Temporal Resolution Analysis

Upon fitting both the VIF_{ind} and VIF_{pop}, absolute kinetic parameter values changed with respect to that of the raw data analysis, as shown in Table VI-7 for Gd-DTPA data; however, no significant difference was found in the statistical comparison between these absolute values produced.

TABLE VI-7
ABSOLUTE PARAMETER VALUES PRODUCED FROM RAW AND FIT VIF DATA.

Mouse	K^{trans} (ST) (min^{-1}) from VIF_{ind}		v_e (ST) from VIF_{ind}	
	raw	fit	raw	fit
1	0.128	0.131	0.374	0.373
2	0.053	0.055	0.174	0.172
3	0.064	0.065	0.483	0.468
4	0.293	0.224	0.668	0.574
5	0.128	0.128	0.326	0.327
6	0.224	0.224	0.322	0.325
7	0.280	0.286	0.745	0.740
8	0.047	0.046	0.068	0.069
9	0.117	0.122	0.374	0.369
10	0.102	0.104	0.314	0.313
11	0.025	0.026	0.168	0.165
p-value	**0.904**		**0.897**	

Additionally, comparing the parameters using the fitted VIF_{ind} and the fitted VIF_{pop} shared similar statistics to comparing values produced using the raw VIF_{ind} and the raw VIF_{pop} data, as indicated in Table VI-8.

TABLE VI-8
STATISTICAL COMPARISON PARAMETERS PRODUCED BY RAW AND FIT VIF .

	Pearson		Intercept		Slope		CCC	
	Gd-DTPA (raw)	Gd-DTPA (fit)	Gd-DTPA (raw)	Gd-DTPA (fit)	Gd-DTPA (raw)	Gd-DTPA (fit)	Gd-DTPA (raw)	Gd-DTPA (fit)
K^{trans} (ST)	0.96	0.96	-0.02	-0.02	1.17	1.16	0.93	0.96
v_e (ST)	0.91	0.91	0.07	0.07	0.81	0.81	0.82	0.85
K^{trans} (EX)	0.96	0.96	-0.01	-0.01	1.04	1.11	0.96	0.97
v_e (EX)	0.90	0.90	0.08	0.07	0.78	0.80	0.80	0.83
v_p (EX)	0.98	0.98	0.00	0.00	1.52	0.99	0.88	0.69

The parameters resulting from the bi-exponential decay analysis resulted in the following parameters for the population VIF data: for Gd-DTPA, a_1 = 0.0516 kg/L, m_1 = 0.0450 sec^{-1}, a_2 = 0.0820 kg/L, and m_2 = 1.3045 sec^{-1}; for P846, a_1 = 0.0602 kg/L, m_1 = 0.0452 sec^{-1}, a_2 = 0.0516 kg/L, and m_2 = 0.4920 sec^{-1}.

Parameters determined using the original sampled (1.5 sec) tissue signal and the parameters obtained by downsampling (ds) the data (30 sec) displayed an insignificant difference in absolute parametric values. Table VI-9 shows absolute K^{trans} (ST) and v_e (ST) for all animals derived using the VIF_{ind} and both raw and downsampled data. A two tailed t-test showed that there were no statistical significances between these parameters; while not shown here, no statistical differences between using the raw or downsampled data were found in the EX model data or VIF_{pop} data.

TABLE VI-9

ABSOLUTE PARAMETER VALUES PRODUCED FROM RAW AND DOWNSAMPLED VIF DATA .

Mouse	K^{trans} (ST) (min^{-1}) from VIF_{ind}		v_e (ST) from VIF_{ind}	
	raw	**ds**	**raw**	**ds**
1	0.128	0.166	0.374	0.354
2	0.053	0.053	0.174	0.145
3	0.064	0.091	0.483	0.634
4	0.393	0.377	0.668	0.651
5	0.128	0.162	0.326	0.308
6	0.224	0.193	0.322	0.290
7	0.280	0.303	0.745	0.710
8	0.047	0.057	0.068	0.096
9	0.117	0.120	0.374	0.365
10	0.102	0.132	0.314	0.192
11	0.025	0.044	0.168	0.185
p-value	**0.792**		**0.933**	

The effect of using the population vs. the individual VIF to fit the data still follows a similar correlation trends as presented for the ROI analysis using the original temporal resolution. Statistical analysis showed that there was no significant difference between parameters found using the VIF_{ind} on the downsampled data versus the VIF_{pop} on the downsampled data, shown in Table VI-10.

TABLE VI-10
STATISTICAL COMPARISON PARAMETERS PRODUCED BY RAW AND DOWNSAMPLED TISSUE CURVES USING VIF_{IND} AND VIF_{POP}.

	Pearson		**Intercept**		**Slope**		**CCC**	
	Gd-DTPA	**Gd-DTPA (ds)**	**Gd-DTPA**	**Gd-DTPA (ds)**	**Gd-DTPA**	**Gd-DTPA (ds)**	**Gd-DTPA**	**Gd-DTPA (ds)**
K^{trans} (ST)	0.95	0.96	-0.02	-0.02	1.20	1.17	0.93	0.94
v_e (ST)	0.83	0.89	0.08	0.08	0.74	0.69	0.82	0.85
K^{trans} (EX)	0.96	0.96	-0.01	-0.02	1.06	1.13	0.96	0.95
v_e (EX)	0.81	0.84	0.09	0.13	0.69	0.55	0.8	0.75
v_p (EX)	0.98	0.97	0.00	0.00	1.54	1.00	0.88	0.95

Discussion

Measuring the vascular input function is one of the more challenging aspects of DCE-MRI measurement and quantification, particularly in small animals. In Pickup, *et al.*, only four mice were used in the study, and spatial resolution was sacrificed in order to obtain an adequate temporal resolution for VIF acquisition (1). A very comprehensive study by McGrath *et al*., compared the VIF in rats with frequently used VIF models and the population averaged VIF and reported the downstream effects on pharmacokinetic modeling parameters (2). To the best of our knowledge, no study has extensively examined the VIF in mice and the effects on pharmacokinetic modeling parameters. Additionally, this study has eliminated injection variability in that an automated syringe pump was used with identical settings for all animals.

The temporal resolution requirements for measuring an accurate VIF typically are not compatible with the spatial resolution requirements of imaging a large heterogeneous

tumor. In order to alleviate these technical demands, the use of a population VIF has been proposed, and this work has focused on assessing the feasibility and resultant error when using a population VIF instead of acquiring individual VIFs in mice. In order to construct an accurate population VIF, a consistent injection protocol must be established. The rapid injection protocol in this study was used for a two main reasons. Firstly, the shorter injection time has been shown to more closely relate K^{trans} to the initial uptake of the contrast agent within a given voxel as well as more closely relate v_e to the accumulation of the agent extravascularly using this specific model (14). Additionally, a rapid injection protocol yields a rapidly rising, short-lived peak concentration which is typically the most difficult to capture and characterize; thus, the "worst-case" VIF was used in this work to compare the downstream effects on the kinetic parameters. We would anticipate the kinetic parameter comparison using a longer, slower injection protocol to be similar. Other injection protocols can be found in the literature (15,16)

Care was also taken to minimize the error associated with a given VIF. A low dose of Gd-DTPA (0.05 mmol/kg) was used to reduce T_2^* effects. Additionally, gated scout images allowed placement in the left ventricle such that: 1) the number of voxels in the center of chamber was maximized to reduce partial volume effects from the ventricle walls; 2) the slice was the farthest away from the mitral valve to reduce flow effects thereby minimizing artifacts due to cardiac motion; and 3) an automated syringe pump was used to ensure reproducible delivery of the contrast agent to all mice. These details are critical to measure individual VIFs that will ultimately produce a population VIF.

In Fig. VI-1, the population VIFs for Gd-DTPA and P846 have a relatively low standard deviation at the peak of the curve which suggests these individual VIFs are

reaching very similar peak concentration in the LV. In the Gd-DTPA and P846 data, the higher variability in the wash-out manifests itself primarily in the v_e parameter while the smaller variability at the peak and wash-in phase seem to be reflected in the high correlations between K^{trans} measures.

In the ROI analysis, correlations and trends for K^{trans} and v_e are similar for the standard and extended models as well as the different contrast agents. K^{trans} (both *ST* and *EX*) displays a high correlation, indicating that parameters produced using the VIF_{pop} are very similar to those that are produced using the VIF_{ind}. For v_e, however, the CCCs are lower, which is most likely an indirect manifestation of the larger wash-out variability seen in Fig. VI-1. However, the ROI-based analysis did not appear to be as sensitive to this variability as the voxel-based comparison. The ROI-based analyses suggest that using a population VIF produced statistically similar parameters, especially for K^{trans} (*ST* and *EX*) indicated by a correlation with unity > 0.90; additionally, the resulting power analysis suggests an increase of at most 35% in the population can preserve the power when using a population VIF versus an individual VIF. For v_e and v_p parameters, the results did not follow a similar trend as they tended to drift from unity. However, these parameters show a large degree of linearity, which indicates that an overall shift in the wash-out period of the VIF_{ind} compared to that of the VIF_{pop} would produce parameters that were linearly shifted as well (either over- or underestimated). While this is not ideal, the strong linearity of these parameters suggests that the VIF shape is similar. Thus, if the VIF_{pop} was used in a treatment study, for example, the pre- and post-treatment values for v_e would both be potentially over- or underestimated but the relative change in the parameter may remain the same. Interestingly, since the power analysis relies on inter-

and intra-subject variability, in order to achieve the same power in measuring v_e using Gd-DTPA, no increase in population is required; in fact, 10-15% less animals can be used (see Table VI-2).

The same cannot be said for P846, which requires the population size to double if a population VIF is used and v_e is the primary metric (Table VI-2). One of the goals of using larger contrast agents such as P846 is to differentiate flow and permeability characteristics in the tissue. Gd-DTPA is small (~ 0.5 kDa); thus, clearance and extravasation to the tissue may be more flow-limited when compared to a larger agent. However, by inspecting the VIFs in Fig. VI-1, it is evident that the larger contrast agent provides a longer peak and wash-out period. The permeability of tissue and the ability to clear a contrast agent are characteristics that are unique to each animal; thus, for smaller agents such as Gd-DTPA the differences in permeability and clearance do not have as great an impact on the VIF_{ind} or VIF_{pop}. However, with P846 the permeability and clearance rate become a more important factor in both the VIF_{ind} and tissue curves; hence, the greater disparity between parameter pairs such as v_e and v_p, indicate that the variability in permeability and clearance for P846 between animals may lead to greater differences between the VIF_{ind} and VIF_{pop}.

The voxel-based data follows a similar trend as the ROI-based analysis; however, the sensitivity to the differences between parameter pairs is magnified, as illustrated in Fig. VI-3 and VI-4. The parametric maps show that, in this particular mouse, the wash-in and peak phase of the VIF are similar, thus producing K^{trans} (both *ST* and *EX*) data points that fall along the line of identity. In this mouse, the v_e and v_p parameters obtained from the VIF_{pop} are always overestimated from the parameters produced from the VIF_{ind}. The plots

show this linear increase, which is an indirect demonstration of the VIF_{ind} curve being overestimated by the VIF_{pop}. It is also worth noting that, as mentioned in the Methods section, some voxel signal data were fit using the VIF_{ind} but could not be fit with VIF_{pop} (i.e., the parameters returned using VIF_{pop} were outside a physiologically relevant range). These data were not included in the above analysis as these "outlier" data tended to severely skew linear regression analysis. Instead, these occurrences were tallied to show the frequency of the occurrences within each mouse and shown in Table VI-11.

TABLE VI-11
ILL-FIT VOXEL DATA FOR GD-DTPA AND P846.

Mouse ID	Gd-DTPA	P846
	Percentage of voxels fit only by VIF_{ind} but not VIF_{pop}	**Percentage of voxels fit only by VIF_{ind} but not VIF_{pop}**
1	0	0
2	3	0
3	0	0
4	0	0
5	0	0
6	0	11
7	0	5
8	0	8
9	0	2
10	52	*na*
11	42	*na*

Additional results comparing a fitted VIF_{ind} and a fitted VIF_{pop} showed similar statistical trends (refer to Tables VI-7 and VI-8) to that of comparing the raw VIF_{ind} and a raw VIF_{pop} suggesting than if bi-exponentially fit data is used for the VIF, the conclusions discussed here remain valid. By examining a temporal resolution that better reflects a more realistic application of obtaining high resolution, high signal to noise scans, it was concluded that while the downsampled data may produce more inaccurate parameter values (refer to Table VI-9) but the comparative trends remain the same; in

other words, the absolute values of the parameters changed but the differences between parameters found using the downsampled data/VIF_{ind} and downsampled data/VIF_{pop} were similar to those reported above using the tissue curve that was sampled more frequently (refer to Table VI-10). As noted in the results examining the effects of temporal resolution, the comparison of kinetic parameters using a VIF_{pop} relative to the VIF_{ind} is of interest; the physiological meaning of these parameters and how they change under various conditions is important but is beyond the focus of this current work.

The results of this study indicate that for animals imaged with Gd-DTPA, K^{trans} (obtained by both the standard and extended models) estimated using a population based VIF have a very high correlation with K^{trans} parameters estimated using an individual VIF on both a global (ROI) and local (voxel) level. An increase 15-35% in population (potentially only 2-4 animals) can preserve the power if the VIF_{pop} is used instead of the VIF_{ind}. Since K^{trans} is typically the primary metric for the majority of DCE-MRI studies, this work supports the use of a population derived VIF obtained with a strict injection protocol and additional animals to preserve the power of the study.

References

1. Pickup S, Zhou R, Glickson J. MRI estimation of the arterial input function in mice. Acad Radiol 2003;10(9):963-968.
2. McGrath DM, Bradley DP, Tessier JL, Lacey T, Taylor CJ, Parker GJ. Comparison of model-based arterial input functions for dynamic contrast-enhanced MRI in tumor bearing rats. Magn Reson Med 2009;61(5):1173-1184.
3. Weinmann HJ, Brasch RC, Press WR, Wesbey GE. Characteristics of gadolinium-DTPA complex: a potential NMR contrast agent. AJR Am J Roentgenol 1984;142(3):619-624.
4. Peldschus K, Hamdorf M, Robert P, Port M, Graessner J, Adam G, Herborn CU. Contrast-enhanced magnetic resonance angiography: evaluation of the high relaxivity low diffusible gadolinium-based contrast agent P846 in comparison with gadoterate meglumine in rabbits at 1.5 Tesla and 3.0 Tesla. Invest Radiol 2008;43(12):837-842.
5. Heilmann M, Vautier J, Robert P, Volk A. In vitro setup to study permeability characteristics of contrast agents by MRI. Contrast Media Mol Imaging 2009;4(2):66-72.
6. Fries P, Runge VM, Bucker A, Schurholz H, Reith W, Robert P, Jackson C, Lanz T, Schneider G. Brain tumor enhancement in magnetic resonance imaging at 3 tesla: intraindividual comparison of two high relaxivity macromolecular contrast media with a standard extracellular gd-chelate in a rat brain tumor model. Invest Radiol 2009;44(4):200-206.
7. Parker GJ, Baustert I, Tanner SF, Leach MO. Improving image quality and T(1) measurements using saturation recovery turboFLASH with an approximate K-space normalisation filter. Magn Reson Imaging 2000;18(2):157-167.
8. Bluml S, Schad LR, Stepanow B, Lorenz WJ. Spin-lattice relaxation time measurement by means of a TurboFLASH technique. Magn Reson Med 1993;30(3):289-295.
9. Haase A. Snapshot FLASH MRI. Applications to T_1, T_2, and chemical-shift imaging. Magn Reson Med 1990;13(1):77-89.
10. Landis CS, Li X, Telang FW, Coderre JA, Micca PL, Rooney WD, Latour LL, Vetek G, Palyka I, Springer CS, Jr. Determination of the MRI contrast agent concentration time course in vivo following bolus injection: effect of equilibrium transcytolemmal water exchange. Magn Reson Med 2000;44(4):563-574.
11. Trune DR, Kempton JB, Gross ND. Mineralocorticoid receptor mediates glucocorticoid treatment effects in the autoimmune mouse ear. Hear Res 2006;212(1-2):22-32.
12. Aref M, Chaudhari AR, Bailey KL, Aref S, Wiener EC. Comparison of tumor histology to dynamic contrast enhanced magnetic resonance imaging-based physiological estimates. Magn Reson Imaging 2008;26(9):1279-1293.
13. Parker GJ, Roberts C, Macdonald A, Buonaccorsi GA, Cheung S, Buckley DL, Jackson A, Watson Y, Davies K, Jayson GC. Experimentally-derived functional form for a population-averaged high-temporal-resolution arterial input function for dynamic contrast-enhanced MRI. Magn Reson Med 2006;56(5):993-1000.

14. Tofts PS, Brix G, Buckley DL, Evelhoch JL, Henderson E, Knopp MV, Larsson HB, Lee TY, Mayr NA, Parker GJ, Port RE, Taylor J, Weisskoff RM. Estimating kinetic parameters from dynamic contrast-enhanced T(1)-weighted MRI of a diffusable tracer: standardized quantities and symbols. J Magn Reson Imaging 1999;10(3):223-232.
15. Tang JS, Choy G, Bernardo M, Thomasson D, Libutti SK, Choyke PL. Dynamic contrast-enhanced magnetic resonance imaging in the assessment of early response to tumor necrosis factor alpha in a colon carcinoma model. Invest Radiol 2006;41(9):691-696.
16. Bradley DP, Tessier JL, Checkley D, Kuribayashi H, Waterton JC, Kendrew J, Wedge SR. Effects of AZD2171 and vandetanib (ZD6474, Zactima) on haemodynamic variables in an SW620 human colon tumour model: an investigation using dynamic contrast-enhanced MRI and the rapid clearance blood pool contrast agent, P792 (gadomelitol). NMR Biomed 2008;21(1):42-52.

CHAPTER VII

ASSESSING THE EFFICACY OF A NOVEL JAK2 INHIBITOR (AZD 1480) USING DIFFUSION WEIGHTED AND DYNAMIC CONTRAST-ENHANCED MAGNETIC RESONANCE IMAGING COMPARED TO POSITIVE (AZD 2171) and VEHICLE CONTROLS

Introduction

As mentioned previously in Chapter III, Jak2 inhibition reduces the levels of Stat3 that is persistently activated in many cancer lines; Stat3 is responsible for the transcription of factors that promote tumor growth (1), halt apoptosis pathways (1,2), and increase angiogenic activity (3). AZD 1480 is a novel drug that acts as small molecule, inhibiting Jak2 and thereby suppressing levels of Stat3 within tumors (4). Both diffusion weighted magnetic resonance imaging (DW-MRI) and dynamic contrast enhanced MRI (DCE-MRI) have been used frequently to monitor cancer treatment, as discussed in previous chapters. Since two of the pathways affected by Jak2 inhibition involve reduced proliferation/increased apoptosis and reduced angiogenic activity, this work seeks to assess the utility of DW-MRI and DCE-MRI in assessing the efficacy of AZD 1480, a novel Jak2 inhibiting drug, compared to a potent anti-angiogenic drug (AZD 2171) (5) and vehicle controls at early treatment time points.

Methods

Tumor Model

Calu-6 human lung carcinoma cells were grown according to the protocol developed in Wedge *et al* (6). Briefly, the cells were grown in a media containing 10% FCS and 2

mM L-glutamine in Eagle's Minimal Essential Medium with 1% sodium pyruvate (100 mM) and 1% non-essential amino acids. Cells growing at 80% confluence were harvested, and a single cell suspension containing 1×10^6 cells suspended in 100 µL of medium were injected subcutaneously on the flank. Tumors were grown for 15 to 20 days to reach a size of approximately 200-250 mm^3 before imaging.

Animal Model

Thirty adult female *fox nu/nu* (8-10 weeks of age) were purchased from Charles River Laboratories, housed in pathogen-free facilities with a 12-hour light/dark cycle (6 AM–6 PM), and provided with rodent chow and tap water *ad libitum*. For DCE-MRI studies, a 26-gauge jugular catheter was surgically implanted to allow for delivery of the contrast agent. All animals were imaged at three time points: a baseline scan was acquired prior to any treatment, and then two subsequent sessions at day 3 and day 5 after the initiation of treatment. The mice were then humanely sacrificed for histological analysis of tumor tissues. During all imaging procedures, the mice were anesthetized using a 2%/98% isoflurane/oxygen mixture. Body temperature was maintained *via* a flow of warm air through the magnet bore, and temperature and respiratory rate were monitored throughout the entire experiment. All procedures in the experiment were reviewed and approved by our Institutional Animal Care and Use Committee.

Treatment

The vehicle for AZD 1480 was prepared using 0.1 mL of Tween80 (Sigma Aldrich, St. Louis, MO), 0.5 g of methylcellulose powder and 100 mL of distilled water stirred

overnight. A vehicle was added to a dose of 50 mg/kg of AZD 1480 such that the administered volume was 10 mL/kg. HCl was added to the drug to ensure the pH was 2.0, following the manufacturer's recommended protocol. The vehicle for AZD 2171 was prepared using 0.1 mL of Tween80 added to 100 mL of distilled water. Vehicle was added to a dose of 6 mg/kg such that the administered volume was 10 mL/kg. All drugs and vehicles were stored at 4° C. Thirty mice were randomly assigned to one of the following three treatment groups once tumor volumes were approximately 200 mm^3: 50 mg/kg AZD 1480, *p.o. q.d.*, 6 mg/kg, AZD 2171 *p.o. q.d.*, and vehicle control, *p.o. q.d.*

Data Acquisition

DW-MRI

Animals were imaged on the 9.4T MR scanner (Varian, Palo Alto, CA) with a 38-mm quadrature coil (Varian, Palo Alto, CA) at all three time points. Due to technical issues, three animals had day 5 data and four animals had day 3 data acquired on a 7T MR scanner (Varian, Palo Alto, CA) using identical protocols. A gradient echo scout sequence was used to locate the tumor tissue. Once the region of interest was located, fifteen slices were imaged (1 mm thick, interleaved) with diffusion weighting using a gated and navigated pulsed gradient spin echo sequence. DW-MRI parameters were as follows: TR\TE\α = 2000 ms\42 s\15°, acquisition matrix = 128^2, FOV = $(35\ mm)^2$, and NEX = 2 with Δ = 35.00 ms and δ =5.00 ms for b-values of 150.88, 500.2, and 800.22 mm^2/s. The equivalent diffusion distance examined was approximately 13 μm as described in Chapter IV.

DCE-MRI

After DW-MRI, pre-contrast T_1 maps were obtained using an inversion recovery snapshot FLASH (Fast Low Angle SHot) gradient echo sequence with an adiabatic inversion pulse over nine inversion times (TI) ranging from 20 – 10000 ms. Imaging parameters were as follows: *TR**TE* \α= 12100 ms\ 3.44 ms\15° and NEX = 4, FOV = 35 mm^2, and matrix = 128^2. The data were then fit to Eqn. (II-10), to obtain T_1 maps for all fifteen slices of data. The DCE-MRI protocol employed a T_1-weighted, gradient echo sequence to obtain 40 serial images for each of fifteen axial planes in 18 minutes of imaging. The parameters were as follows: *TR**TE**α* = 100 ms\2.83 ms\25°, NEX = 2, with the same acquisition matrix and FOV as for the T_1 map. A bolus of 0.1 mmol/kg Gd-DTPA was delivered over 2.5 seconds with an automated Harvard pump (2.4 mL/min) *via* a jugular catheter beginning after the acquisition of the fifth dynamic image.

Data Analysis

DW-MRI

The derivation for the signal intensity relationship with diffusion weighted data was described in Chapter IV. Briefly, the diffusion weighted images acquired at three separate *b* values, 150.88, 500.2, and 800.22 mm^2/s,were fit to Eqn. (IV-9) to extract the *ADC* values at every ROI and voxel location.

DCE-MRI

Data collected for the T_1 map were fit using a nonlinear least squares method in Matlab 2008a (The Mathworks, Natick, MA, USA) to Eqn. (II-10). Once pre-contrast T_1

maps were calculated, Eqn. IV-2 was used to extract pharmacokinetic parameters of K^{trans} and v_e (7). The derivation of this model is described in Chapter IV. The signal time course from the tissue for each voxel was fit using a nonlinear least squares fit to Eqn. (IV-2) by incorporating 1) the relationship between the signal and the initial R_1/T_1 values by means of the method described by Landis, et al., Eqn. (VI-1) (8), 2) the fast exchange limit (FXL) model with relaxivity for Gd-DTPA at 9.4T was found to be 4.8 $mM^{-1}s^{-1}$ (unpublished results, see Figure V-1) and a hematocrit value of 0.45, based on literature values (9), and 3) a population-derived VIF or $C_p(t)$ derived from a cohort of ten *fox nu/nu* mice found identical to the study described in the previous chapter.

Histology

On day six (one day after the final imaging session), animals were dosed and sacrificed using CO_2 two hours later. These samples were taken on the final day to mimic the imaging timeline; this ensured that the histology and molecular markers would reflect two hours after dosing just as when imaging was performed. The tumor tissue was excised, placed into tissue cassettes, and soaked in 10% Formalin (Fisher, Pittsburgh, PA) for 24-48 hours. The tissue was then store in 70% ethanol until the all tumors from this study were excised. Subsequent immunohistochemistry was performed at the AstraZeneca facility in Waltham, MA. Samples were paraffin embedded and sectioned at 5 μm thickness. Immunohistochemistry was performed on the Ventana Discovery XT Autostainer using the standard CC1 protocol. In order to verify proper AZD 1480 dosing, samples were stained with phosphoylated Stat3 (pStat3) antibody (Cell Signaling Technology, Danvers, MA). Additionally cellular proliferation, apoptosis, microvessel

density, and cell density estimates were found using Ki-67 (Cell Signaling Technology, Danvers, MA), cParp (Cell Signaling Technology, Danvers, MA), CD31 (Cell Signaling Technology, Danvers, MA) and hematoxylin/eosin (H&E) staining (Ventana, Tucson, AZ), respectively.

From the CD31 stained slides, microvessel density was calculated by using the Aperio (Vista, CA) Microvessel Analysis software; briefly, the software was tuned to detect the CD31 stain color and the size of the detected vessels. The algorithm then basis vessel selection on the endothelial areas compared to the lumen areas, and how the regions should be joined together to form a vessel. The number of vessels detected were divided by the area of the field of view in order to determine the microvessel density.

Additionally, Aperio digital histology images of the tumor were acquired at 20× magnification. The Positive Pixel Count Algorithm, developed by Aperio, was used to create maps of intra- and extracellular regions based on intensity thresholding; briefly, based on the intensity of the stains, images were thresholded into four categories: positive (*e.g.*, hemotoxylin), strong (*e.g.*, eosin), weak (*e.g.*, eosin), and no staining (*e.g.*, extracellular regions). A region was drawn to encompass the entire slice of histology data and thresholded as described above. Statistics summarizing the thresholding that include total region area (A_{ROI}) and total stained area (A_{stain}) were used to determine the percentage of extracellular (EC) space as shown below:

$$EC(\%) = \left(1 - \frac{(A_{ROI} - A_{stain})}{A_{ROI}} \right) \cdot 100 \, . \qquad \text{(VII-1)}$$

Statistical Analysis

In order to assess group changes in K^{trans}, and v_e, an ROI was manually drawn on the center slice for each tumor at each time point. The average signal intensity was then fit to Eqn. (IV-2) to obtain parametric values for each animal at baseline, day 3, and day 5. The same ROIs were applied to diffusion-weighted data collected at *b* values of 150.88, 500.2, and 800.22 mm/s^2. The data were then fit to Eqn. (IV-9), as described above, to obtain *ADC* values for all mice at all time points. Before being placed into the appropriate treatment group for analysis, the integrity of the data was examined by using either muscle tissue (DCE-MRI) or water phantom data (DW-MRI) as shown in Fig. VII-1. Briefly, if the muscle curve did not qualitatively follow characteristics of a rapid wash-in and wash-out of CA or if physiologically implausible parameters were returned, the injection was deemed unsuccessful and the DCE-MRI data was not used. Similarly, if the slice used in the DW-MRI comparison had a phantom ADC value outside the range of 0.003 mm^2/s ± 15% (experimentally-derived *ADC* of free water at 34° at 9.4T), then the tumor *ADC* data was also not used. For each treatment group, the average and standard error (1.96 × standard deviation /√n, where *n* is the number of samples) were computed. The percent change from baseline for each animal was also computed, and the average and standard error were calculated. A Wilcoxon signed rank test was used to determine significant differences between each treatment group (both absolute and percent change data) (10). Histological data were quantified using pathological scoring and compared with all imaging metrics.

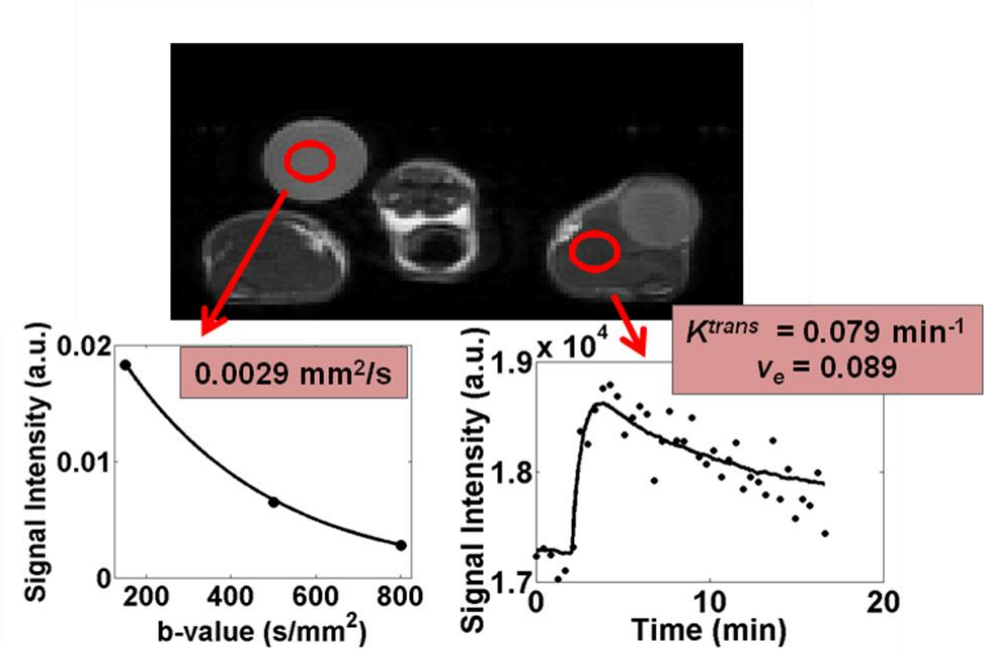

Fig.VII-1. The water phantom in the top right of the figure was used to ensure that ADC values for the interrogated slice were accurate. An example of the DW-MRI fit of this phantom data is shown in the lower left corner. Muscle tissue was used to verify DCE-MRI data integrity. An example of the muscle tissue curve and subsequent fit is shown in the lower right.

Results

In total, N = 12 / N = 10 / N = 9 mice were imaged at three time points for the AZD 2171 / AZD 1480 / CTL groups, respectively. For the DCE-MRI group analyses, N_{2171} = 7 / N_{1480} = 8 / N_{CTL} = 6 animals were used while N_{2171} = 5 / N_{1480} = 9 / N_{CTL} = 7 animals were used in the *ADC* group analysis. The tumor volume changes for all animals are shown in Fig. VII-2, where the square/solid line indicates animals treated with AZD 2171, the circle/dashed line indicates animals treated with AZD 1480 and the triangle/dashed line represents animals in the CTL group. The vertical lines are 1.96 × standard error for each respective group.

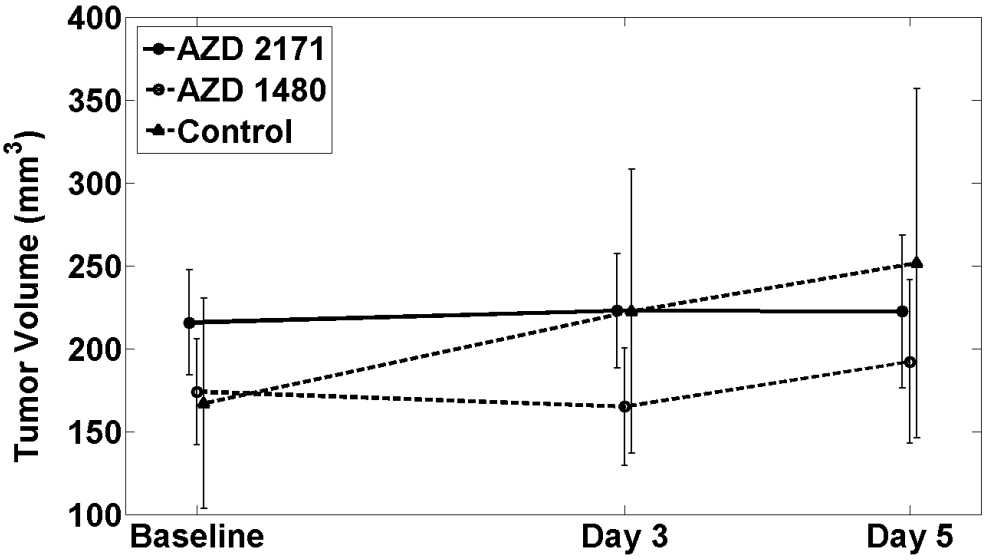

Fig.VII-2 Volumetric data for all animals used in each treatment group. The solid circles/solid line represents the AZD 2171 group while the open circle/dashed line represent the AZD 1480. The control group is represented by the triangle/dashed line with the vertical lines indicating 1.96 × standard error for each time point.

Animals that did not have a characteristic muscle curve (potentially from a damaged catheter line) or inaccurate water phantom *ADC* values (potentially caused by ghosting artifacts) were excluded from further analyses. Average phantom and muscle data are shown in Fig. VII-3.

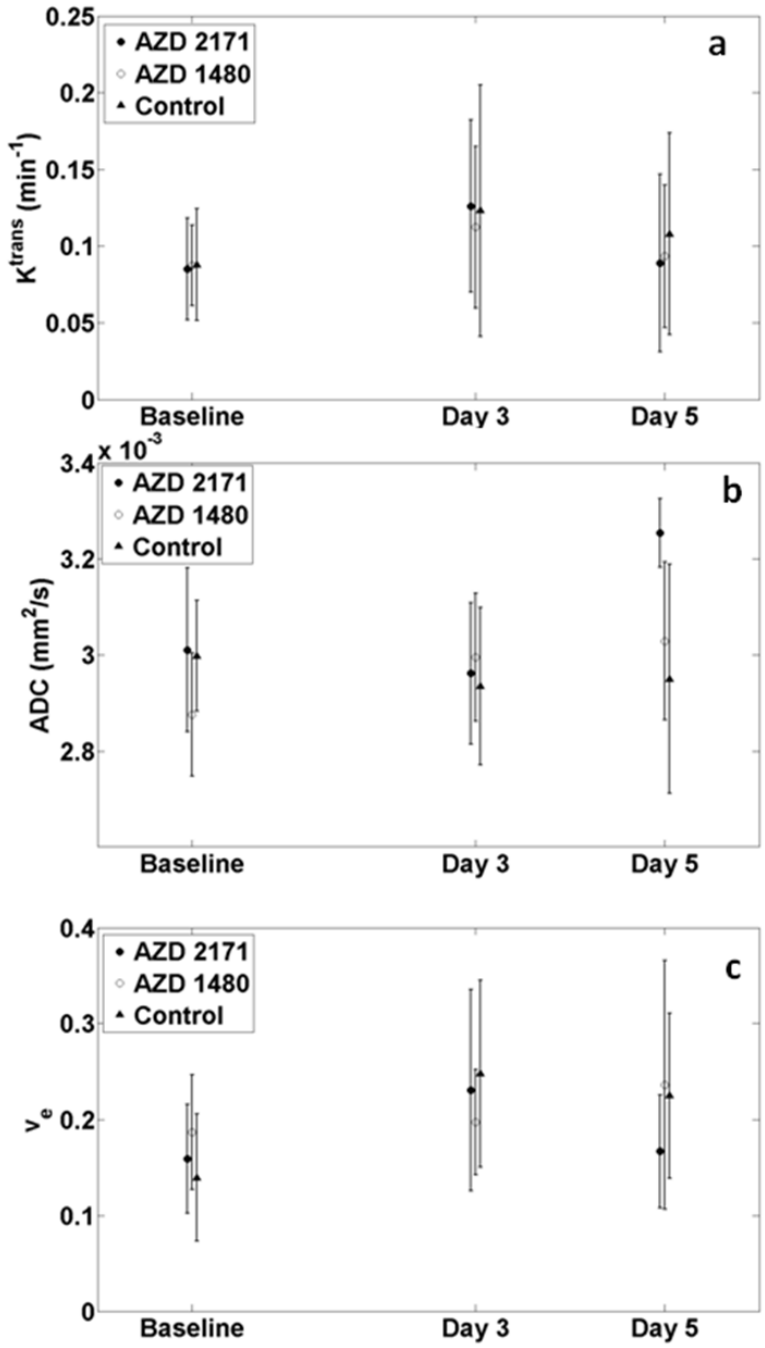

Fig. VII-3. The average K^{trans} (a) and v_e (c) from muscle tissue and *ADC* from the water phantom (b) for each treatment group (AZD 2171 (●), 1480 (○), and Control (▲)) where the standard error bars are represented by the vertical bars.

Group Analyses

The results of the percent change in the group analyses are displayed in Fig. VII-4 (figures displaying individual sample percentages are shown in the Appendix). The AZD 2171 treatment group is denoted by the square and solid line; the AZD 1480 treatment group is denoted by the circle and dashed line while the control (CTL) group is represented by the triangle marker and dashed line. The vertical lines indicate the standard error for each treatment group while the '*' denotes significance (p-value < 0.05) from baseline measurements in the same group.

Animals treated with the positive control, AZD 2171, showed significant decreases in K^{trans} at both day 3 and day 5 with an average percent difference of -29% and -53%, respectively (depicted in Fig VII-4 (a)). The average percent differences in the AZD 1480 treatment group were -21% and -23% for each post-treatment time points while the CTL group showed stable decreases of 26 percent at both subsequent time points. No significant differences were found in either AZD 1480 or CTL groups at either post-treatment time points for K^{trans}. Absolute K^{trans} values for these treatment groups are listed in Tables VII-1 through VII-3.

TABLE VII-1
ABSOLUTE K^{TRANS} VALUES IN THE AZD 1480 TREATMENT GROUP.

ID	Baseline (min^{-1})	Day 3 (min^{-1})	Day 5 (min^{-1})		CD31 Scoring and Description (if available)
1	0.047	0.033	Na	2+	peripheral vessels
2	0.064	0.039	na	na	
3	0.088	0.155	0.059	3+	
4	0.051	0.026	0.026	1+	necrotic tissue
5	0.122	0.069	0.047	3+	attenuated vessels
6	0.040	0.019	na	1+	
7	0.036	0.046	0.042	1+	
8	0.039	0.010	0.037	1+	slit-like morphology

TABLE VII-2
ABSOLUTE K^{TRANS} VALUES IN THE AZD 2171 TREATMENT GROUP.

ID	Baseline (min^{-1})	Day 3 (min^{-1})	Day 5 (min^{-1})		CD31 Scoring and Description (if available)
1	0.050	0.036	0.012	na	
2	0.054	0.056	0.066	2+	attenuated vessels
3	0.041	0.028	na	1+	attenuated vessels
4	0.052	0.021	0.021	1+	attenuated vessels
5	0.094	0.089	0.031	na	
6	0.046	0.040	0.022	1+	necrotic tissue
7	0.068	0.019	0.009	1+	slit-like morphology

TABLE VII-3
ABSOLUTE K^{TRANS} VALUES IN THE CONTROL GROUP.

ID	Baseline (min^{-1})	Day 3 (min^{-1})	Day 5 (min^{-1})		CD31 Scoring and Description (if available)
1	0.048	0.053	0.055	3+	
2	0.052	0.019	0.021	2+	
3	0.096	0.054	0.060	3+	
4	0.104	0.052	0.037	3+	diffuse distribution
5	0.062	0.071	0.073	na	
6	0.030	na	0.022	na	

In Fig. VII-4 (b), the percent change in *ADC* shows that both treatment groups demonstrate an increasing trend with a significant increase for the AZD 1480 at both day 3 (63%) and day 5 (49%) post-treatment. While the AZD 2171 group shows an increase on day 5 for *ADC*, only three animals were available at this final time point so that statistical significance could not be achieved. Also of note, the CTL group trended negatively, suggesting that apparent diffusion decreased as the tumor grew. Absolute *ADC* values for the three treatment groups are listed in Tables VII-4-6.

TABLE VII-4
ABSOLUTE *ADC* VALUES IN THE AZD 1480 TREATMENT GROUP.

ID	Baseline ($\times 10^{-4}$ mm^2/s)	Day 3 ($\times 10^{-4}$ mm^2/s)	Day 5 ($\times 10^{-4}$ mm^2/s)
1	3.61	6.85	8.76
2	5.12	6.29	na
3	6.41	na	11.0
4	4.79	8.55	4.80
5	7.17	7.64	12.2
6	5.98	na	9.32
7	9.24	na	11.6
8	6.01	na	6.59
9	5.61	na	4.47

TABLE VII-5
ABSOLUTE *ADC* VALUES IN THE AZD 2171 TREATMENT GROUP.

ID	Baseline ($\times 10^{-4}$ mm^2/s)	Day 3 ($\times 10^{-4}$ mm^2/s)	Day 5 ($\times 10^{-4}$ mm^2/s)
1	7.32	4.66	7.25
2	7.71	8.72	na
3	6.85	3.76	10.1
4	6.70	10.1	8.46
5	3.95	7.04	Na

TABLE VII-6
ABSOLUTE *ADC* VALUES IN THE CONTROL GROUP.

ID	Baseline ($\times 10^{-4}$ mm^2/s)	Day 3 ($\times 10^{-4}$ mm^2/s)	Day 5 ($\times 10^{-4}$ mm^2/s)
1	8.90	na	6.84
2	8.55	5.23	4.07
3	7.48	na	na
4	3.98	9.03	na
5	5.17	8.16	4.08
6	7.57	6.66	na
7	6.01	3.59	na

In the final panel of Fig. VII-4 (c), the group changes for v_e are demonstrated. No significant changes in v_e were illustrated with the exception of day 5 of AZD 2171 treatment, which reflected a significant decrease at this time point. The absolute values of v_e found for all animals in each treatment group are listed in Tables VII-7 through 9.

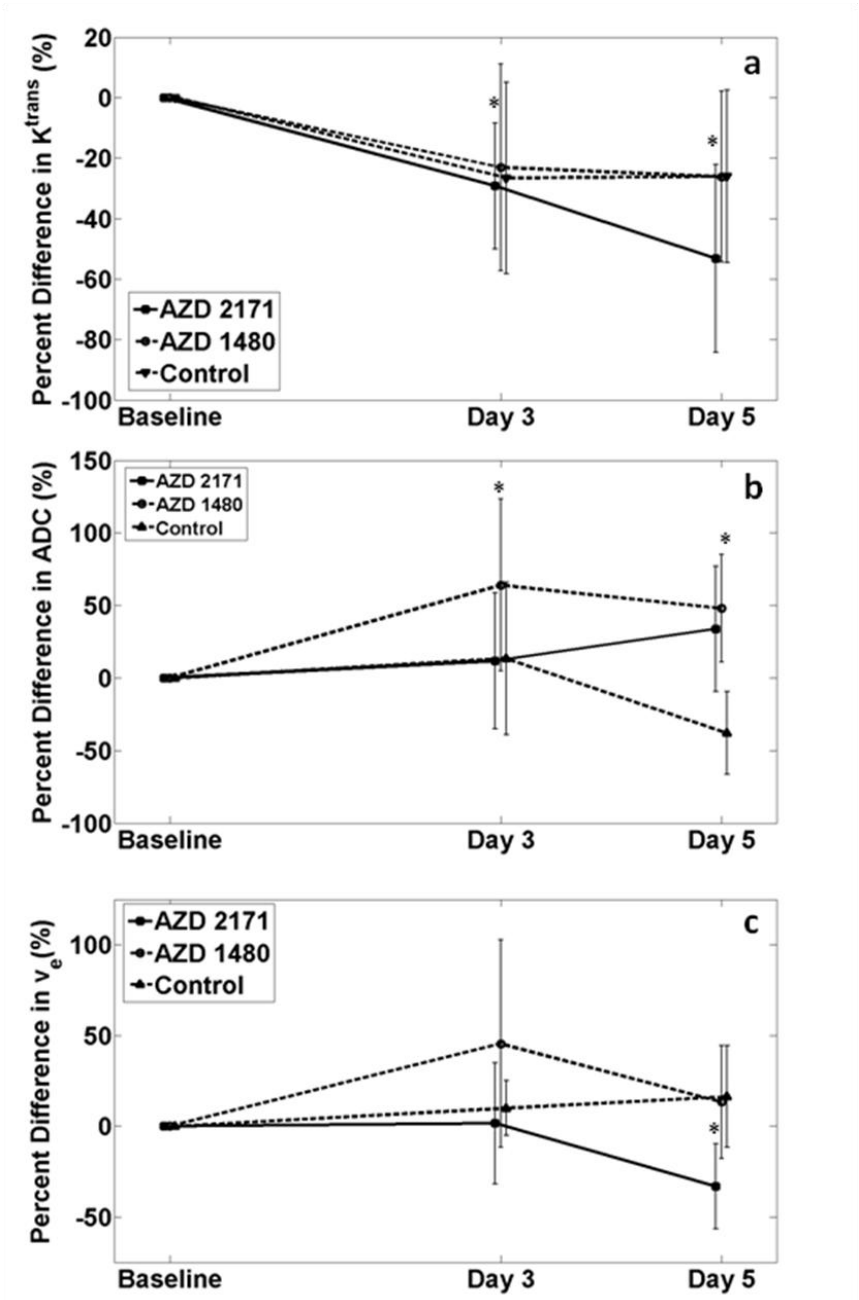

Fig. VII-4. Each panel demonstrates the percent change from baseline for K^{trans}, *ADC*, and v_e, respectively, from a center slice ROI where AZD 2171 (■), 1480 (●), and Control (▲) with the standard error bars are represented by the vertical bars. P-values less than 0.05 are noted by the *. Statistical significances were found for K^{trans} in the AZD 2171 treatment group while AZD 1480 day 3 and day 5 data showed significant increases in *ADC*. A significant decrease was found for v_e in the AZD 2171 treatment group.

TABLE VII-7
ABSOLUTE v_E VALUES IN THE AZD 1480 TREATMENT GROUP.

ID	Baseline	Day 3	Day 5
1	0.966	0.748	na
2	0.477	0.668	na
3	0.456	0.563	0.354
4	0.661	0.726	0.880
5	0.692	0.353	0.721
6	0.279	0.866	na
7	0.333	0.450	0.290
8	0.126	0.273	0.207

TABLE VII-8
ABSOLUTE v_E VALUES IN THE AZD 2171 TREATMENT GROUP.

ID	Baseline	Day 3	Day 5
1	0.536	0.544	0.192
2	0.284	0.277	0.263
3	0.484	0.547	na
4	0.292	0.395	0.294
5	0.393	0.321	0.322
6	0.248	0.405	0.146
7	0.656	0.129	0.206

TABLE VII-9
ABSOLUTE v_E VALUES IN THE CONTROL GROUP.

ID	Baseline	Day 3	Day 5
1	0.347	0.478	0.526
2	0.236	0.231	0.344
3	0.551	0.584	0.395
4	0.350	0.399	0.268
5	0.276	0.259	0.377
6	0.214	na	0.246

Three representative curves (representing each time point) from a mouse in each treatment group are shown in Fig. VII-5. The dynamic data and curve fit (in black) were

taken from baseline while the red and blue fit lines indicate day 3 and day 5 data, respectively. Panel (a) shows the dramatic efficacy of AZD 2171 on K^{trans} (denoted by the arrow) while panel (b) and panel (c) reiterate the group average results for AZD 1480 and CTL, respectively. In both (b) and (c), K^{trans} changes very little or without trend (as denoted by the arrows), whereas this is a marked decrease in this parameter in panel (a).

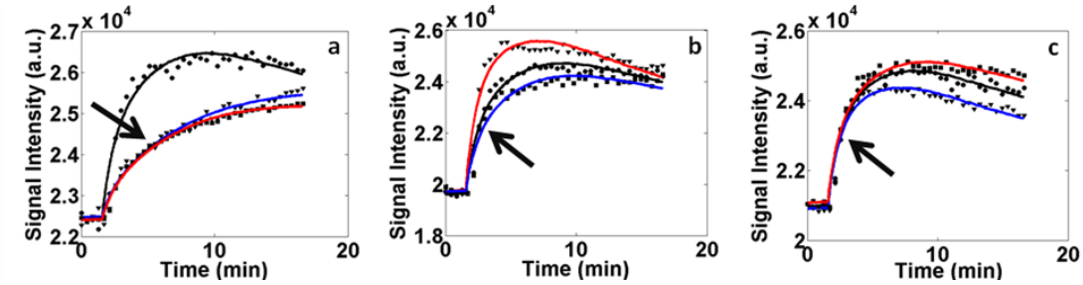

Fig.VII-5 Example DCE-MRI curves from each treatment group. Panel (a) shows a subject from the AZD 2171 treatment group with the black line indicating the baseline, the red line indicating day 3 data, and the blue line representing day 5 data. As noted by the arrow, there is dramatic decrease in K^{trans} for the AZD 2171 group. Panel (b) shows ROI curves from the AZD 1480 group with the arrow showing that no specific pattern in K^{trans} can be detected; similarly, panel (c), representing the control group, shows little detectable change in K^{trans} values.

Histogram Analyses

To further explore the efficacy of K^{trans}, *ADC*, and v_e to report on these treated animals, parametric maps and histograms were constructed. Fig. VII-6 illustrates a panel of K^{trans} maps for each treatment group (rows: AZD 2171, AZD 1480, and CTL) at each time point (columns: baseline, day 3, and day 5). The corresponding histograms for the slice data is represented in the final column. Both the maps and the histograms confirm a significant decrease in K^{trans} values for the AZD 2171 treatment group, shown by the arrow (a, b, c, and d) while little change or trend is noted in the AZD 1480 group (e, f, g,

and h). Interestingly, in this CTL animal, higher K^{trans} values are found at the day 5 time point, as shown by the arrow (i, j, k, and l).

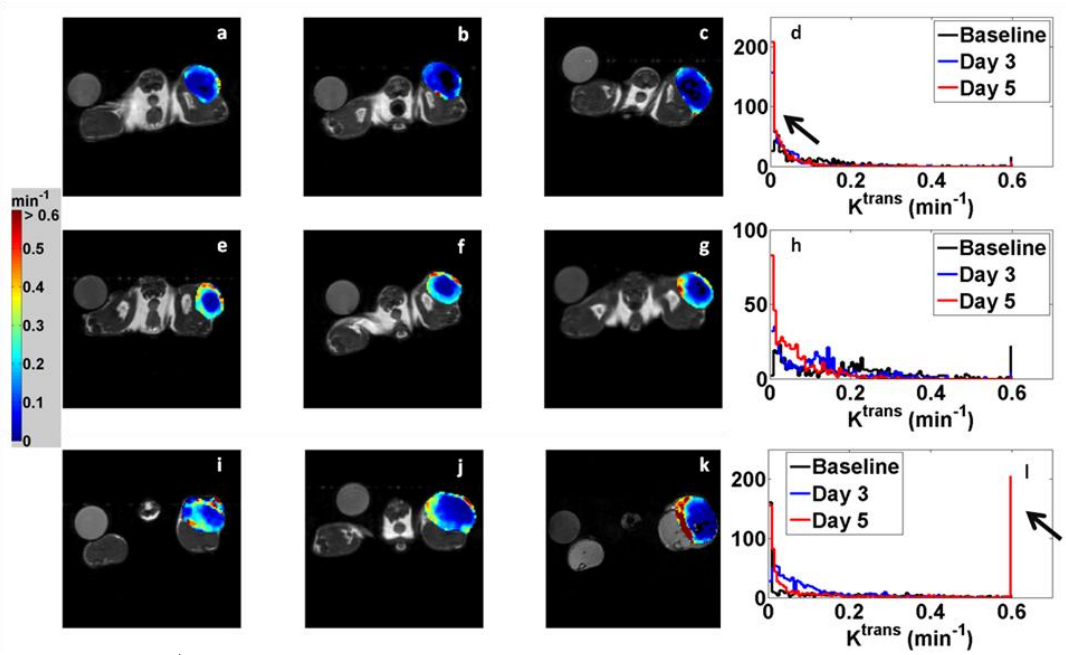

Fig. VII-6. K^{trans} parametric maps for representative mice from each treatment group. The columns indicate baseline, day 3 and day 5 time points while each row shows the AZD 2171 (a-d), AZD 1480 (e-h), and Control groups (i-l). In panel d, the arrow emphasize an increase in lower K^{trans} values by day 5 unlike in panel l where the arrow indicates more of an increase in higher K^{trans} values in the Control group.

ADC maps and histograms were also constructed and displayed in Fig. VII-7. In a similar fashion, the treatment groups are displayed in the rows (AZD 2171, AZD 1480 and CTL groups) while each column represents the imaging time points (baseline, day 3, and day 5). The *ADC* maps do not show a dramatic difference in the AZD 2171 animal (a, b, c, and d) while there is a clear increase in *ADC* values for the AZD 1480 animal (e, f, g, and h). The CTL group (i, j, k, and l) shows a decrease *ADC* values that reflect the group analyses mentioned above.

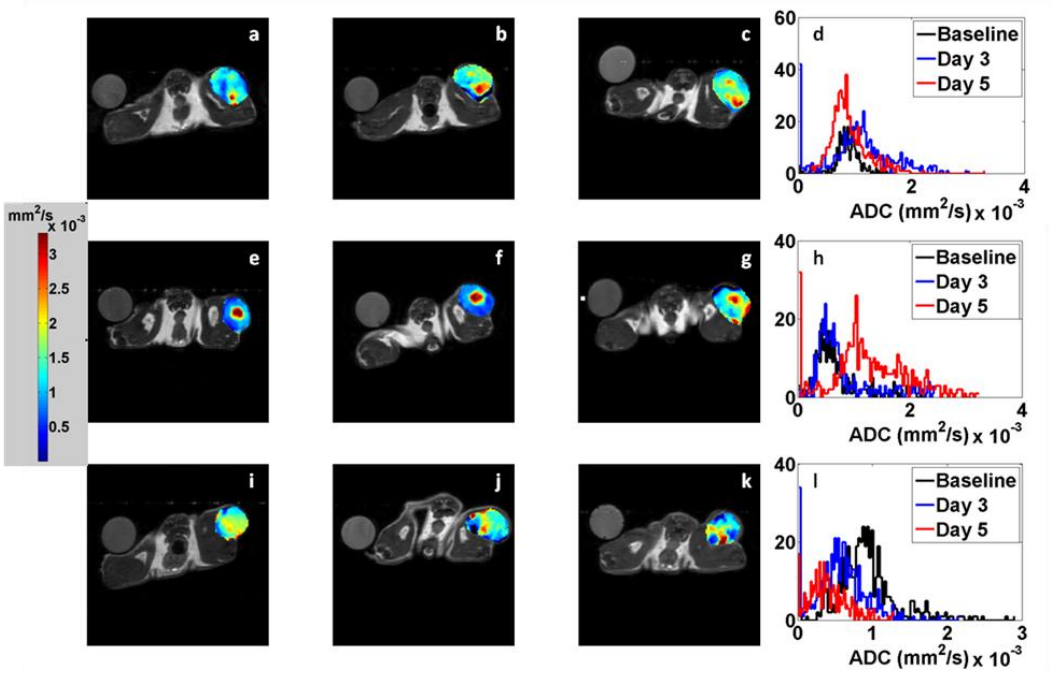

Fig. VII-7. *ADC* parametric maps for representative mice from each treatment group. The columns indicate baseline, day 3 and day 5 time points while each row shows the AZD 2171 (a-d), AZD 1480 (e-h), and Control groups (i-l). Supporting the group findings, a increase in *ADC* can be seen in panel h while the Control group shifts to a lower *ADC* distribution in panel l.

The final series of panels, shown in Fig VII-8, displays v_e data from represented animals from the treatment groups in a similar fashion. No trends or correlations are evident with this parameter. Interestingly, this parameter maintains very high values at all time points for all treatments. Some voxels surpassed the physiological boundary (v_e = 1) which were exempt from analyses; additional comments about this phenomena can be found in the subsequent chapter.

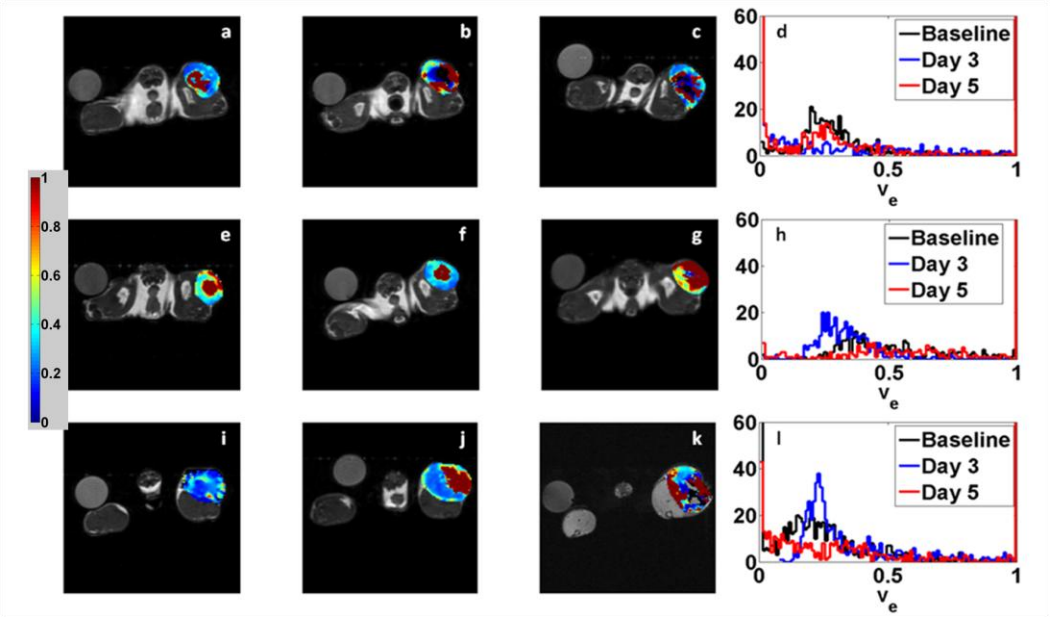

Fig. VII-8. v_e parametric maps for representative mice from each treatment group. The columns indicate baseline, day 3 and day 5 time points while each row shows the AZD 2171 (a-d), AZD 1480 (e-h), and Control groups (i-l).

Histological Correlation

Since Jak2 inhibition by AZD 1480 reduces Stat3 activity (as discussed in Chapter III), samples were stained with phosphorylated Stat3 (pStat3); all AZD 1480 samples were found to significantly inhibit pStat3 activity while AZD 2171 and control groups yield normal levels of expression. In order to verify the imaging results, stains for CD31 (as a marker for microvasculature) were acquired, and the pathologists scoring and comments are listed in Table VII-1 through VII-3. A histogram of the CD31 scoring for each treatment group is shown in Fig. VII-9 (a). A CD31 scoring ranges from 1+, which indicates little to no vasculature while a scoring of 3+ indicates a heavily vascularized section of tissue. As noted by the comments as well as the histogram, the AZD 2171 treated group showed reduced vasculature and distinct changes in vessel morphology that indicated vascular collapse (*e.g.*, as the vessels collapsed, the vessel structures resembled

more of a "slit" – like morphology). However, the distribution for CD31 scoring for AZD 1480 seems equally distributed into all scoring categories, similar to the CTL group, with only some tumors depicting morphological changes indicating "attenuated" vessels.

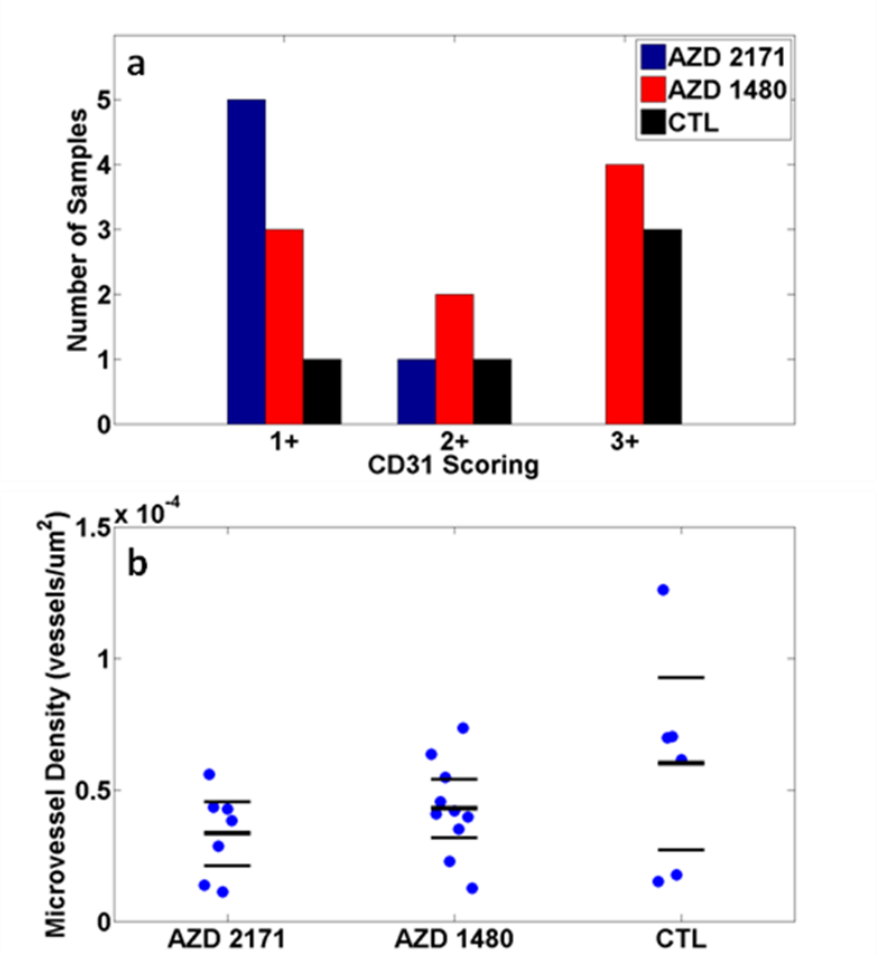

Fig. VII-9. Panel a shows a histogram of CD31 data depicting the number of samples from each treatment group scored 1+ (low/attenuated vasculature), 2+ (somewhat vascularized) or 3+ (highly vascularized). The CD31 findings support the group analyses in that vasculature was reduced in AZD 2171 while vasculature in AZD 1480 showed no significant decrease in K^{trans} or CD31. In panel b, microvessel density was calculated for all the samples in each treatment group. Each '•' represents a sample with the bold solid line being the mean and the error bars above and below are ± (1.96 × standard error). While both AZD2171 ($p = 0.13$) and AZD1480 ($p = 0.42$) groups trended toward reduced microvessel density relative to the control group, no significance was reported.

In order to quantify the vasculature in histology, microvessel density was calculated from the CD31 staining, described in the *Methods* section, and the results are shown in Figure VII-9 (b). While no significant differences were detected in either treatment groups from the control group, the control group displays a larger variation in measurements than both treatment groups. Interestingly, both AZD 2171 and AZD 1480 groups have similar microvessel density as measured by CD31 after the last imaging time point.

Additional immunohistochemistry analyses for cellular activity included H&E, Ki-67, and cParp staining; the results of these analyses are shown in Fig. VII-10. Panel (a) demonstrated the extracellular space fraction (*EC* (*%*)) on H&E stained slides, calculated as described in the *Methods* section, for each group. A significant increase in *EC* (*%*) was found between the AZD 1480 treatment group and the control group while the AZD 2171 showed an increasing trend in *EC* (*%*). To quantify the effects on proliferation, Ki-67 was used to identify the percentage of cells that was actively proliferating at the last imaging time point; the results for all three groups are shown in panel (b), and no statistical significances were reported between treatment and control groups. Finally, cParp, a marker for apoptosis, was quantified as percentage of cells that stained positive for apoptotic activity. The results of this study are shown in Fig. VII-10 (c) with a statistically significant ($p = 0.036$) increase in cParp staining for the AZD 1480 treatment group compared to the control group. Sample slides from CD31, Ki-67, and cParp are shown in Fig. VII-11.

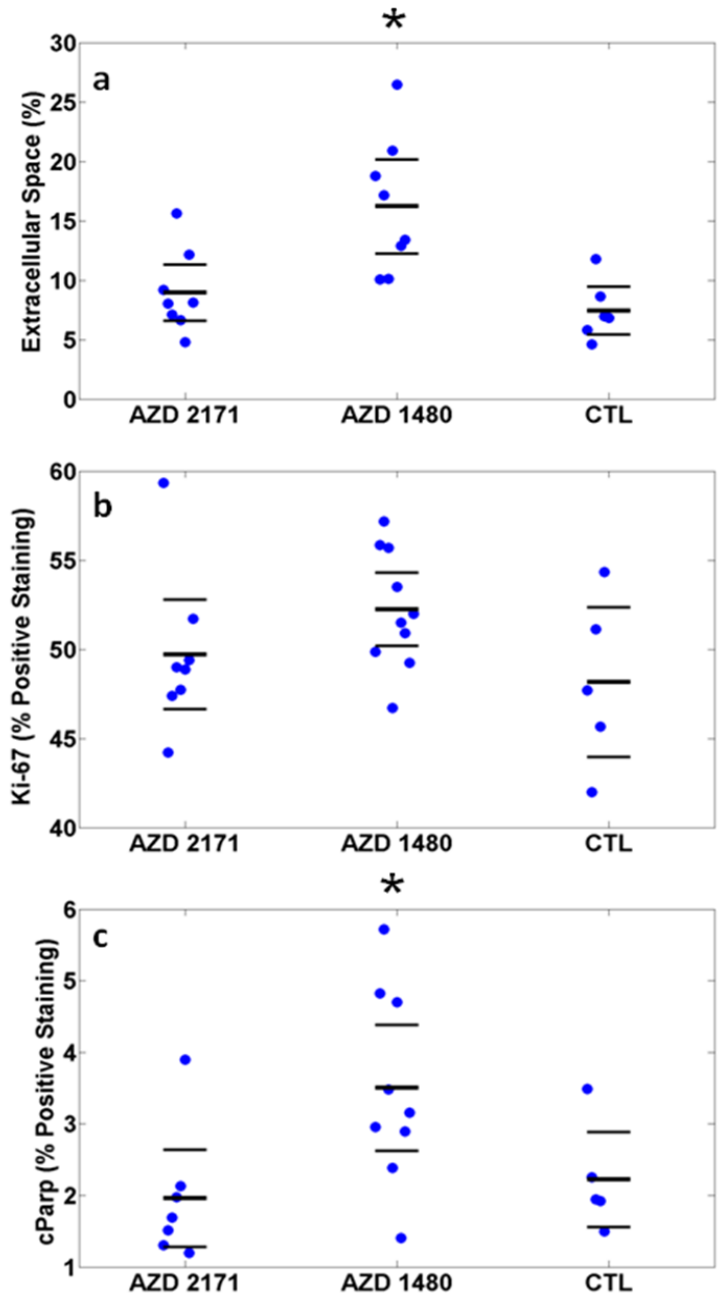

Fig. VII-10. Panels a, b, and c display cell density, Ki-67, and cParp staining results, respectively for each group. Each '•' represents a sample with the bold solid line being the mean and the error bars above and below are ± (1.96 × standard error). Panel (a) displays the cell density results as determined by H&E staining while panel (b) shows percentage of cells that stained positive for Ki-67 activity. Similarly, panel (c) depicts the percentage of cells that stained positive for cParp activity.

Discussion

The use of a Jak2 inhibitor as an anti-cancer treatment has been shown to interfere with several oncogenic pathways. Downstream effects of inhibiting Jak2 include prohibiting angiogenesis (2,3), decreasing cellular proliferation (1), and increasing apoptotic activity (1,2); thus, Jak2 inhibitors such as AZD 1480 have been shown as effective methods of inhibiting tumor growth (4). One of the unique advantages of imaging tumor physiology is the ability to capture changes prior to any palpable/volumetric changes in tumor growth. Thus, the goal of this study was to examine the efficacy of AZD 1480 using two imaging techniques that report on the physiologic attributes of angiogenesis and cellularity.

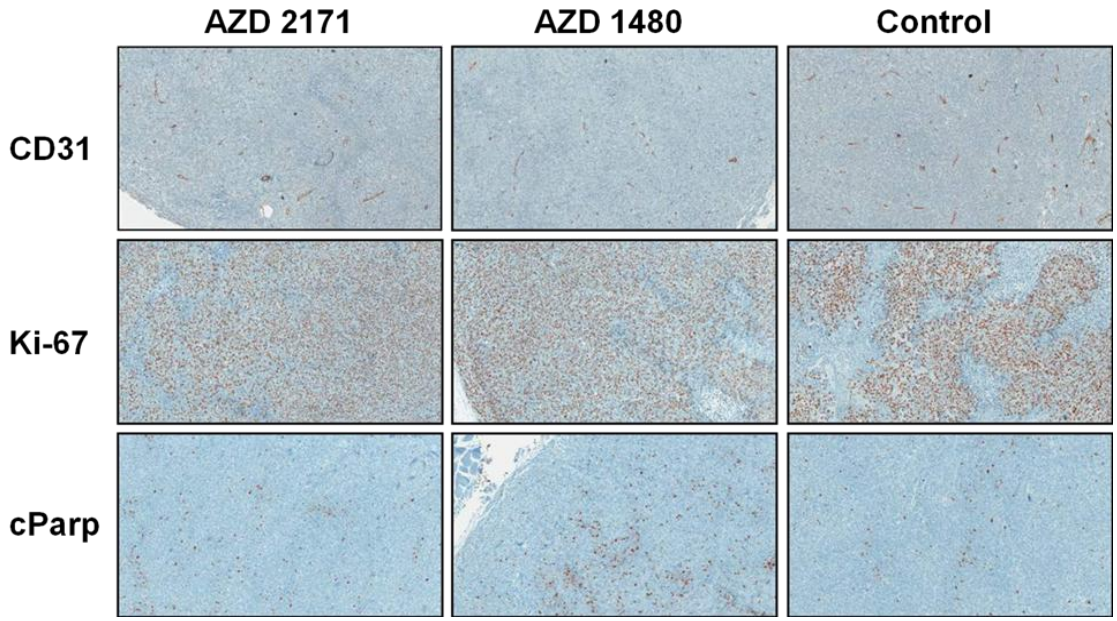

Fig. VII-11. Sample staining for CD31 (first row), Ki-67 (second row), and cParp (last row) for the AZD 2171 treatment group (first column), AZD 1480 treatment group (second column), and Control group (last column). The brown staining shown in the CD31 staining indicates a positive stain for CD31 on endothelial cells while a brown staining in the Ki-67 images indicates cells that are in a proliferative state. The brown staining for the cParp images indicate cells positive for the Parp cleavage typically characterized by cells undergoing apoptosis.

The group changes demonstrated in this work indicate that day 3 and day 5 of a once per day dose (50 mg/kg) of AZD 1480 is possibly too early to see any anti-angiogenic effects. Compared to the positive control AZD 2171, which is a potent anti-angiogenic drug, changes in the vasculature of the AZD 1480 group were not evident as supported by immunohistochemistry.

Interestingly enough, the more sensitive measure for AZD 1480 treatment seemed to be *ADC*. Significant increases in *ADC* were indicated in the group study and shifts were noted on a voxel-by-voxel level. Additionally, while tumor volume gave no significant indications of efficacy for this group, immunohistochemistry indicated a significant increase in apoptosis and extracellular space (*EC* (*%*)) in this treatment group. Thus, cellular level changes could be identified prior to any anti-angiogenic affects could be noted. In previous work, changes in vascularity have been seen as early as day 6 with this dosing regimen in this cell line by CD31 staining (D. Huszar, unpublished results). One could hypothesize that if the treatment and subsequent DCE-MRI data were taken out over a longer period of time, significant decreases in K^{trans} might be noted, but logistics could not permit a longitudinal study of that length for this work. Since *ADC* was determined as a sensitive parameter, it appears that Jak2 inhibition initially impacts cellular function within the tumor with a potential latent affect on vascularity.

As discussed in Chapter IV, DW-MRI has been shown to correlate with cell density measures in cancer (11-14). In this study, significant difference was found in extracellular space (indirectly identifying cell density) measures from H&E in the AZD 1480 group; however, v_e did not illustrate any significant trends other than a demonstrating a significant decrease on day 5 for the AZD 2171. With a significant change in cParp

(apoptosis surrogate) and *EC* (%) and no difference in Ki-67 (proliferation marker), one could hypothesize that the changes in *ADC* are primarily induced by pro-apoptotic activity. At a molecular level, significant changes in cParp indicate apoptotic activity; Parp is a protein involved in DNA repair, differentiation, and chromatin structure formation. During apoptosis, caspase-3 (mentioned in Chapter III) cleaves this protein. Thus, the cleaved fragment of Parp (cParp) indicates caspase/apoptotic activity (15).

Regretfully, these endpoint histology measures do not allow the change in these histology parameters to be compared to the changes in imaging parameters. However, the relationship between these histology endpoint measurements and the imaging data is explored in more detail in the following chapter (Chapter VIII). As mentioned earlier, *ADC* can be affected by several cellular/extracellular activities such as changes in active transport, blood flow, and tissue re-organization (16). These changes can also be transient with treatment activity; for example initial cellular swelling and reduced blood flow may lead to lower *ADC* values earlier in treatment (17). As cells begin to die, edema, reduced cell density, and tissue reorganization may lend to an increase in *ADC*, as seen frequently during treatment of malignant tumors (16). Thus, it is possible that the change in *ADC* reflects a change in tissue reorganization as apoptosis increases. Similarly, cell density correlation with *ADC* may be confounded by changes in blood flow and perfusion in the positive control AZD 2171. This anti-angiogenic drug can cause vessel attenuation and degradation leading to vessel/tissue component reorganization. While no significant changes in *ADC* were noted in the AZD 2171 group, the *ADC* at day 5 demonstrated an increasing trend as did the percent extracellular space (*EC* (%)). Thus, it appears that

ADC reports on different cellular / tissue properties based on both cancer and treatment model; regardless, it seems to be a more sensitive measure for drugs inhibiting Jak2.

The goal of this study was to assess the efficacy of AZD 1480 using parameters from both DCE-MRI and DW-MRI. As anticipated, K^{trans}, an indicator of blood flow/perfusion reported significant changes in the anti-angiogenic drug, AZD 2171, treatment group from baseline measurements; this finding was also supported by histology. K^{trans} did not seem to reliably report any treatment response for AZD 1480 but significant changes in *ADC* at both day 3 and day 5 post-treatment and significant apoptotic activity and increased extracellular fraction indicated that cellular activity may be a better biomarker for early treatment response using a Jak2 inhibitor.

References

1. Dang CV. c-Myc target genes involved in cell growth, apoptosis, and metabolism. Mol Cell Biol 1999;19(1):1-11.
2. Niu G, Bowman T, Huang M, Shivers S, Reintgen D, Daud A, Chang A, Kraker A, Jove R, Yu H. Roles of activated Src and Stat3 signaling in melanoma tumor cell growth. Oncogene 2002;21(46):7001-7010.
3. Semenza GL. Targeting HIF-1 for cancer therapy. Nat Rev Cancer 2003;3(10):721-732.
4. Hedvat M, Huszar D, Herrmann A, Gozgit JM, Schroeder A, Sheehy A, Buettner R, Proia D, Kowolik CM, Xin H, Armstrong B, Bebernitz G, Weng S, Wang L, Ye M, McEachern K, Chen H, Morosini D, Bell K, Alimzhanov M, Ioannidis S, McCoon P, Cao ZA, Yu H, Jove R, Zinda M. The JAK2 inhibitor AZD1480 potently blocks Stat3 signaling and oncogenesis in solid tumors. Cancer Cell 2009;16(6):487-497.
5. Wedge SR, Kendrew J, Hennequin LF, Valentine PJ, Barry ST, Brave SR, Smith NR, James NH, Dukes M, Curwen JO, Chester R, Jackson JA, Boffey SJ, Kilburn LL, Barnett S, Richmond GH, Wadsworth PF, Walker M, Bigley AL, Taylor ST, Cooper L, Beck S, Jurgensmeier JM, Ogilvie DJ. AZD2171: a highly potent, orally bioavailable, vascular endothelial growth factor receptor-2 tyrosine kinase inhibitor for the treatment of cancer. Cancer Res 2005;65(10):4389-4400.
6. Wedge SR, Ogilvie DJ, Dukes M, Kendrew J, Chester R, Jackson JA, Boffey SJ, Valentine PJ, Curwen JO, Musgrove HL, Graham GA, Hughes GD, Thomas AP, Stokes ES, Curry B, Richmond GH, Wadsworth PF, Bigley AL, Hennequin LF. ZD6474 inhibits vascular endothelial growth factor signaling, angiogenesis, and tumor growth following oral administration. Cancer Res 2002;62(16):4645-4655.
7. Kety SS. Peripheral blood flow measurements. Pharmacol Rev 1951;3:1-41.
8. Landis CS, Li X, Telang FW, Coderre JA, Micca PL, Rooney WD, Latour LL, Vetek G, Palyka I, Springer CS, Jr. Determination of the MRI contrast agent concentration time course in vivo following bolus injection: effect of equilibrium transcytolemmal water exchange. Magn Reson Med 2000;44(4):563-574.
9. Trune DR, Kempton JB, Gross ND. Mineralocorticoid receptor mediates glucocorticoid treatment effects in the autoimmune mouse ear. Hear Res 2006;212(1-2):22-32.
10. Wilcoxon F. Individual Comparisons by Ranking Methods. Biometrics Bulletin 1945;1(6):80.
11. Sugahara T, Korogi Y, Kochi M, Ikushima I, Shigematu Y, Hirai T, Okuda T, Liang L, Ge Y, Komohara Y, Ushio Y, Takahashi M. Usefulness of diffusion-weighted MRI with echo-planar technique in the evaluation of cellularity in gliomas. J Magn Reson Imaging 1999;9(1):53-60.
12. Hayashida Y, Yakushiji T, Awai K, Katahira K, Nakayama Y, Shimomura O, Kitajima M, Hirai T, Yamashita Y, Mizuta H. Monitoring therapeutic responses of primary bone tumors by diffusion-weighted image: Initial results. Eur Radiol 2006;16(12):2637-2643.

13. Guo Y, Cai YQ, Cai ZL, Gao YG, An NY, Ma L, Mahankali S, Gao JH. Differentiation of clinically benign and malignant breast lesions using diffusion-weighted imaging. J Magn Reson Imaging 2002;16(2):172-178.
14. Squillaci E, Manenti G, Cova M, Di Roma M, Miano R, Palmieri G, Simonetti G. Correlation of diffusion-weighted MR imaging with cellularity of renal tumours. Anticancer Res 2004;24(6):4175-4179.
15. Stadelmann C, Lassmann H. Detection of apoptosis in tissue sections. Cell Tissue Res 2000;301(1):19-31.
16. Padhani AR, Liu G, Koh DM, Chenevert TL, Thoeny HC, Takahara T, Dzik-Jurasz A, Ross BD, Van Cauteren M, Collins D, Hammoud DA, Rustin GJ, Taouli B, Choyke PL. Diffusion-weighted magnetic resonance imaging as a cancer biomarker: consensus and recommendations. Neoplasia 2009;11(2):102-125.
17. Thoeny HC, De Keyzer F, Chen F, Vandecaveye V, Verbeken EK, Ahmed B, Sun X, Ni Y, Bosmans H, Hermans R, van Oosterom A, Marchal G, Landuyt W. Diffusion-weighted magnetic resonance imaging allows noninvasive in vivo monitoring of the effects of combretastatin a-4 phosphate after repeated administration. Neoplasia 2005;7(8):779-787.

CHAPTER VIII

PRELIMINARY CROSS-CORRELATION OF CELL DENSITY MEASUREMENTS USING DCE-MRI, DW-MRI AND HISTOLOGY IN SUBCUTANEOUS CALU-6 XENOGRAFTS

Introduction

In Chapter IV, it was discussed that the apparent diffusion coefficient (*ADC*) maps obtained from DW-MRI have not only been shown to be a metric of cellularity in tumors (1-3), but have also been used to examine treatment response to both chemotherapy and radiotherapy (4,5) in preclinical and clinical settings. Based on Einstein's equation describing Brownian motion, if the diffusivity of free water at body temperature is ~ 2.5 $\mu m^2/ms$, within an interval of approximately 35 ms, water will move ~ 13 μm which is approximately the size of a cell. Thus, by adjusting the timing of a DW-MRI sequence, an estimation of cellularity can be determined based on the limitation placed upon diffusion by cellular membranes. This idea has been widely used in oncology. Correlations with *ADC* maps and tumor cellularity have been demonstrated (6-11). Because of its high sensitivity, DW-MRI has also been used to monitor treatment response in a variety of anti-cancer therapies, including both cytotoxic and anti-vascular/anti-angiogenic drugs (4,5,12). However, the specific changes in tissue that lead to these changes in *ADC* are not fully understood but most likely involves a combination of changes in cellularity, tissue reorganization, and increased extracellular space tortuosity, as mentioned in Chapters III and VII (13).

Pharmocokinetic modeling of DCE-MRI data also yields a parameter that has been shown to reflect cellularity. In the literature, v_e has been shown to correlate with cellular density and the extravascular, extracellular space (14-16). There are very few treatment studies that use v_e alone to predict response (17,18), and even fewer have examined this parameter as it relates to other cell density metrics, such as the study done by Yankeelov *et al* (12). In this study, DCE-MRI and DW-MRI were acquired both pre- and post-chemotherapy treatment in order to determine the sensitivity of these two techniques in determining treatment response. Of particular note in this study was the finding that the correlation between *ADC* and v_e was negative. While trends showing an increase in *ADC* and a decrease in v_e after treatment have been reported in this study and others (8,19-21), this is the first study to simultaneous examine the relationship between these parameters. However, this finding seems counterintuitive; as a tumor is successfully treated, there is a reduction in cell density presumably leading to an increase in *ADC* and an increase in v_e. Another study examining *ADC* and v_e in glioblastomas found confounding results as well. While both *ADC* and v_e have been assumed to be metrics of extravascular extracellular space, no relationship between the two parameters were found in glioblastoma multiforme (22); thus, a rigorous examination of both the relationship between these parameters and histological measures is needed.

This study proposed to investigate the relationship between *ADC* and v_e by the two aforementioned types of treatment, AZD 2171 and AZD 1480, to manipulate the cellularity levels within the tumor. DCE-MRI and DW-MRI imaging at different time points during these treatments were used to examine any spatial and temporal relationship

that might exist between these two imaging measures; then, endpoint imaging data were examined with histology data.

Methods

The same data sets acquired in the previous chapter were used for analyses in this study. For detailed information on tumor model, animal model, or acquisition parameters, see *Chapter VII: Methods*.

Statistical Correlation Analysis

In order to determine if any relationship exists between *ADC* and v_e, imaging data were examined at two levels for correlation: spatial correlation between voxel data and histological correlation with immunohistochemistry findings.

To determine if a spatial correlation exists between these two measures, sets of imaging data acquired from eight animals at the baseline time point were used. For each animal, two parametric maps containing *ADC* and v_e data were filtered to ensure non-physiologically relevant data were removed (e.g., $0 < v_e < 1$, $0 < ADC < 0.0033$ mm^2/s – approximately the *ADC* of free water at body temperature + 10%). Then, the voxel pairs were plotted against each other, and linear regression was used to characterize any relationship between the two parameters; the Pearson correlation coefficient was found between data sets to assess the significance of the relationship.

Imaging data that was obtained at day 5 post-treatment (Chapter VII) were filtered to only include animals that had reasonable phantom/muscle data (0.0027 mm^2/s $> ADC_{phantom} > 0.0033$ mm^2/s and $0 > v_e > 1$, with typical wash-in/wash-out characteristics

of muscle). These multi-slice MRI maps were examined to find a single slice that represented the corresponding section of the tissue slice that was stained using hemotoxylin and eosin (H&E) for nuclei (dark purple) and cytoplasm (light purple), respectively. Aperio (Vista, CA) digital histology images of the tumor were acquired at 20× magnification. The Positive Pixel Count Algorithm, developed by Aperio, was used to create maps of intra- and extracellular regions based on intensity thresholding; briefly, based on the intensity of the stains, images were thresholded into four categories: positive (*e.g.*, hemotoxylin), strong (*e.g.*, eosin), weak (*e.g.*, eosin), and no staining (*e.g.*, extracellular regions). The percentage of extracellular (*EC* (*%*)) space was found as described by Eqn. (VII-1). Imaging data from the corresponding histology slice were then compared to this parameter to determine the relationship, if any, between *ADC*, v_e, and the extracellular compartment. Linear regression parameters and Pearson correlation coefficients were found for 1) v_e and *EC*, 2) *ADC* and *EC*, and 3) *ADC and* v_e.

Results

Data acquired at baseline for eight animals were used to assess spatial correlation between *ADC* and v_e. The results of a linear regression and correlation analyses are presented in Table VIII-1.

TABLE VIII-1
SPATIAL CORRELATION OF *ADC* AND v_E.

ID	M ($\times 10^{-4}$)	b ($\times 10^{-4}$)	R^2 (fit)	R (data)
1	3.50	4.80	0.36	0.36
2	2.91	2.79	0.20	0.20
3	2.53	6.99	0.15	0.16
4	0.19	7.47	0.10	0.10
5	6.29	7.47	0.18	0.04
6	-0.34	9.30	0.02	-0.02
7	4.26	2.93	0.25	0.25
8	-1.29	9.65	0.14	-0.13
Average	**1.76**	**6.43**	**0.17**	**0.12**
STD	**1.93**	**2.65**	**0.10**	**0.16**

As demonstrated by the remarkably low R^2 fit (average = 0.17), no linear relationship was identified between *ADC* and v_e. Additionally, the slope was approximately 0 (average = 1.76×10^{-4}), reaffirming the lack of a statistical relationship between these two parameters. When the data sets were directly correlated using the Pearson correlation coefficient, R, the average R value was 0.12. Three mice (indicated by each row) are illustrated in Fig. VII-2 Parametric maps of v_e (first column) and *ADC* (second column) were paired and plotted against each other in the scatter plot depicted in the third column. The black line indicates the trend line fit to the data. The examples in this figure clearly support the lack of direct spatial correlation between these two parameters.

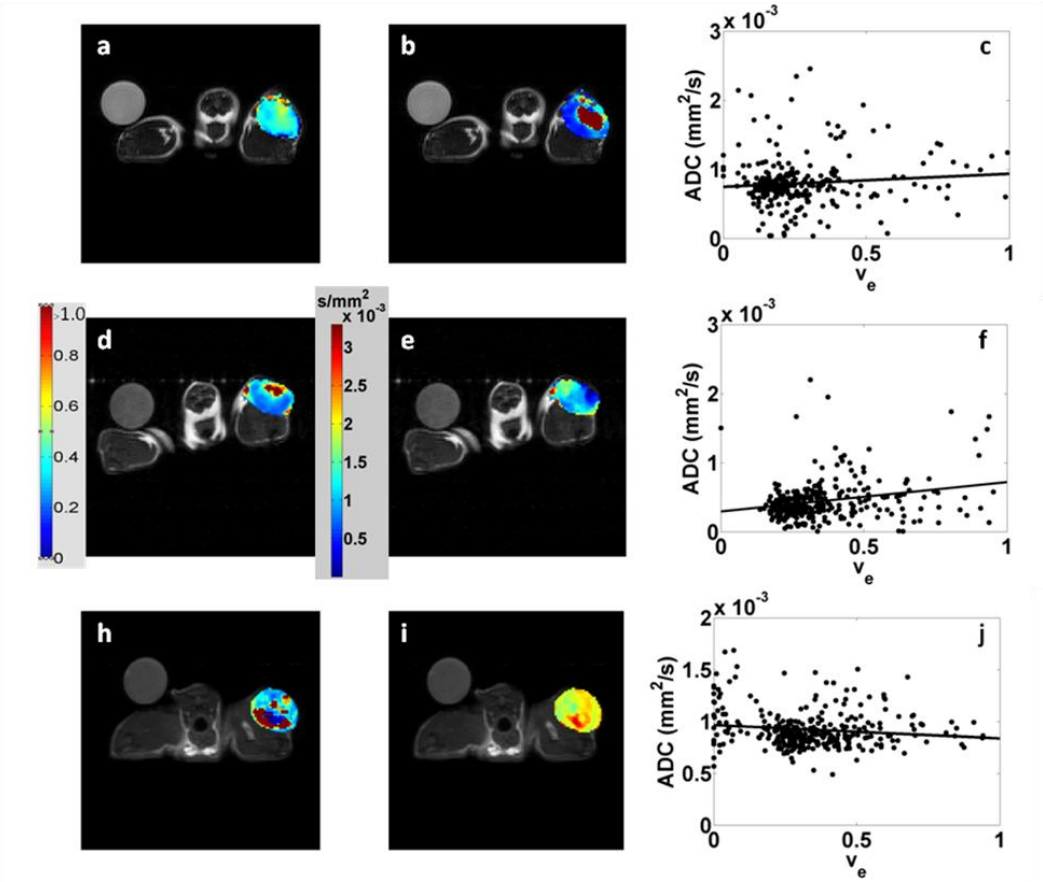

Fig. VIII-1. Example v_e (leftmost column) and *ADC* (center column) for three mice (ID # 4, 3, and 6 from Table VIII-I). Plots of v_e vs. *ADC* for each animal are displayed in panels c, f and j. A trend line is shown on each scatter plot by the solid black line; slope and goodness of fit parameters can be found in Table VIII-1.

H&E data obtained from the end time point were quantified to determine the extracellular cellular area fraction (*EC* (%)); then, the appropriate imaging slice was matched with each histology slice and the imaging and histology parameters were plotted against each other as shown in Fig. VIII-3. A significant positive correlation ($p = 0.007$) was found between *ADC* and *EC* (%), demonstrated in Fig. VIII-3 (a); additionally, an increasing trend between v_e and *EC* (%), shown in Fig. VIII-3 (b), was also found to be significant ($p = 0.02$).

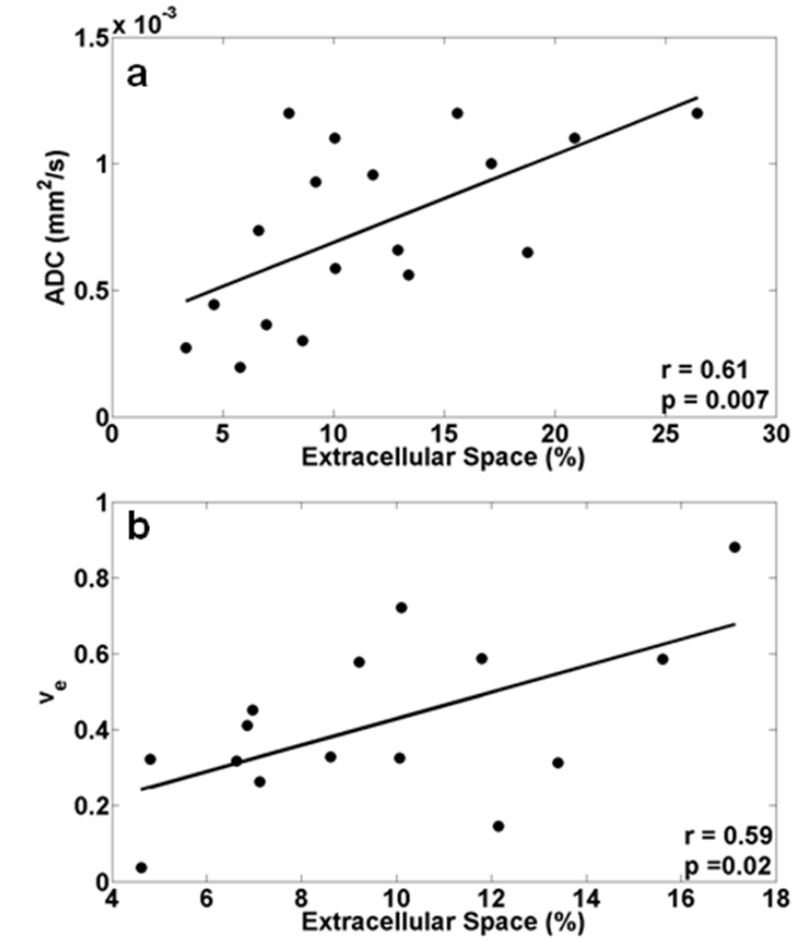

Fig. VIII-2. Panel a shows the results of comparing histology data (*EC* (%)) to *ADC* while panel b shows the comparison with v_e. A significant correlation was found between both *ADC* and *EC* (%) with a p = 0.007 as well as v_e and *EC* (%) with a p = 0.02.

The *ADC* and v_e values determined from the ROIs from each day 5 slice mentioned above were plotted against each other in Figure VIII-3. A positive linear trend is evident but no statistical significance (p = 0.15) was determined.

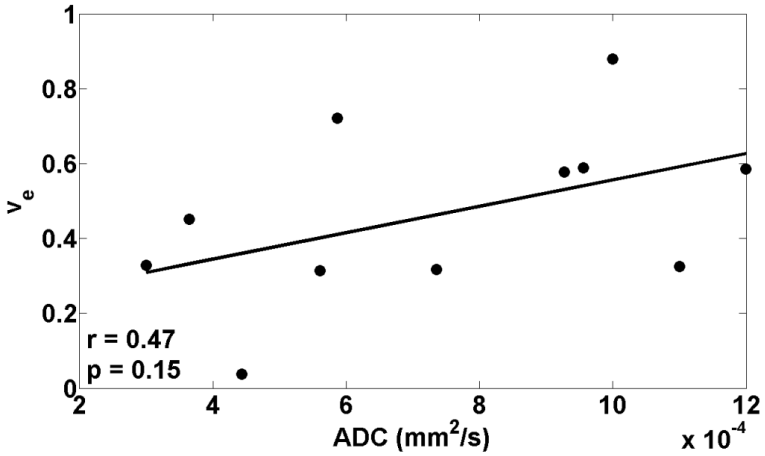

Fig. VIII-3. Average ADC and ve from each animal on the day 5 slice were plotted against each other and linear regression was used to determine any relationship. There was no significant correlation (p = 0.15).

Discussion

Recently, there has been a great interest in the imaging community to resolve the relationship between the parameters of v_e and *ADC*. Both these parameters have been shown to correlate with cell density in a similar fashion, independently (13,15), but the relationship between the two parameters appears to dissolve in response to cancer treatment. In fact, in some studies that have determined a temporal correlation in response to treatment, it has been found to be an inversely proportional relationship between these two metrics (12). It has been greatly detailed in the literature that *ADC* is highly sensitive to cellular changes during treatment (4,5) but very rarely has v_e been used as a primary metric assessing treatment efficacy.

Interestingly, this study shows that both *ADC* and v_e have a statistically significant positive correlation with the amount of extracellular space within the tumor. Since *ADC* is a reflection of the free diffusion of water, in areas of decreased cellular boundaries (high *EC* (*%)*), an increase in *ADC* is anticipated; similarly, an increase in extracellular

space should yield an increase in the DCE-MRI parameter v_e since it is a biomarker for this exact characteristic. While it is not necessarily surprising to see a significant relationship with these two parameters, it is surprising that v_e (the fraction of extravascular extracellular space) is hugely overestimated compared to its histological counterpart. Additionally, v_e showed little predictive value in terms of assessing treatment for AZD 1480 and AZD 2171, while ADC was able to determine that these significant changes in extracellular space were occurring during AZD 1480 treatment. Finally, these two metrics have very little spatial correlation as well, as shown in Table VIII-1. Thus, it seems that while both v_e and *ADC* correlate with cell density, there may be underlying tumor physiology that is influencing these measurements, specifically v_e.

To examine this point even further, Fig. VIII-4 and Fig. VIII-5 demonstrate the parametric maps derived from imaging with the corresponding histology slice. Panel (a), (b), and (c) in Fig. VIII-4 show the parametric maps for K^{trans}, v_e and *ADC* overlaid on a T_2-weighted images, while (d) is the original H&E slice with (e) indicating the thresholded image used to quantify EC (the white area represents the unstained regions, while purple, orange and yellow are thresholded stained areas separated by high, medium, and low intensity strength, respectively). Interestingly, the *ADC* map corresponds well with the dense cell staining in (d) and (e) as denoted by the dark purple (nuclei) staining (yellow arrows) as well as areas of low cell density (white/black arrows).

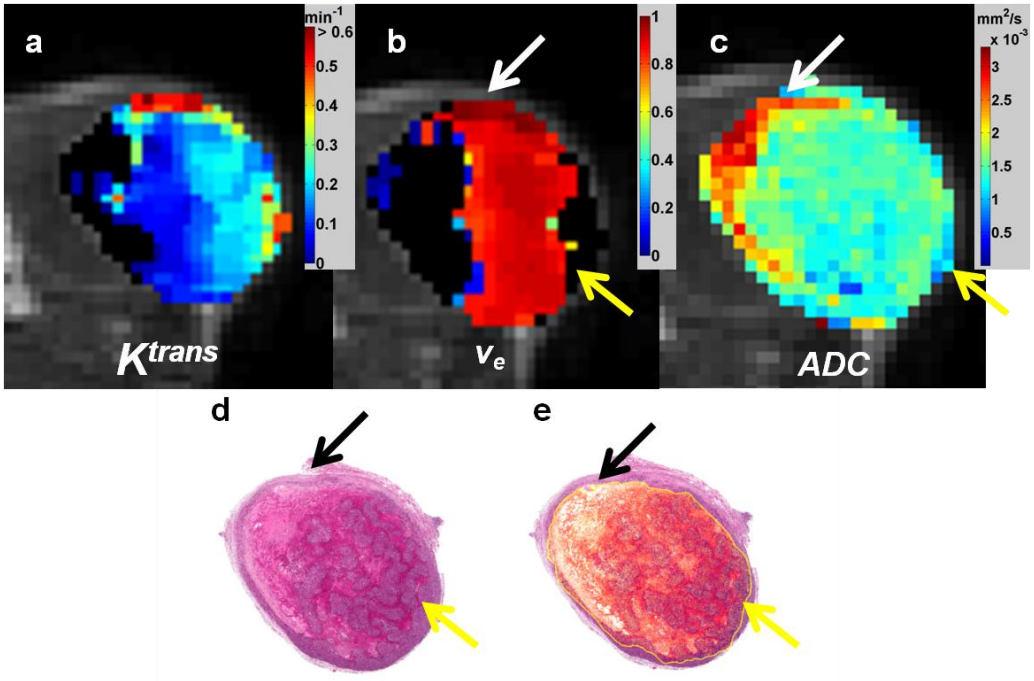

Fig. VIII-4. Panels (a), (b) and (c) depict the parametric maps for K^{trans} v_e, and *ADC* overlaid on a T_2-weighted image. Panels (d) and (e) are the corresponding histology slice with original and thresholded stains, respectively. Note the area indicated by the white and black arrows; this area appears to have reduced cell density. The *ADC* map seems to visually compare to the histology data while both K^{trans} and v_e show elevated values elsewhere. The yellow areas show a significantly dense area of the tumor as evident by the strong purple staining (nuclei) in panels d and e. Lower v_e and *ADC* values are evident here.

The maps of v_e in (b) show elevated values in the area indicated by the white/black arrows (low density regions) but the v_e distribution seems heterogeneous compared to the histology; note, however, that K^{trans} is low in the area with reduced cellularity. It seems that physiology that affects the flow and/or distribution of the CA could affect the v_e measurement; for example, the CA may be diffusing passively into to the tumor as opposed to active delivery.

Figure VIII-5 demonstrates another example of these parametric comparisons with histology. Panels (a) and (b) are *ADC* and ve maps, respectively while (c) and (d) are the original and thresholded stained histology slice.

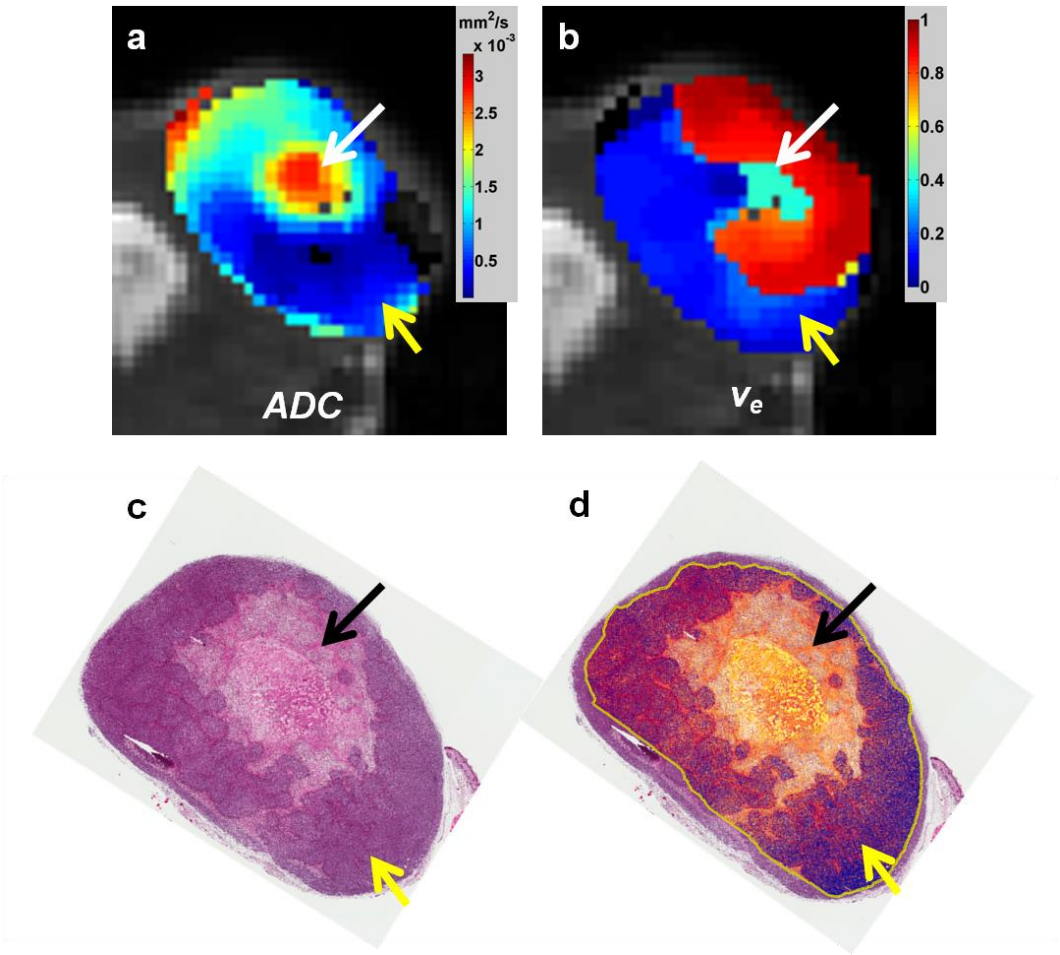

Fig. VIII-5. *ADC* and v_e parametric maps are shown in panels (a) and (b), respectively with the corresponding histology slice (original and thresholded) shown in (c) and (d), respectively. The black and white arrows emphasize an area of low cellularity while the yellow arrows indicate a dense area of cellular/nuclear staining.

As mentioned before, the *ADC* map corresponds well with areas of high and low cell staining. In this case, v_e is elevated in the area of low cell density as well, as indicated with the white and black arrows. Additionally, the yellow arrows emphasize the correlation with low *ADC*, low v_e and high cellular staining. Similar to Fig. VIII-4, there exists high v_e values but a very heterogeneous distribution in the v_e image that does not intuitively follow the histology information.

The significant correlation with *EC* (*%*) and the linear trend observed on an ROI average scale between v_e and *ADC* such as in Fig. VIII-3, suggest that cell density does strongly affect v_e. However, the lack of spatial correlation with v_e and *ADC* parametric maps as well as the heterogeneity in the histology comparison suggests that cellular density or extravascular/extracellular space might not be the only factor influencing v_e. Since v_e relies on the flow of a CA into the extravascular, extracellular space, regions that are not well perfused or necrotic regions such as that shown in Fig. VIII-4 and Fig. VIII-5, may misrepresent the extravascular, extracellular volume. This cell density measurement is based on the indirect method of quantifying the pharmacokinetics of a CA in tissue; thus, physiology that affects the flow and/or distribution of the CA (*e.g.*, passive diffusion or active delivery of the CA) will inherently confound the v_e measurement.

The inability of v_e to display predictive value in the study discussed in Chapter VII may suggest that improvement in the acquisition and/or analyses of the DCE-MRI data/model might be required to truly study this parameter. One interesting finding from the treatment study described in Chapter VII is that some tumors exhibited unique signal intensity curves that never quite plateaued; this phenomenon is illustrated in Fig. VIII-6.

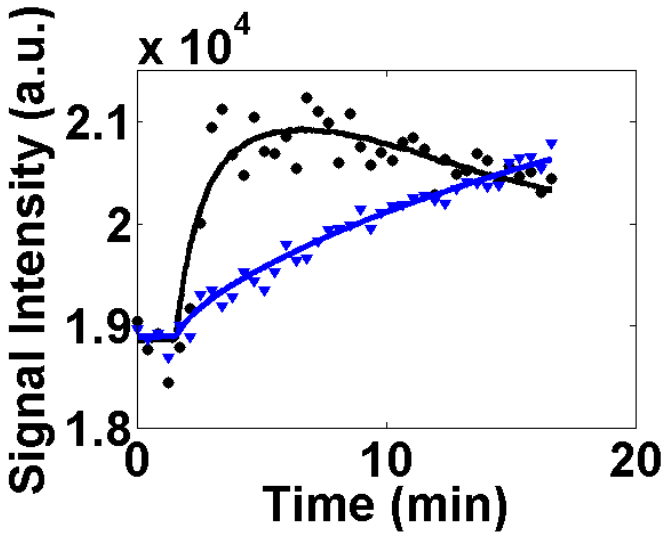

Fig. VIII-6. An example of a muscle tissue curve and corresponding fit (black) in comparison to a tumor tissue and fit (blue). No plateau or wash out period is evident for the tumor tissue curve.

The black circle/fit line data is the muscle curve acquired from the animal while the blue triangle/fit line represents the tumor tissue uptake. As evident in the muscle curve, there is a clear uptake and wash-out in this animal, indicating a successful injection of contrast agent.

While there is a possibility that some of the v_e overestimation seen in Fig. VIII-3 (b) could be due to the use of the population derived vascular input function (discussed in Chapter VI), the overestimation of this magnitude indicates another underlying issue. The tumor appears to never reach equilibrium, even after seventeen minutes of acquisition. For this particular animal, the v_e value returned from this fit was well over a 100% extravascular extracellular volume percent, which is physiologically implausible. While this fit returned a high R^2 value of > 0.95, the returned fit parameters are obviously flawed in this particular case. By examining this signal intensity time curve, it appears that there is another process, other than that dictated by K^{trans}, by which the contrast agent is entering the tumor. The gradual uptake in the latter time points of the tumor indicate

that contrast agent may be diffusing into the tumor from other surrounding tissue. For this study, spatially dependent diffusion had not been incorporated into the two compartment model but previous investigators have incorporated this component into the standard model (23).

This study suggests that both *ADC* and v_e are influenced by cellular density, but further investigation is warranted. An optimized study should be designed to allow for a more complete understanding of these two parameters. First, the Calu-6 model used in this study tend to have large areas of necroses that may confound gradual changes in cellular density; either a tumor model with less necroses should be chosen or care should be taken to use an imaging technique that accurately identifies necrotic regions that do not meet DCE-MRI/DW-MRI model assumptions. Additionally, a cytotoxic treatment such as doxorubicin, mentioned in Chapter III, is suggested to directly affect cellularity; the treatments used in this study were anti-angiogenic (AZD 2171) and a Jak2 inhibitor (AZD 1480) have an indirect effect on cellularity. In order to obtain absolute v_e values without the possibility of overestimation, an individual vascular input function should be acquired for each subject in the study. A model that incorporates diffusion within the two compartment model should be used in order to accurately obtain true physiological representation of the tumor kinetics. With these amendments to protocol design, a more rigorous comparison between v_e, *ADC*, and heterogeneous histology can be achieved.

References

1. Stejskal EO, Tanner JE. Spin diffusion measurements: spin echoes in the presence of a time dependent field gradient. J Chem Phys 1965;42:288-292.
2. Le Bihan D, Breton E, Lallemand D, Aubin ML, Vignaud J, Laval-Jeantet M. Separation of diffusion and perfusion in intravoxel incoherent motion MR imaging. Radiology 1988;168(2):497-505.
3. Chenevert TL, Brunberg JA, Pipe JG. Anisotropic diffusion in human white matter: demonstration with MR techniques in vivo. Radiology 1990;177(2):401-405.
4. Patterson DM, Padhani AR, Collins DJ. Technology insight: water diffusion MRI--a potential new biomarker of response to cancer therapy. Nat Clin Pract Oncol 2008;5(4):220-233.
5. Thoeny HC, De Keyzer F. Extracranial applications of diffusion-weighted magnetic resonance imaging. Eur Radiol 2007;17(6):1385-1393.
6. Sugahara T, Korogi Y, Kochi M, Ikushima I, Shigematu Y, Hirai T, Okuda T, Liang L, Ge Y, Komohara Y, Ushio Y, Takahashi M. Usefulness of diffusion-weighted MRI with echo-planar technique in the evaluation of cellularity in gliomas. J Magn Reson Imaging 1999;9(1):53-60.
7. Hayashida Y, Yakushiji T, Awai K, Katahira K, Nakayama Y, Shimomura O, Kitajima M, Hirai T, Yamashita Y, Mizuta H. Monitoring therapeutic responses of primary bone tumors by diffusion-weighted image: Initial results. Eur Radiol 2006;16(12):2637-2643.
8. Guo Y, Cai YQ, Cai ZL, Gao YG, An NY, Ma L, Mahankali S, Gao JH. Differentiation of clinically benign and malignant breast lesions using diffusion-weighted imaging. J Magn Reson Imaging 2002;16(2):172-178.
9. Humphries PD, Sebire NJ, Siegel MJ, Olsen OE. Tumors in pediatric patients at diffusion-weighted MR imaging: apparent diffusion coefficient and tumor cellularity. Radiology 2007;245(3):848-854.
10. Squillaci E, Manenti G, Cova M, Di Roma M, Miano R, Palmieri G, Simonetti G. Correlation of diffusion-weighted MR imaging with cellularity of renal tumours. Anticancer Res 2004;24(6):4175-4179.
11. Manenti G, Di Roma M, Mancino S, Bartolucci DA, Palmieri G, Mastrangeli R, Miano R, Squillaci E, Simonetti G. Malignant renal neoplasms: correlation between ADC values and cellularity in diffusion weighted magnetic resonance imaging at 3 T. Radiol Med 2008;113(2):199-213.
12. Yankeelov TE, Lepage M, Chakravarthy A, Broome EE, Niermann KJ, Kelley MC, Meszoely I, Mayer IA, Herman CR, McManus K, Price RR, Gore JC. Integration of quantitative DCE-MRI and ADC mapping to monitor treatment response in human breast cancer: initial results. Magn Reson Imaging 2007;25(1):1-13.
13. Padhani AR, Liu G, Koh DM, Chenevert TL, Thoeny HC, Takahara T, Dzik-Jurasz A, Ross BD, Van Cauteren M, Collins D, Hammoud DA, Rustin GJ, Taouli B, Choyke PL. Diffusion-weighted magnetic resonance imaging as a

cancer biomarker: consensus and recommendations. Neoplasia 2009;11(2):102-125.
14. Aref M, Chaudhari AR, Bailey KL, Aref S, Wiener EC. Comparison of tumor histology to dynamic contrast enhanced magnetic resonance imaging-based physiological estimates. Magn Reson Imaging 2008;26(9):1279-1293.
15. Vaupel P, Harrison L. Tumor hypoxia: causative factors, compensatory mechanisms, and cellular response. Oncologist 2004;9 Suppl 5:4-9.
16. Tofts PS, Brix G, Buckley DL, Evelhoch JL, Henderson E, Knopp MV, Larsson HB, Lee TY, Mayr NA, Parker GJ, Port RE, Taylor J, Weisskoff RM. Estimating kinetic parameters from dynamic contrast-enhanced T(1)-weighted MRI of a diffusable tracer: standardized quantities and symbols. J Magn Reson Imaging 1999;10(3):223-232.
17. Cooper RA, Carrington BM, Loncaster JA, Todd SM, Davidson SE, Logue JP, Luthra AD, Jones AP, Stratford I, Hunter RD, West CM. Tumour oxygenation levels correlate with dynamic contrast-enhanced magnetic resonance imaging parameters in carcinoma of the cervix. Radiother Oncol 2000;57(1):53-59.
18. Padhani AR, Husband JE. Dynamic contrast-enhanced MRI studies in oncology with an emphasis on quantification, validation and human studies. Clin Radiol 2001;56(8):607-620.
19. Sinha S, Lucas-Quesada FA, Sinha U, DeBruhl N, Bassett LW. In vivo diffusion-weighted MRI of the breast: potential for lesion characterization. J Magn Reson Imaging 2002;15(6):693-704.
20. Wedam SB, Low JA, Yang SX, Chow CK, Choyke P, Danforth D, Hewitt SM, Berman A, Steinberg SM, Liewehr DJ, Plehn J, Doshi A, Thomasson D, McCarthy N, Koeppen H, Sherman M, Zujewski J, Camphausen K, Chen H, Swain SM. Antiangiogenic and antitumor effects of bevacizumab in patients with inflammatory and locally advanced breast cancer. J Clin Oncol 2006;24(5):769-777.
21. Pickles MD, Lowry M, Manton DJ, Gibbs P, Turnbull LW. Role of dynamic contrast enhanced MRI in monitoring early response of locally advanced breast cancer to neoadjuvant chemotherapy. Breast Cancer Res Treat 2005;91(1):1-10.
22. Mills SJ, Soh C, Rose CJ, Cheung S, Zhao S, Parker GJ, Jackson A. Candidate biomarkers of extravascular extracellular space: a direct comparison of apparent diffusion coefficient and dynamic contrast-enhanced MR imaging--derived measurement of the volume of the extravascular extracellular space in glioblastoma multiforme. AJNR Am J Neuroradiol;31(3):549-553.
23. Pellerin M, Yankeelov TE, Lepage M. Incorporating contrast agent diffusion into the analysis of DCE-MRI data. Magn Reson Med 2007;58(6):1124-1134.

CHAPTER IX

CONCLUSION

DCE-MRI techniques are one of the more commonly used measurements for characterizing tumor associated vasculature. Parameters obtained using DCE-MRI are useful in measuring changes in tumor vascularity and cellularity in response to treatment. In addition, DCE-MRI studies offer quantification of the treatment response so that longitudinal studies of treatment might be better evaluated. The studies presented in this work have demonstrated the optimization of a pre-clinical DCE-MRI protocol, the application of two imaging techniques (DCE-MRI and DW-MRI) in longitudinally assessment of the efficacy of a novel anti-cancer therapy (AZD 1480), and closely examined the relationship between two imaging parameters that are biomarkers for cellular density (*ADC* and v_e).

This work has shown that the error associated with the population-derived VIF can be minimized such that a population averaged VIF can be used in a pre-clinical setting instead of an individually measured VIF. Therefore, future DCE-MRI protocols can be modified to offer more flexibility in providing higher SNR and improved spatial resolution critical to examining lesion heterogeneity.

Then, both DCE-MRI and DW-MRI were used to examine a novel Jak2 inhibitor compared to both a positive anti-angiogenic (AZD 2171) and vehicle controls. This work showed that measures of cellularity (*ADC*) produced from DW-MRI proved to be significantly more sensitive at early time points (day 3 and day 5 post-treatment) than

parameters reporting on the anti-angiogenic affect by DCE-MRI (K^{trans}); this information can be potentially applied to future pre-clinical and clinical trials.

And finally, quantitatively comparing cell density parameters produced by DCE-MRI (v_e) and DW-MRI (*ADC*) with each other and with histology showed that both correlate significantly with changes in extracellular volume, but it also yielded the need for future work in DCE-MRI model development and study design to fully elucidate factors that affect v_e. Overall, these contributions have aided in developing appealing future studies in addition to improving DCE-MRI use in pre-clinical longitudinal treatment studies.

APPENDIX A

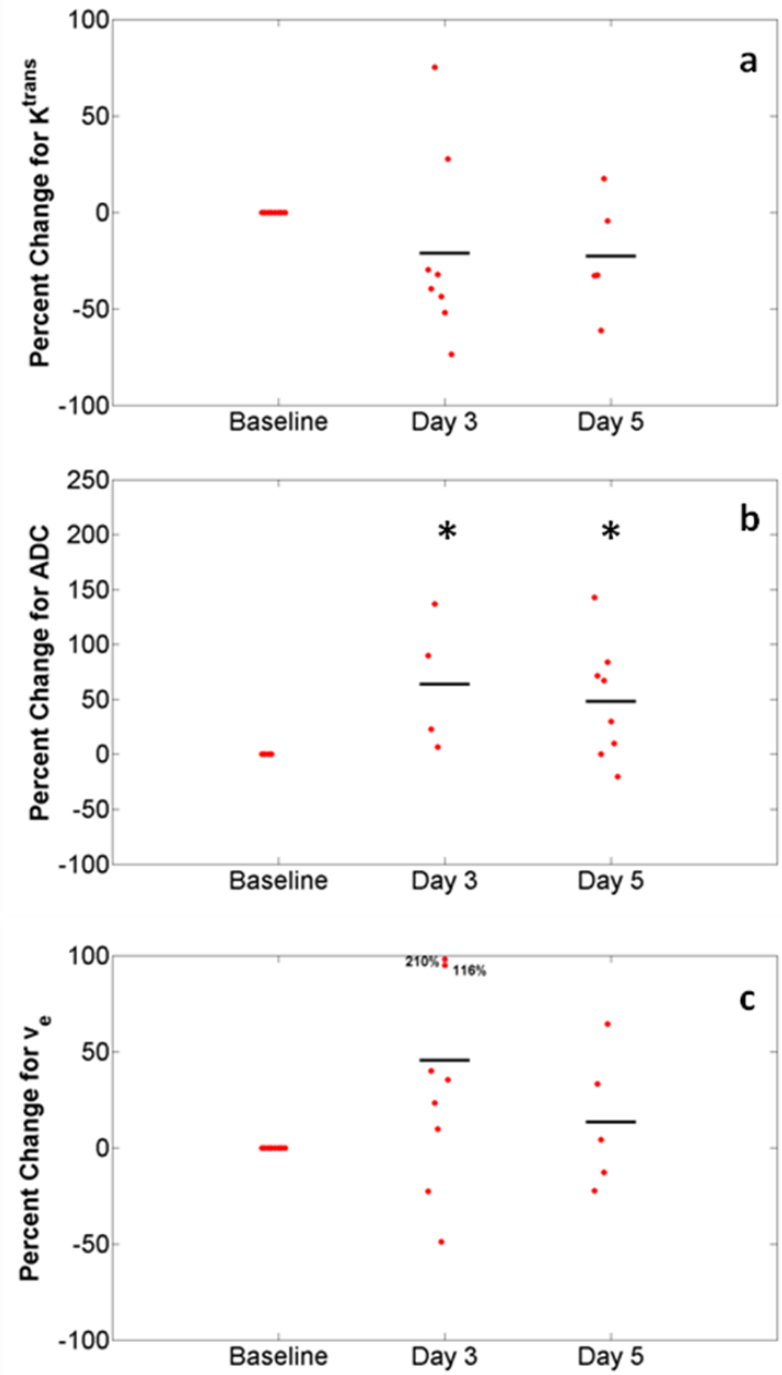

Fig. A-1 Percent change in K^{trans} (a), *ADC* (b) and v_e (c) for each individual subject in the AZD 1480 treatment group at baseline, day 3, and day 5 time points. The black horizontal line represents the group mean.

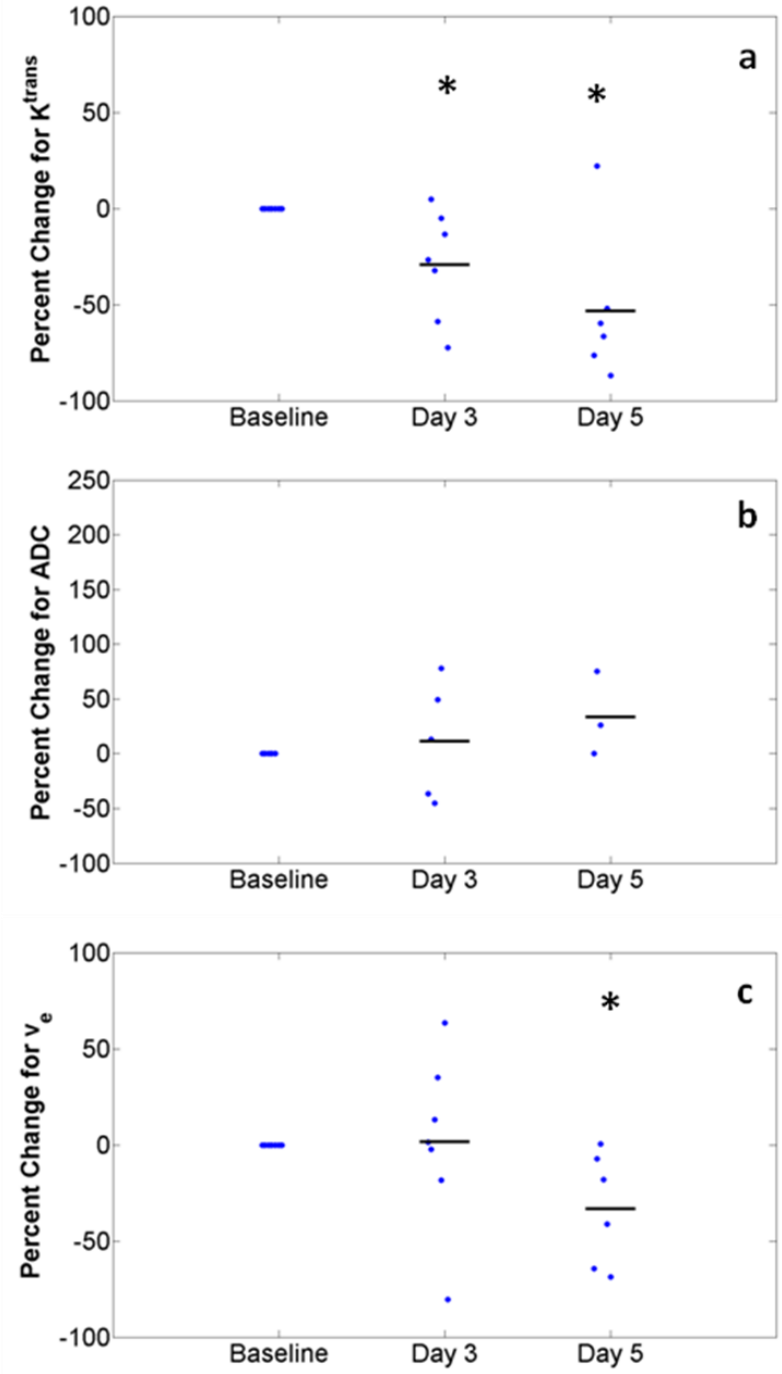

Fig. A-2 Percent change in K^{trans} (a), *ADC* (b) and v_e (c) for each individual subject in the AZD 2171 treatment group at baseline, day 3, and day 5 time points. The black horizontal line represents the group mean.

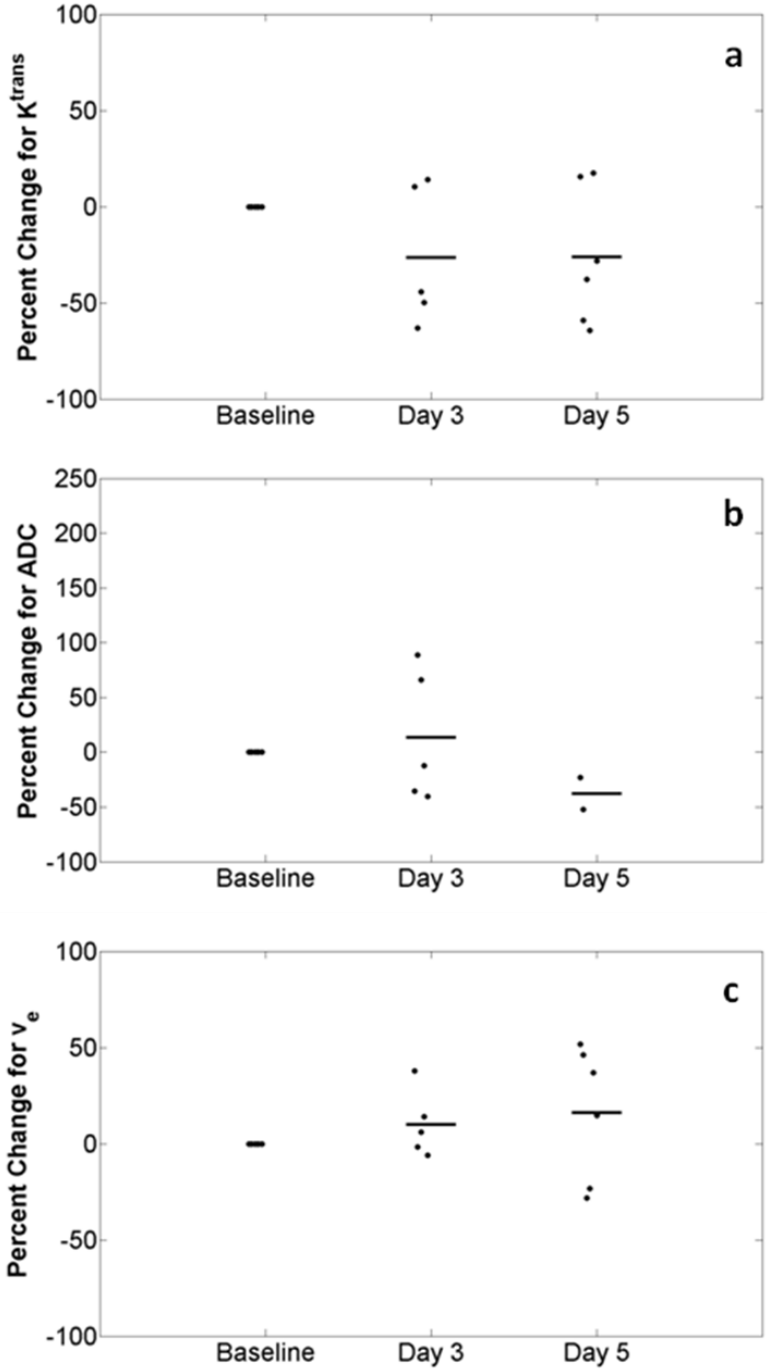

Fig. A-3 Percent change in K^{trans} (a), *ADC* (b) and v_e (c) for each individual subject in the Control treatment group at baseline, day 3, and day 5 time points. The black horizontal line represents the group mean.